UNIVERSITY OF BASILICATA

Doctor of Philosophy in:

Innovation and Sustainable Development Engineering:
Industrial, Energetic and Information Technologies

Radiation Physics and Experimental Characterization of the Radiation Fields Produced by a Heavy Ion Accelerator for Medical Applications

Disciplinary Scientific Sector:
ING-IND/18

Ph.D. Coordinator:
Prof.ssa Aurelia Sole

Candidate:
Francesco Bonforte

Supervisors:
Prof. Antonio D'Angola
Dr. Michele Ferrarini

Cycle XXXVI

A mamma e papà

Riassunto della Tesi

Negli ultimi anni, il trattamento dei tumori con ioni pesanti è aumentato, grazie alle loro particolari caratteristiche di deposizione energetica. Gli adroni sono particolarmente indicati per la radioterapia in quanto capaci di depositare energia in uno spazio limitato e confinato. Questa terapia è nota come adroterapia. Il Centro Nazionale di Adroterapia Oncologica (CNAO) a Pavia è uno dei sei centri al mondo in grado di trattare pazienti sia con protoni che con ioni di carbonio. In futuro, verrà installato un nuovo sincrotrone a protoni con gantry rotante e una facility di BNCT, mentre il sincrotrone esistente sarà aggiornato con una nuova sorgente di ioni che permetterà l'accelerazione di elio, litio, ossigeno e ioni di ferro per attività cliniche e di ricerca.

In questo contesto, la tesi si concentra sulla fisica della radiazione e sulla caratterizzazione sperimentale dei campi di radiazione secondaria generati da un sincrotrone utilizzato per applicazioni mediche. Di conseguenza, questo lavoro si propone una metodologia per determinare le correnti massime con cui i nuovi ioni possono essere accelerati senza modificare l'attuale design delle schermature e la caratterizzazione di un rem counter basato su un Micro Strutured Neutron Detector (MSND).

Lo studio per valutare le correnti per i nuovi ioni è condotto con il modello Monte Carlo noto in letteratura come Line of Sight, solitamente adottato per valutazioni di schermature. Il modello è stato adattato per il caso specifico introducendo un nuovo rapporto denominato Equivalent Carbon Ratio. Questo rapporto viene calcolato dividendo l'equivalente di dose ambientale ottenuto con un determinato ione in una data posizione di schermatura per la dose valutata con ioni di carbonio. I risultati ampliano i dati disponibili in letteratura per questi modelli, introducendo le curve di attenuazione per gli ioni di ferro a 306 MeV/u. Inoltre, il rapporto del carbonio può essere adottato anche per una prima valutazione delle correnti ioniche in altri centri di terapia adronica che già accelerano ioni di carbonio. La valutazione finale delle correnti è stata condotta con simulazioni Monte Carlo con l'implementazione della geometria completa del CNAO in FLUKA, ponendo particolare attenzione alla geometria e al modello di perdita del fascio. Le correnti massime per ioni selezionati sono state calcolate moltiplicando il rapporto tra la dose fornita da un dato ione e gli ioni di carbonio a 400 MeV/u per la corrente massima consentita per gli ioni di carbonio. I valori riportati sono valutati considerando circa 400 punti di dose sia all'interno dei confini del CNAO con valori superiori a 10 μSv/anno sia punti al di fuori dei confini del CNAO.

Per la caratterizzazione del rem counter sono stati condotti studi computazionali e sperimentali. Il detector si basa su un rivelatore neutronico microstrutturato (MSND) circondato da un moderatore sferico a base di polietilene con inserti di cadmio e piombo. L'intero sistema è poi collegato a un Raspberry Pi attraverso pin GPIO per controllarlo a distanza. Un primo esperimento è stato effettuato per verificare le prestazioni tra il MSND e il collegamento Raspberry Pi testando più programmi di conteggio. Il codice più performante è composto da uno script Python di visualizzazione e uno script C di conteggio. Il programma è in grado di gestire onde quadre fino a 90 kHz, ben oltre le richieste minime del MSND (66 kHz). La cuve di risposta del detector è stata caratterizzata utilizzando il codice Monte Carlo FLUKA per calcolando i conteggi$\cdot$cm^2 del rivelatore in funzione di 54 energie neutroniche da 10 meV a 1 GeV. I risultati mostrano un alto livello di accordo con i dati in letteratura su altri contatori di equivalente di dose ambientale. Durante la campagna sperimentale condotta presso il Czech Metrology Center (CMI), è stato stimato un fattore di calibrazione di 1,25 ± 0,06 nSv/conteggio con una sorgente Am-Be e il test di linearità mostra un rateo di dose di saturazione di 2 mSv/h. I test suggeriscono la possibilità di adottare il rivelatore anche per applicazioni di monitoraggio della perdita del fascio.

Infine, il rivelatore è stato testato presso la sala di taratura del CERN, presso la struttura CERF e nella sala del sincrotrone CNAO. Tutti i test mostrano una grande affidabilità del detector anche in campi misti ad alta intensità. In particolare, le misurazioni presso la sala di taratura con una sorgente Am-Be confermano il fattore di calibrazione calcolato presso il CMI e gli esperimenti condotti presso CERF e presso il CNAO mostrano una leggera sottostima della dose misurata dal rivelatore in campi neutronici ad alta energia. Questo comportamento è comune per i rem counter poiché di solito sono calibrati con sorgenti Am-Be o ^{252}Cf concentrate intorno a 1-10 MeV. Infatti, gli spettri della CERF e CNAO si estendono da meV fino a GeV e questo ampio range energetico può causare questa sottostima. Questo trend è stato confermato con simulazioni Monte Carlo dove è stato calcolato il rapporto tra la risposta del rem counter con sorgente Am-Be e lo spettro neutronico della CERF.

Dati gli ottimi risultati delle campagne sperimentali presso CERF e CNAO in campi misti ad alta intensità, si può concludere che il detector può essere utilizzato sia per la valutazione della dose ambientale sia per il monitoraggio della perdita del fascio presso il CNAO. L'idea è sviluppare un'infrastruttura di rete dedicata a un insieme di questi rilevatori per il monitoraggio dell'equivalente di dose ambientale in tempo reale in punti designati del centro. In particolare, questa applicazione può anche migliorare il modello di perdita del fascio adottato in questa tesi al fine di migliorare le future valutazioni di dose necessarie per valutare l'impatto radiologico del centro.

Abstract

Recently, the treatment of tumors with heavy ions has been increasing, thanks to their particular energy deposition characteristic. In fact, hadrons are particularly indicated for radiotherapy due to their capacity of depositing energy in a limited and confined space in contrast to other techniques. This practice is known as hadron therapy. The National Centre for Oncological Hadron Therapy (CNAO), Pavia is one of the six centers in the world able to treat patients with both protons and carbon ions. In the near future, a new proton synchrotron with a rotating gantry and a BNCT facility will be installed, and the existing synchrotron will be upgraded with a new ion source that allows the acceleration of helium, lithium, oxygen, and iron ions for both clinical and research activities. From a radiation protection perspective, secondary neutrons generated by accidental beam losses on machine components or on the patient are a significant concern for the future upgrade.

In this framework, this thesis focuses on the radiation physics and experimental characterization of secondary radiation fields generated by a synchrotron used for medical applications. The research includes the methodology for determining the maximum currents at which the new ions can be accelerated by using the pre-existing shielding system and the characterization of an extended-range radiation detector based on a Micro Structured Neutron Detector (MSND).

New ion currents have been assessed using two approaches: the line of sight model and simulations of the CNAO geometry in the Monte Carlo code FLUKA. These findings are valuable for other hadron therapy centers interested in accelerating different ion species. Radiation physics and experimental studies conducted on the rem counter demonstrate its reliability in complex mixed fields, making it suitable for both ambient dose equivalent and beam losses monitoring. The rem counter was calibrated at the primary standard Czech Metrology Center in Prague and experimental campaign was conducted to validate the detector's reliability at the CNAO center and the CERF facility at CERN.

In the first chapter, the CNAO center and the studies conducted by the CNAO radiation protection group are presented. Therefore, the aims of the thesis are introduced. The second chapter of the thesis is devoted to the evaluation of maximal currents at which the ions producted with the new source can be accelerated. It provides a concise overview of nuclear reactions at hadron therapy energies and introduces the Monte Carlo code FLUKA. The methodologies adopted for the assessments are then elaborated, including a comprehensive description of the beam loss model utilized for simulating the CNAO center. The results obtained are then discussed. Chapter three introduces the state of the

art of rem counters and their physical functioning. The rem counter developed at CNAO has been described in detail and in particular, tests on the feasibility of the connection between the MSND and the Raspberry Pi are conducted, with a specific emphasis on the software implementation. Subsequently, the Monte Carlo model adopted to evaluate the response function of the detector is presented. Lastly, the calibration factor and the linearity test carried out at the Czech Metrology Center are detailed. The fourth chapter is dedicated to the experimental campaigns conducted to test the reliability of the detector at CERN and CNAO. After providing an introduction to the facilities, a detailed analysis of the results is presented. In conclusion, the outcomes of the thesis are discussed and future developments are outlined.

Contents

1 | Introduction

1.1 Hadron Therapy and BNCT at CNAO

The CNAO (Centro Nazionale di Adroterapia Oncologica) located in Pavia is one of only six centers in the world that use both protons and carbon ions for hadron therapy [1]. Hadron therapy is a form of radiotherapy that utilizes an external beam consisting of hadrons to treat cancer. Ions are capable of releasing sufficient energy in tumor cells to deactivate them. From a physical perspective, the energy loss of a charged particle in a target can be expressed as a function of the target's density (ρ), the target charge (Z), the atomic number of the target (A), the incident ion charge (z), and the velocity of the incident ion (v), as follows:

$$-\frac{dE}{dx} \propto \rho \frac{Z}{A} \frac{z^2}{v^2} \tag{1.1}$$

The energy deposition as function of the depth in the tissue is shown in Figure 1.1. As

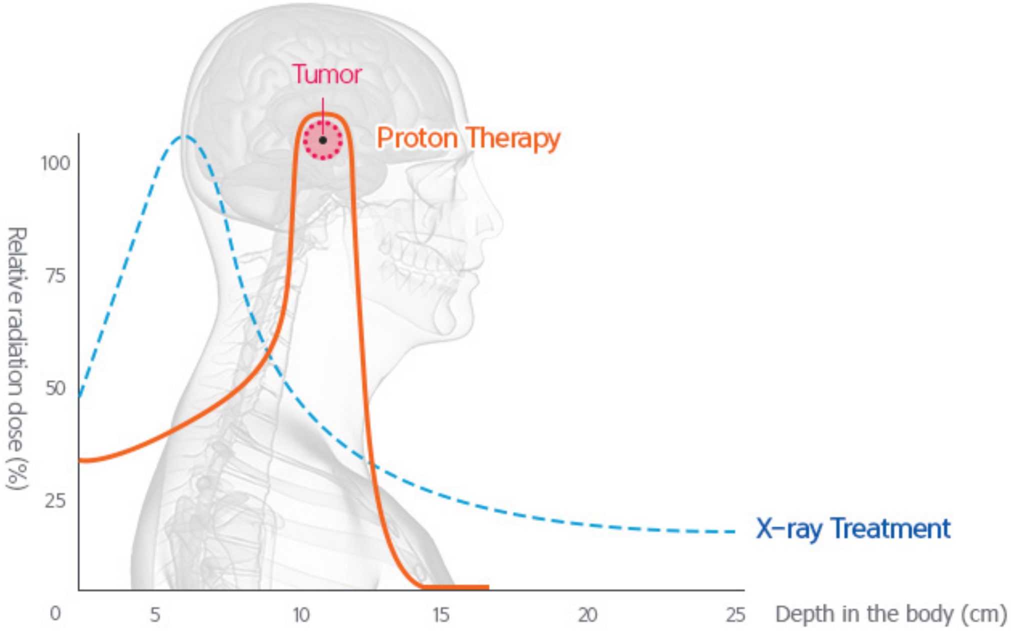

Figure 1.1: Dose as function of the depth in the tissue.

shown in Figure 1.1, the dose exhibits a sharp peak at the end of its path, commonly known as the Bragg peak. This peak can be utilized in treatment planning for tumors. This unique feature provides the opportunity to precisely treat tumors in challenging locations or those resistant to conventional radiotherapy. Examples of tumors that can be treated with hadron therapy include:

- Tumours of the brain;
- Tumours of the skull base and spinal cord;
- Tumours of the head neck and early respiratory tract;
- Tumours of the pelvis;
- Tumours of the limbs and spine;
- Pediatric solid tumours.

In recent years, hadron therapy has been increasingly adopted for cancer treatment. Since the 1990s, more than 290000 patients have received protontherapy treatments, with an annual increase of 35000 patients. Regarding carbon ions, approximately 40000 patients have been treated thus far. Since 2011, CNAO has treated more than 4000 patients, with an annual average ranging between 500 and 700 patients [2].

In the near future, CNAO will host a proton therapy facility with a rotating gantry and a Boron Neutron Capture Therapy (BNCT) facility. Furthermore, the existing synchrotron will also be capable of accelerating helium, lithium, oxygen, and iron ions for hadron therapy and experimental purposes.

1.1.1 CNAO Synchrotron and Protontherapy with Rotating Gantry

The CNAO synchrotron facility hosts a 25-meter diameter accelerator capable of accelerating protons up to 250 MeV and carbon ions up to 400 MeV/u. The mean current values for protons and carbon ions are $1.375{\cdot}10^{10}$ particles per second and $5.5{\cdot}10^{8}$ particles per second, respectively. Each year, the facility can accelerate $1{\cdot}10^{18}$ protons and $1.26{\cdot}10^{16}$ carbon ions. Ions are generated by two separate sources, using two separate Electron Cyclotron Resonance (ECR) sources, one using H_2 and the other CO_2 gas. To generate helium, lithium, oxygen, and iron ions (new ions), a third ECR source called AISHa (Advanced Ion Source for hadron therapy) will be installed [3]. The list of ions with their maximum energies that can be accelerated by the current synchrotron is provided in Table 1.1. In Figure 1.2, is shown the layout of the synchrotron facility. The synchrotron serves three treatment rooms (TR1, TR2, and TR3) and one experimental room (XPR). TR1 and TR3 a fixed horizontal beam lines are installed, while in TR2 has both horizontal and vertical beam lines. Finally, XPR features a fixed beam line with four isocenters. Machine operators have the ability to select the isocenter for the beam from the control room. Information regarding the number of particles accelerated in the synchrotron, their

Table 1.1: List of ions with corresponding energies used in the simulations.

Ion Beam	**Energy [MeV/u]**
^{4}He	250
^{7}Li	306
^{12}C	400
^{16}O	400
^{56}Fe	306

species (e.g., protons, carbon ions), and energies is recorded in a database software called CNAO History. In the near future, a proton therapy facility will be installed at CNAO to expand the number of patients who can access hadron therapy. This facility's distinctive feature is the adoption of a rotating gantry, which provides the capability to treat tumors from various angles while preserving healthy tissues.

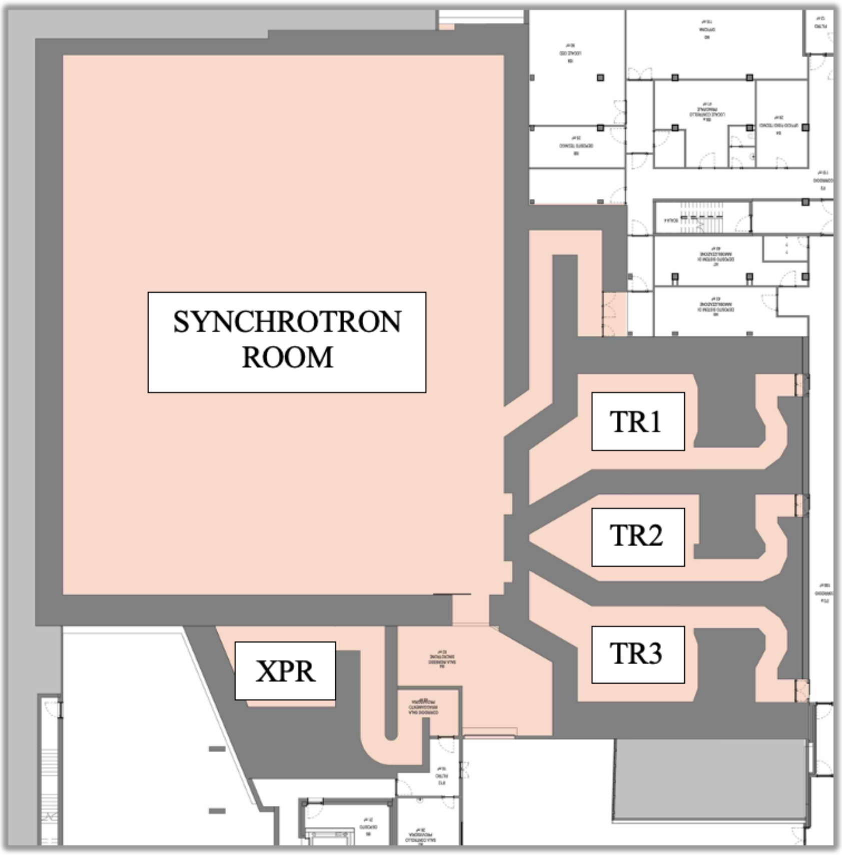

Figure 1.2: Layout of synchrotron room, experimental room (XPR) and treatment rooms (TR1, TR2, TR3) at CNAO.

1.1.2 BNCT Facility

Boron Neutron Capture Therapy (BNCT) is a radiotherapy tecnique that relies on selectively enriching cancer cells with ^{10}B and then irradiating them with themal neutrons having an energy of 0.025 eV. This energy level triggers the neutron capture reactions by boron, resulting in the following:

$$\mathrm{n} + {}^{10}\mathrm{B} \longrightarrow \begin{cases} {}^{7}\mathrm{Li} \;\; + \alpha + 2.79\, MeV (\text{ground state}) \\ {}^{7}\mathrm{Li}^{*} + \alpha + 2.31\, MeV (\text{excited state}) \end{cases} \tag{1.2}$$

The ^{10}B neutron capture reaction can proceed through two different channels. In the first channel, an α particle and a recoiling ^{7}Li nucleus in the ground state are emitted with a Q-value of 2.79 MeV. In the second channel, which is the most likely, boron undergoes decay, resulting in the emission of an alpha particle and a recoiling ^{7}Li nucleus in an excited state. This excited nucleus subsequently de-excites and emits a 0.478 MeV photon. These heavy ions are high Linear Energy Transfer (LET) particles with a range of a few micrometers, capable of damaging and breaking the DNA strands of a cell, ultimately leading to cell death. The unique characteristics of BNCT make it particularly suitable for treating specific types of cancers, including brain tumors, head and neck cancers, recurrent cancers, and other localized, deep-seated malignancies.

Historically, one of the primary challenges of BNCT has been the difficulty of accessing neutron facilities. This is because delivering a treatment requires neutrons within the energy range of 0.5 eV to 10 keV, which are primarily found in nuclear reactors. While these reactor-based centers serve scientific research well, they are not specifically designed for clinical treatments. To address this issue, in recent years, there has been a growing effort to develop accelerators that can be installed in hospitals or facilities like CNAO.

CNAO will host a BNCT facility based on a tandem accelerator that generates neutrons through the endothermic reaction:

$$^{7}\mathrm{Li} + \mathrm{p} \longrightarrow {}^{7}\mathrm{Be} \ + \ \mathrm{n} \text{ - } 1.65\ MeV \tag{1.3}$$

in which a proton impinges on a ^{7}Li and a ^{7}Be and a neutron are produced. The cross section for the reaction in reported in Figure 1.3. These energies are too high for the treatment, as the beam must meet quality standards as outlined in Table 1.2. In the table, ϕ_{epi} and ϕ_{th} represent the epithermal and thermal neutron flux, respectively. J indicates the neutron current, $\mathrm{D_H}$ represents the fast neutron dose, and D_γ stands for the gamma dose. To overcome these quality factors usually a Beam Shaping Assembly (BSA) is adopted. In Figure 1.4 an example of BSA is shown.

The main elements of a BSA are:

- moderator: made by MgF_2, AlF_3 or CaF in order to slow-down neutrons;
- reflector: made by Pb in order to maximize the neutron fluence in the region of interest;

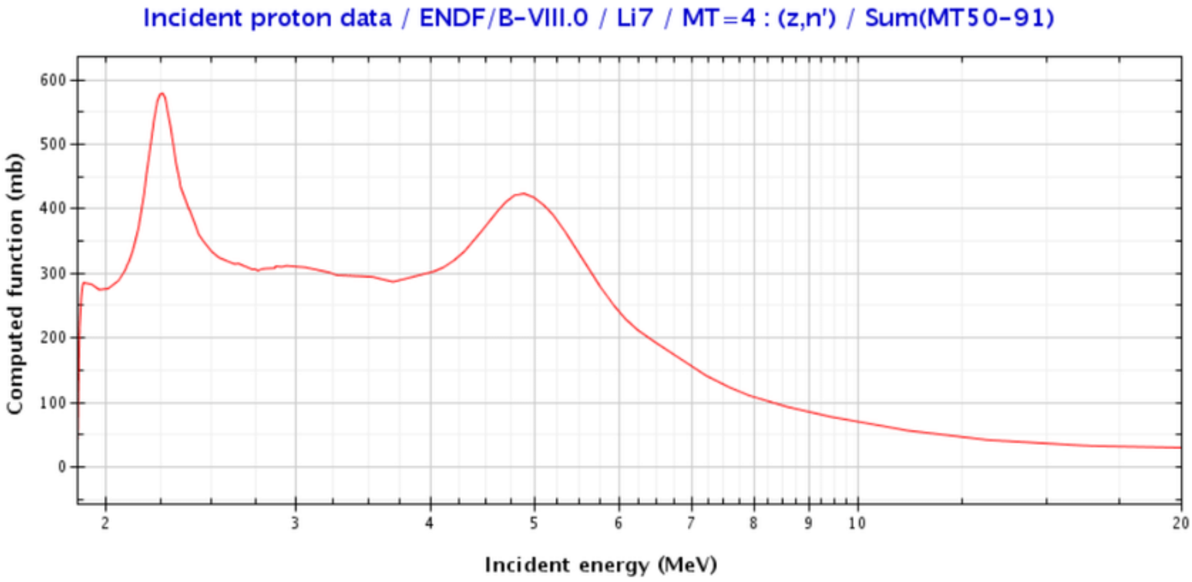

Figure 1.3: Cross section for $^{7}\mathrm{Li(p,n)}^{7}\mathrm{Be}$ reaction.

Table 1.2: Reference neutron beam quality factors [4].

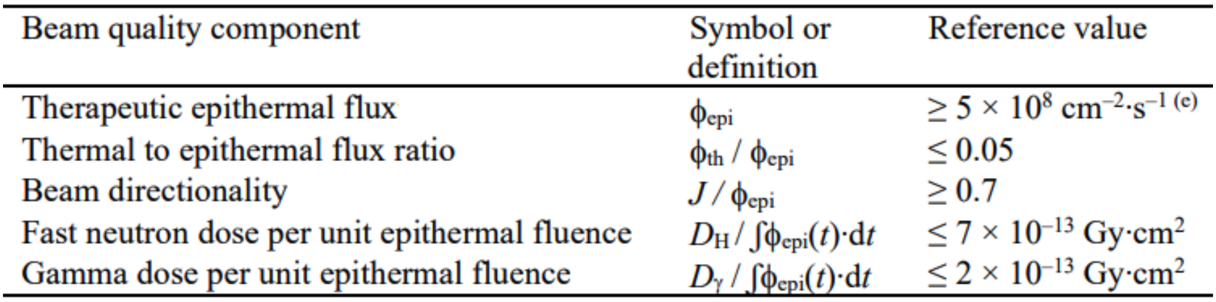

Beam quality component	Symbol or definition	Reference value
Therapeutic epithermal flux	ϕ_{epi}	$\geq 5 \times 10^{8}$ cm^{-2}·s^{-1} (e)
Thermal to epithermal flux ratio	ϕ_{th} / ϕ_{epi}	≤ 0.05
Beam directionality	J / ϕ_{epi}	≥ 0.7
Fast neutron dose per unit epithermal fluence	$D_{H} / \int \phi_{epi}(t) \cdot dt$	$\leq 7 \times 10^{-13}$ Gy·cm^{2}
Gamma dose per unit epithermal fluence	$D_{\gamma} / \int \phi_{epi}(t) \cdot dt$	$\leq 2 \times 10^{-13}$ Gy·cm^{2}

- thermal neutron filter made by Cd;
- gamma filter made by Pb in order to minimize photons generated by the interaction of neutrons with the moderator and the reflector;
- collimator in order to design the final beam shape for the treatment;

The BNCT facility at CNAO will be able to accelerate protons at 2.5 MeV with a maximum current around 10 mA.

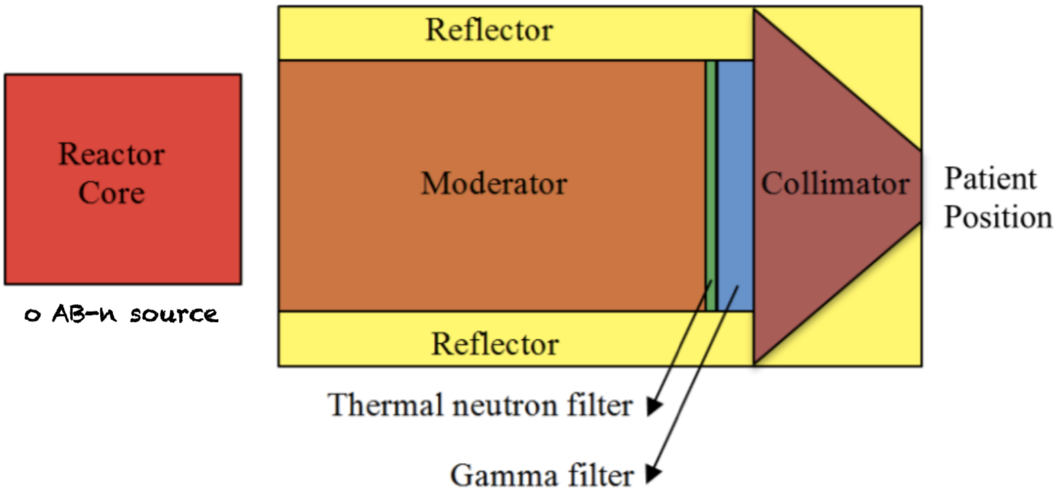

Figure 1.4: Beam Shaping Assembly design.

1.2 Radiation Protection Research at CNAO

As previously mentioned, the CNAO expansion project includes the installation of a new proton therapy facility with a rotating gantry and a BNCT facility. The design of these new facilities involves several studies to comply with the current regulations [5]. These research activities involve collaboration between CNAO and many universities, including Politecnico di Milano, University of Pavia, University of Milan, and University of Basilicata. The studies include radiation physics evaluations on the secondary field generated inside the synchrotron room, the maximum workloads allowed for the new ions listed in Table 2, and the shielding design of the BNCT facility. Other studies were conducted on the characterization of an extended-range rem counter for neutron dosimetry and its application in the BNCT field. Further assessments were dedicated to air activation problems at low distances and to water and material activations.

Throughout my doctoral studies, I had the opportunity to contribute to most of these projects, resulting in the publication of several master's theses. In the subsequent sections, a brief introduction to these studies is provided and the main results are presented. The final section in Chapter 1.3 outlines the objectives of this thesis.

1.2.1 Radiation Physics

One of the main issues of the radiation protection of high energy particle accelerators involves understanding the radiation fields generated by the machines installed in a facility. The beam losses produce a mixed high-energy secondary field dominated by neutrons up to hundreds of MeV and high-energy photons. In real cases, it can be challenging to assess radiation fields through simple calculations due to complexity of physical processes occurring for each interaction between particles. To obtain the required results, the radiation protection group at CNAO has utilized the Monte Carlo code FLUKA [6], [7] to create a highly precise geometry of the center, encompassing the existing synchrotron, the synchrotron with a rotating gantry, and the BNCT facility. The implemented geometry in FLUKA is depicted in Figure 1.5. As shown in Figure 1.5, the model takes into account

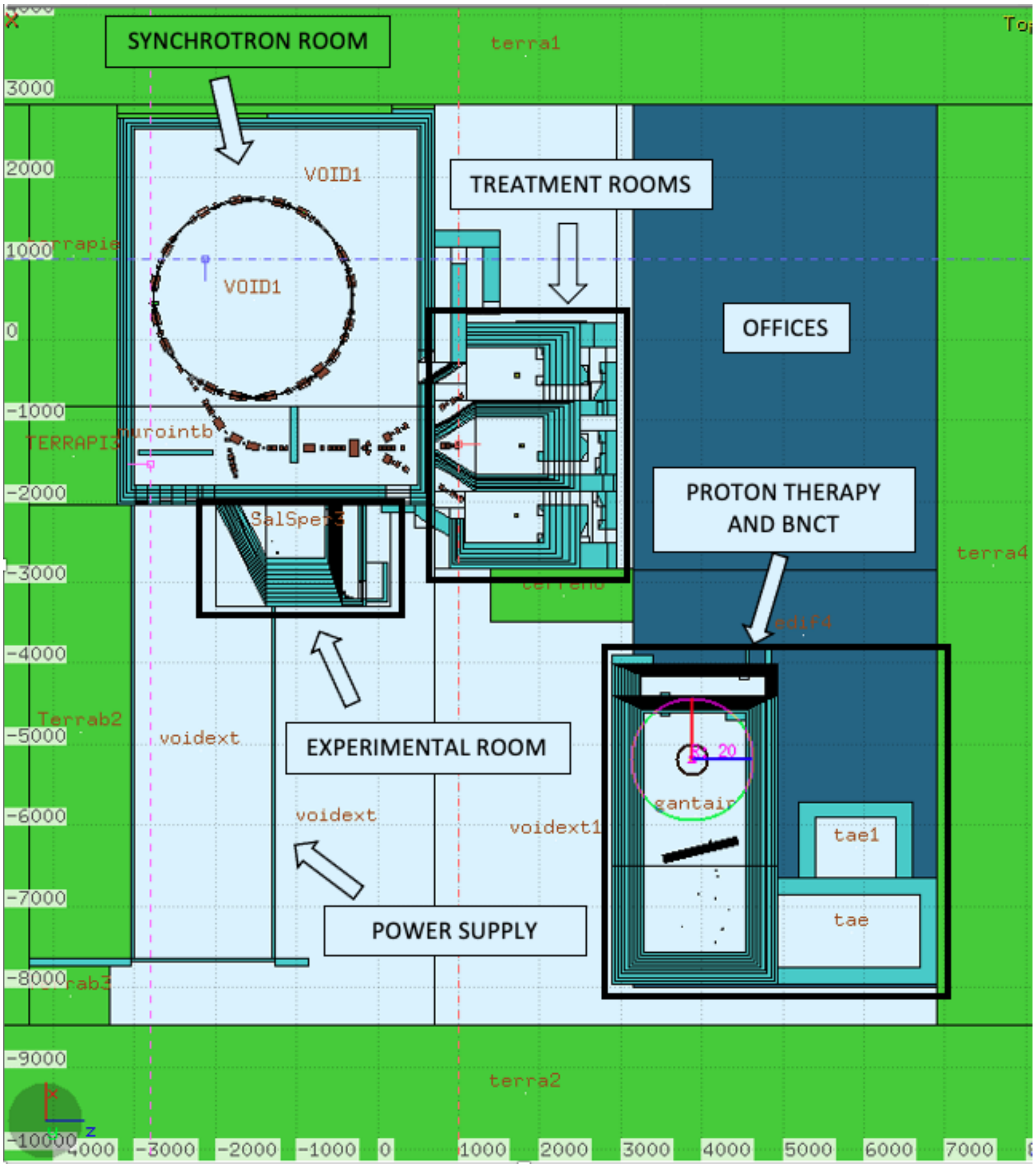

Figure 1.5: Geometry of CNAO implemented in FLUKA.

the total masses of the accelerator magnets to understand their influence on the radiation field and their shielding effect. The primary sources of dose outside the shielding are secondary neutrons generated through the interaction of the primary beam with machine components such as magnets and the vacuum chamber, as well as losses resulting from accidental injection and beam extraction, and losses on targets, including patients and experimental targets. For the existing synchrotron, a beam loss model has been implemented [8], [9]. This model simulates a total of 15 beam losses occurring tangentially to the accelerator's circumference. The primary beam impinges on copper, iron, or lead cubes, each measuring 10x10x10 cm^3, which represent elements of the accelerator machine. Additionally, three more losses are simulated, where a primary beam impacts the center of a 30x30x30 cm^3 water cube. The remaining four losses are implemented to take into account the four isocenters in the experimental room. In this model, approximately 50% of the losses originate from the experimental room and treatment rooms, while the remaining 50% are attributed to unintended losses in the beam pipe or on synchrotron elements. It's essential to stress that the model is designed with a strong emphasis on caution. The studies conducted for the ions listed in Table 1.1 using the beam loss model [8] consider two different geometries: one with all machine elements and another with just the vacuum chamber. In both cases, the secondary field inside the synchrotron room is primarily composed of neutrons and photons, with their spectra illustrated in Figure 1.6 and Figure 1.7. These figures display the spectra of neutrons and photons inside the shielding when the primary beam is composed of carbon ions. Notably, the presence of magnets attenuates the high-energy peak of neutrons centered around 100 MeV, while their influence on the photon spectrum is minimal. Neutron spectrum are characterized by three peaks: spallation peak around 100 MeV, evaporation peak around 1 MeV and thermal peak around eV. Photon spectra show peaks due to (n, γ) reactions on ^{1}H (2.2 MeV), ^{24}Mg (3.7 MeV), ^{23}Na (4.7 MeV), ^{28}Si (6.3 MeV), ^{27}Al (7.6 MeV), ^{40}Ca (6.3 MeV), ^{56}Fe (7.6 MeV) in concrete. The secondary field is similar for all beams and without magnets it is composed by ∼65% from neutrons, ∼30% from photons, and ∼5% from heavy ions; with magnets the heavy ion component can be neglected and the field is composed

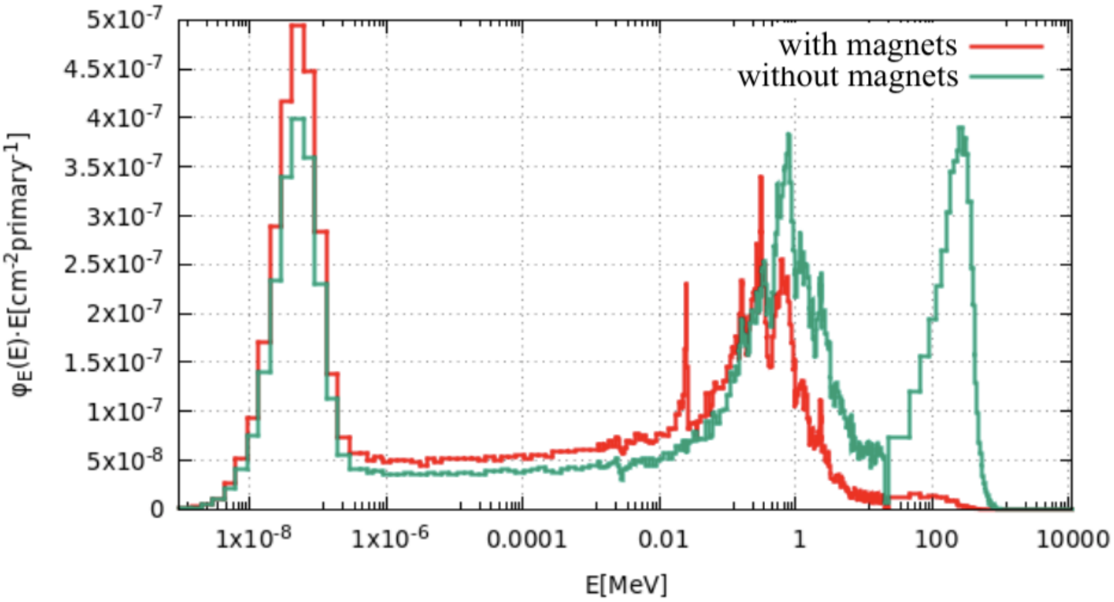

Figure 1.6: Neutron spectra generated inside the synchrotron room with and without magnets [8].

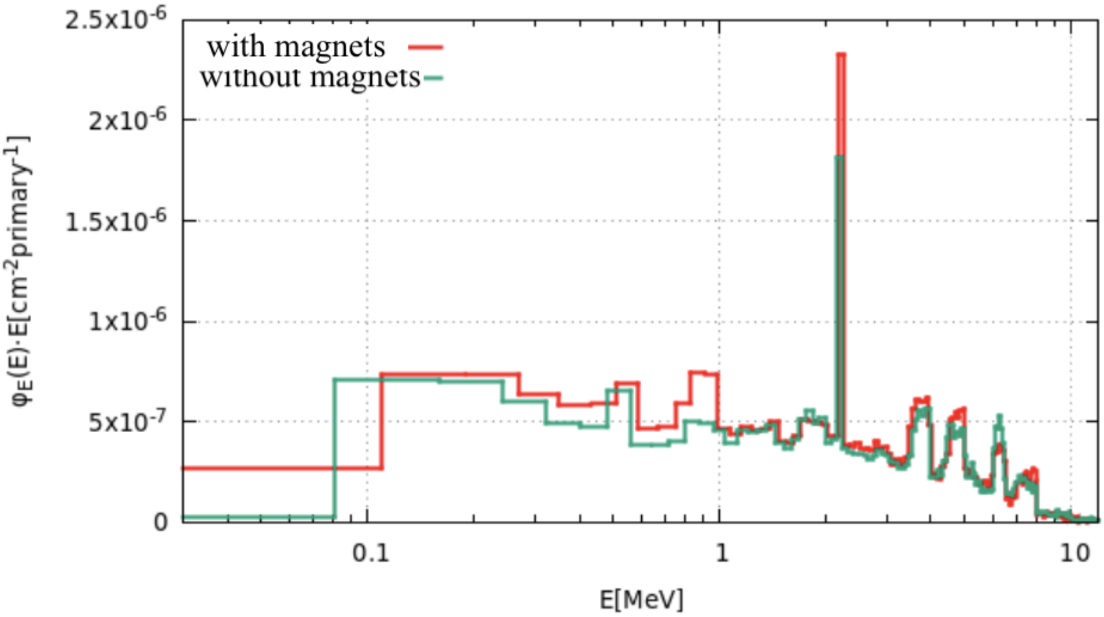

Figure 1.7: Photon spectra generated inside the synchrotron room with and without magnets [8].

by ∼70% from neutrons, ∼30% from photons.

Another issue that CNAO has tackled is defining the workloads for the new ions listed in Table 1.1, which will be accelerated in the existing synchrotron without alterations to the shielding. Typically, shielding is designed using Monte Carlo methods, often employing simplified models [10, 11, 12, 13, 14] or in a complete geometry considering the desired workload. During my master's thesis [15], I developed a simplified method to calculate both a maximum and a minimum value for the current of the new ions.

In the context of BNCT, studies were conducted to accurately assess the composition of the shielding [16]. Typically, in hadron therapy centers, shielding is designed with a focus on high-energy neutrons (> 1 MeV) and employs concrete walls. However, in the case of BNCT, the secondary radiation field is primarily composed of low-energy neutrons (< 100 keV), making it non-trivial to adopt the same shielding material. The main result of the thesis is that the inclusion of a first layer of concrete enriched with 1% boron offers significant advantages in meeting both radiation protection regulations and the desired workload. This is because boron has the capability to significantly reduce the thermal neutron scattering component within the treatment room.

1.2.2 Development of an Extended Range Rem Counter

The CNAO radiation protection group is involved in the development of a neutron dosimeter. Currently, on the market, there are rem counters that utilize gas thermal neutron detectors surrounded by plastic-based moderators. CNAO has chosen to develop their own rem counter to create an instrument that is cost-effective, easily repairable, and active. The instrument, depicted in Figure 1.8, consists of a solid-state thermal neutron semiconductor detector coupled with a Raspberry Pi and surrounded by a plastic-based moderator featuring cadmium and lead insertions to extend its range of response. Specifically, the rem counter operates without requiring high voltage, and it can be controlled solely by a Raspberry Pi, eliminating the necessity for an electronic chain involving amplification, a single-channel analyzer and a counter. CNAO already conducted studies on the instrument for the characterization of the first prototype [17] and its application in BNCT fields [18].

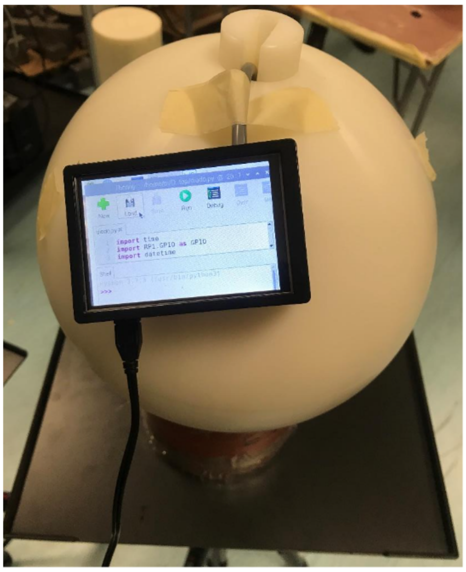

Figure 1.8: View of semiconductor-based rem counter [17].

1.2.3 Air Activation

Air activation poses a significant concern, particularly in the context of air release within synchrotron, experimental, and treatment rooms. Therefore, these rooms are equipped with systems for air exchange. Air can become activated both by the primary beam when it is unconfined in the air and by the secondary neutrons generated during the interaction between the primary beam and either the patient or the irradiated sample.

Recent studies conducted at CNAO [19] confirm that the main radionuclides generated by the primary beam are ^{13}N, ^{15}O, ^{11}C and the secondary neutrons generate the same radionuclides as the primary with the addition of the ^{41}Ar [19]. These radionuclides are the same for proton, helium, lithium, oxygen and iron primary beams.

In literature are available some models for air transport in the atmosphere [20]. The state of the art softwares are HotSpot [21] and Genii [22] that are widely used for air release problems in the atmosphere. It adopts a Gaussian Plume Model (GPM) and simplified meteorological conditions to evaluate ambient dose at a given distance from the emission stack. The model is highly reliable away from populated areas at distances >1 km, but as already mentioned CNAO is in a different position. Furthermore, it adopts dose conversion factors for dose assessments with nonzero values only inside the radioactive plume. In Figure 1.9 an aerial view of CNAO with the surrounding area with calculated distances from the synchrotron emission stack is reported. It can be seen from Figure 1.9 that distances from the synchrotron emission stack to hospitals, apartments and university are between 100-200 *m* so other models are needed. In particular, it has been conducted a comparison between HotSpot, Genii [22], a sphere model and a Monte Carlo model using FLUKA. In FLUKA it was implemented a transport of the radionuclide emissions (e.g. photons) from a gaussian plume. Results show a very good agreement at high distances

Symbol	Latitude	Longitude	Distance [m]	Description
S	45°12′04″N	9°8′40″E	-	Synchrotron emission stack
1	-	-	-	CNAO main entrance
2	-	-	-	Synchrotron bunker
A	45°12′01″N	9°8′38″E	127	Istituto Zooprofilattico Sperimentale
B	45°11′59″N	9°8′36″E	171	Apartment building
C	45°12′00″N	9°8′35″E	170	Apartment building
D	45°11′58″N	9°8′36″E	200	Avis comunale di Pavia
E	45°11′59″N	9°8′34″E	194	Apartment building
F	45°12′01″N	9°8′31″E	221	University of Pavia building
G	45°12′02″N	9°8′32″E	189	Nursing school
H	45°12′03″N	9°8′36″E	112	CNAO - High voltage control unit
J	45°12′04″N	9°8′47″E	159	Policlinico San Matteo - hospital
K	45°12′02″N	9°8′48″E	189	Policlinico San Matteo - hospital
L	45°12′02″N	9°8′45″E	143	Policlinico San Matteo - hospital
M	45°12′01″N	9°8′42″E	110	Policlinico San Matteo - hospital
N	45°11′58″N	9°8′41″E	182	Policlinico San Matteo - hospital

Figure 1.9: Aerial view of CNAO with the surrounding area. All distances are calculated from the S [23].

(few km) and a significant difference in the models at especially at low distances. In particular, it can be distinguished two scenarios [23]:

1. inside the plume: GPM models overestimate the ambient dose respect to the trasportation model (FLUKA);
2. outside the plume: GPM model evaluate null values in contrast of the transportation model.

CNAO is also conducting another study on air release at low distances in atmosphere using the computational fluid dynamics (CFD) software Ansys Fluent [24]. The idea is to implement a two step approach:

1. evaluate the radioactive plume dispersion using Ansys Fluent;
2. evaluate doses with the full transport model FLUKA.

Preliminary results show a good agreement of the CFD model and the GPM model at high distances [25].

1.2.4 Water and Materials Activation

Another field of study is the investigation on methodologies for the decommissioning of a facility. In literature are available computational studies on induced radioactivity in material considering hadron therapy beams and copper or stainless steel elements [26]. In fact, copper and stainless steel are the most adopted materials to simulate respectively accelerator elements and the beam pipe. Nevertheless, it is difficult to find data on the specific beams adopted in the CNAO expansion project. The radiation protection team at CNAO conducted studies [27], [28] on the beams reported in Table 1.1 in order to expand literature data. Data were particularly valuable for the BNCT facilities were a 1% of deviation of the thermal neutron inside the treatment room can be very impacting.

Further studies were dedicated to the water activation and tritium measurements for the actual synchrotron, the protontherapy and the BNCT facility [29], since very few useful data are available on the argument. The study take into account the radioactivity producted in the cooling circuit pipes by beam losses with the same beam loss model adopted in other thesis. Data from Monte Carlo simulations indicate that tritium concentration is not a cause for concern in the context of the new proton therapy, BNCT facility, and the current synchrotron, whether using protons, carbon ions, helium, lithium, oxygen, or iron ions.

1.3 Aim of the Thesis

In the previous paragraph, we introduced the state of the art in radiation protection studies relevant to CNAO. The following chapters of this thesis are dedicated to the three main aspects addressed in this work: radiation physics studies dedicated for helium, lithium, oxygen and iron ions (new ions in the following) to be accelerated in the actual CNAO synchrotron; the development of a extended range rem counter based on a Micro Structured Neutron Detector (MSND) and the experimental campaigns in order to test the detector.

1.3.1 Radiation Physics Studies

The radiation physics studies chapter can be divided into two different sections:

- Line of sight model
- Simulations performed in CNAO center with the Monte Carlo code FLUKA

The purpose of this chapter is to calculate the maximum current at which the new ions can be accelerated using two different methods. In both approaches, the doses produced by the new ions are compared to those of carbon ions, which are already accelerated at CNAO. By establishing the ratio between a specific ion and carbon ions, it becomes possible to estimate the radiological impact of the new ion in the current synchrotron. Multiplying this ratio by the maximum current allowed for carbon ions provides a way to calculate the maximum current for the new ions. The radiation protection studies were conducted with ions at their maximum energy, chosen for precautionary reasons.

From a radiation protection perspective, the primary concern in designing the shielding of a hadron therapy center is managing beam losses. These losses can be intentional, directed at the patient, or unintended, involving losses on a magnet or a component of the synchrotron. Modeling this aspect is quite challenging since it typically depends on various factors that can vary, ranging from the magnetic field design to the energy of the lost particle. In this thesis, two different approaches have been explored.

Line of Sight Model

The first approach uses the line of sight model, where a single beam loss is modeled using a Monte Carlo code. By determining the locations of beam losses in the machine and their proportions relative to the total number of accelerated particles, it becomes possible to assess the required shielding for a center. The geometry involves a pencil beam impacting either an iron target or an ICRU-tissue target, simulating a beam loss on a magnet or a patient, respectively. Subsequently, the secondary radiation is shielded by 6-meter of concrete. In this thesis, the secondary neutron field is evaluated in terms of neutron energy distributions. Additionally, attenuation curves for these neutrons are calculated to compare the results of a specific ion with respect to carbon ions after passing through a given thickness of concrete.

Monte Carlo simulations of CNAO center

The second approach involves investigating the ambient dose equivalent in a model of the CNAO center, as presented in Section 2.4.1, using the beam loss model detailed in Section 2.4.2. With this implementation, it's possible to conduct simulations for each new ion and compare their doses at selected points relative to those of carbon ions. Finally, in Section 2.4.5, dose maps featuring the assessed maximum doses for each ion are presented.

1.3.2 Development of a Extended Range Rem Counter

Following a brief introduction to rem counters, the implementation of the extended range rem counter is presented. This implementation involves the MSND connected to the General Purpose Input Output (GPIO) pins of the Raspberry Pi, enclosed within a polyethylene sphere with cadmium and lead insertions.

In this thesis, both the counting and visualization codes, written in C and Python, have been implemented. The final integral codes are provided in Appendix B.1. Multiple Python and C codes were tested to determine if the Raspberry Pi can effectively process signals from the MSND. For testing the codes, an Arduino was used to generate square waves at various frequencies

Using the Monte Carlo code FLUKA, the response function of the detector has been assessed. The simulations involved a broad beam interacting with the extended range rem counter, collecting counts for 55 different energies. The outcome of each simulation is the detector's counts corresponding to a specific energy.

Lastly, at the Czech Institute of Metrology, the detector was calibrated using an Am-Be source, and a linearity test of the detector was conducted.

1.3.3 Experimental Campaigns at Cern and at CNAO

After calibration, the detector was tested at two facilities at CERN and at CNAO. At CERN, access to two distinct facilities was available: the calibration room, equipped with multiple Am-Be sources to assess the detector's response, and the Cerf facility, offering various neutron fields, as described in the literature [30]. At CERF, the response of the detector in intense fields was evaluated by comparing the experimental results with those reported in the literature. Given the detector's reliability in CERF fields, measurements at CNAO were conducted within the synchrotron room. The results were then compared to Monte Carlo simulations of the center, incorporating the previously mentioned beam loss model.

2 | Radiation Physics Studies on New Ions

This chapter focuses on radiation physics investigations with the aim of calculating the maximum current for accelerating new ions in the existing synchrotron facility. Currently, the center is authorized to accelerate protons up to 250 MeV and carbon ions up to 400 MeV/u. In the near future, the facility will also accelerate helium, lithium, oxygen, and iron ions for both therapeutic treatments and research, outlined in Table 1.1. The current shielding design of the center is configured to handle up to $1.26{\cdot}10^{16}$ carbon ions per year and up to $3.15{\cdot}10^{17}$ protons per year for therapy and research. To determine the number of particles per year that can be accelerated within the existing shielding without necessitating changes to the current shielding. This approach is crucial because the sources required to produce the new ions (helium, lithium, oxygen, iron) cannot be adopted until they receive approval from the relevant Italian authorities, in accordance with Italian radiation protection legislation [5].

The research has been carried out by reccuring to Monte Carlo methods and the FLUKA code [6] , [7]. Two different groups of simulations have been conducted:

- Line of sight model to evaluate the production of secondary neutrons and assess attenuation curves of the new ions.
- Monte Carlo geometry of the center to test the maximum permissible currents.

Line of sight model aimed to yield data that could be applicable to new hydrotherapy centers, providing valuable insights for their operations. On the other hand, the second set of simulations was employed for the authorization procedures for CNAO. Prior to delving into simulations, this chapter provides a concise introduction to nuclear reactions at hadron therapy energies and an overview of the Monte Carlo code FLUKA. It is essential to note that Monte Carlo codes stand as the most robust tools for simulating the complex set of nuclear reactions involved in hadron therapy.

2.1 Nuclear Reactions at Hadron Therapy Energies

Nuclear reactions are classified considering their characteristics. In this thesis the same nomenclature in the textbook [31] has been adopted, focusing on the classification by particle exchange and mechanism.

Classification by Particle Exchanges

Generally, a nuclear reaction can be written as:

$$\mathrm{X(a,b)Y} \tag{2.1}$$

where X is the target nucleus, a is the incoming particle, Y and b are the reaction products. From this simple equation a first classification can be made:

- Elastic scattering reaction: if X=Y and a=b with Y and b are in ground state.
- Inestatic scattering reaction: if X=Y and a=b with Y or b are in an excited state.
- Knockout reaction: if more than one nucleon is ejected from the nucleus.
- Transfer reaction: if one or more nucleons are transferred between the incoming particle and the target.

An interesting transfer reaction is the radiative capture that often occur for thermal neutrons and can be expressed with:

$$\mathrm{X(n,\gamma)Y} \tag{2.2}$$

in which the atomic number of the target in the final state is increased by one and a photon is emitted from the target.

Classification by Mechanism

Nuclear reactions can also be classified based on the mechanisms that occur during the process, and they can be broadly categorized as follows:

- Direct reactions: few nucleons of the target interact with the projectile and the incoming energy is distributed into those few nucleons.
- Compound nucleus: the projectile and the target merge together into the so-called compound nucleus and the energy of the incoming particle is shared. After 10^{-16} s - 10^{-18} s one or more nucleons are emitted from the compound nucleus and the final equilibrium state for the target is reached.
- Resonance reactions: the projectile and the target form a "quasibound" state before one particle is emitted.

In a direct reaction the incident particle interacts with one or very few nucleons inside the target nucleus. This kind of reactions is most likely to happen at energies over a tens of MeV since the De Broglie wavelength allows the projectile to interact with individual nucleons inside the target. These reactions are very fast (10^{-22} s) and the distribution of the ejected nucleons is peaked in the forward direction.

When the energy of the incident particle is in the MeV range, its De Broglie wavelength is comparable to the nucleus dimension and the formation of the compound nucleus can occur. In this reaction the energy of the projectile is shared through all the nucleons inside the nucleus. The time scale of the reaction is smaller than the direct reaction and it is around 10^{-16} s - 10^{-18} s. The final products of the reaction are independent from their formation and the decay probability into a final state depends mainly on the total energy of the system by statistical rules. The angular distribution of the ejected particles is almost isotropic. After the compound nucleus reactions, the de-excitation of residual nucleus occurs, in which γ emissions allow the nucleus to reach its ground state. Usually, heavy nuclei emission can be assumed to be continuous, while for light nuclei less nuclear states are available and the emission is commonly considered to be discrete.

Resonance reaction and resonance peaks are visible at low excitation energies during the compound nucleus. In fact at high energies ($>$100 keV), nuclear states are closely spaced and the result is a continuum emission of nucleons as function of energy. At lower energies, the gap between the states is larger and typical resonance peaks are visible.

Spallation reactions

Nuclear interactions that occur at hadron therapy energies are commonly known as spallation reactions [32]. When a hadron at hadron therapy energy impinges on a target, a two step process take place: the first is the intranuclear cascade in which scattering processes occur and high energy neutrons, protons and pions ($>$20 MeV) are emitted from the nucleus (direct reactions). After these interactions, the nucleus is left in an excited state and compound nucleus and resonance reactions occur. Secondaries emitted from a spallation reaction can generate a series of spallation reactions inducing a process known as hadronic cascade.

Models for nuclear reactions

In the last section, nuclear reactions for hadrons impinging on a target have been described. In Monte Carlo codes some models are adopted for spallation reactions. In particular, the Monte Carlo code adopted in this thesis, FLUKA, uses a collection of models known as intranuclear cascade models that follows 4 steps:

- Direct hadron-nucleon interactions: above 200 MeV.
- Pre-equilibrium stage: between 50-200 MeV.
- Evaporation: below 50 MeV.
- De-excitation of residual nucleus: for the final emission of photons.

2.2 The Monte Carlo code FLUKA

Monte Carlo method represents a broad class of computational algorithms that rely on random sampling to solve problems that might be deterministic in principle. Monte Carlo methods have a wide variety of applications from the calculation of π to the development of atomic weapons. In the first paragraph a mathematical introduction to the Monte Carlo code is given adopting a similar description presented in the text book [33]. The chapter continues with an overview on FLUKA capabilities and the physics implemented in the Monte Carlo code [34, 35, 7, 6].

Mathematical introduction to Monte Carlo

Consider a random variable $T = f(X_1, ..., X_k)$ function of k random variables $(X_1, ..., X_k)$. The mean value of T, I, can be expressed as:

$$I = \int_D f(x_1, ..., x_k) p(x_1, ..., x_k)\ dx_1 ... dx_k, \tag{2.3}$$

where $p(x_1, ..., x_k)$ is the normalized probability density of the variables $(X_1, ..., X_k)$ defined in the domain D in $\mathbb{R}^k$. Monte Carlo codes generate a sample of N random variables (or events) T from the probability density $p(x_1, ..., x_k)$ with a mean value:

$$T_N = \frac{1}{N} \sum_{i=1}^{N} f(x_{1i}, ..., x_{ki}) \tag{2.4}$$

Applying the Central Limit Theory, it can be shown, that if $N > 10$ the probability density of the random variable T_N converges to I with standard deviation $\frac{\sigma_T}{\sqrt{N}}$.

The statistical error of T_N depend s on the inverse of the square of N and the convergence can be very slow. In order to improve this trend some variance techniques are often implemented in Monte Carlo codes [36].

2.2.1 FLUKA Input file Overview

As reported in FLUKA manual [37]:

> *FLUKA is a general purpose tool for calculations of particle transport and interactions with matter, covering an extended range of applications spanning from proton and electron accelerator shielding to target design, calorimetry, activation, dosimetry, detector design, Accelerator Driven Systems, cosmic rays, neutrino physics, radiotherapy etc.*

FLUKA `CARDS` can be implemented from a text file or through the FLUKA input interface Flair [38]. The input procedure can be divided into 8 main sections that contains a series of FLUKA `CARDS`:

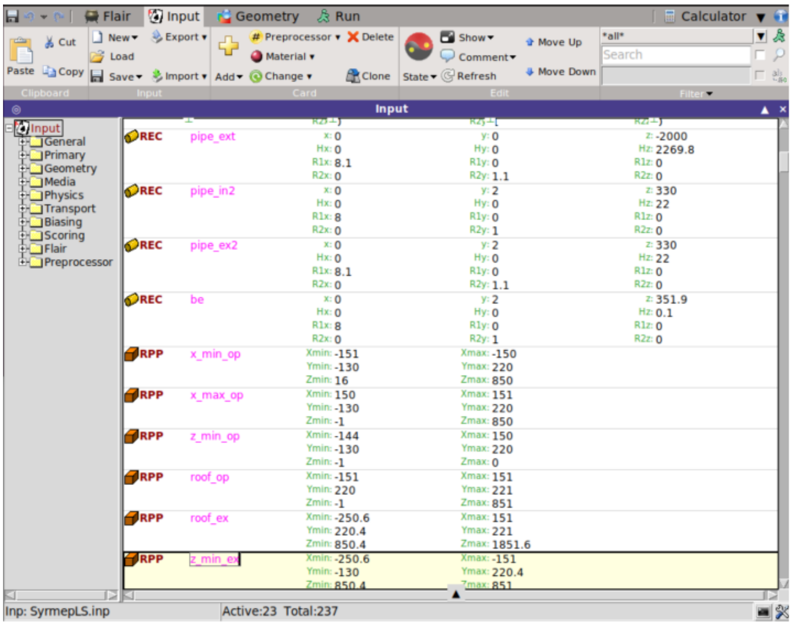

```
REC   pipe_ext     x: 0        y: 0        z: -2000
                  Hx: 0       Hy: 0       Hz: 2269.8
                 R1x: 8.1    R1y: 0      R1z: 0
                 R2x: 0      R2y: 1.1    R2z: 0
REC   pipe_in2     x: 0        y: 2        z: 330
                  Hx: 0       Hy: 0       Hz: 22
                 R1x: 8      R1y: 0      R1z: 0
                 R2x: 0      R2y: 1      R2z: 0
REC   pipe_ex2     x: 0        y: 2        z: 330
                  Hx: 0       Hy: 0       Hz: 22
                 R1x: 8.1    R1y: 0      R1z: 0
                 R2x: 0      R2y: 1.1    R2z: 0
REC   be           x: 0        y: 2        z: 351.9
                  Hx: 0       Hy: 0       Hz: 0.1
                 R1x: 8      R1y: 0      R1z: 0
                 R2x: 0      R2y: 1      R2z: 0
RPP   x_min_op  Xmin: -151   Xmax: -150
                Ymin: -130   Ymax: 220
                Zmin: 16     Zmax: 850
RPP   x_max_op  Xmin: 150    Xmax: 151
                Ymin: -130   Ymax: 220
                Zmin: -1     Zmax: 850
RPP   z_min_op  Xmin: -144   Xmax: 150
                Ymin: -130   Ymax: 220
                Zmin: -1     Zmax: 0
RPP   roof_op   Xmin: -151   Xmax: 151
                Ymin: 220    Ymax: 221
                Zmin: -1     Zmax: 851
RPP   roof_ex   Xmin: -250.6 Xmax: 151
                Ymin: 220.4  Ymax: 221
                Zmin: 850.4  Zmax: 1851.6
RPP   z_min_ex  Xmin: -250.6 Xmax: -151
                Ymin: -130   Ymax: 220.4
                Zmin: 850.4  Zmax: 851
```

Inp: SyrmepLS.inp Active:23 Total:237

Figure 2.1: Flair input interface.

- General
- Primary
- Geometry
- Media
- Physics
- Transport
- Biasing
- Scoring

FLUKA `CARDS` can be implemented from a text file or through the FLUKA input interface Flair [38]. An example of Flair input is reported in Figure 2.1. In the following paragraphs a basic set of FLUKA `CARDS` for each section are introduced.

General

- `DEFAULTS`: allow the user to call a series of physical and transport options based on the application.

Primary

- `BEAM`: defines the dimension and the energy/momentum of the beam.

- `BEAMPOSIt`: defines the position and the direction of the physical beam.
- `SOURCE`: enables the introduction of a user-written beam source.

Geometry

- `BODY`: basic geometric elements that can be intersected, joined or subtracted to build more complicated geometries.
- `REGION`: geometric structures build by the intersection, the union and the subtraction of bodies.

Media

- `MATERIAL`: defines a user-define material with its properties.
- `COMPOUND`: allows the user to define a compound from isotopes.
- `ASSINGMAt`: allows the user to assign a material to a region.
- `LOW-MAT`: allows the user to assign the low energy neutrons (<20 MeV) cross-section data for a material.

Physics

- `PHYSICS`: allows the user to activate physical models.

Transport

- `RADDECAY`: activates the radioactive decay in the simulation.
- `IRRPROFIle`: defines an irradiation profile in a simulation with radioactive decays.
- `DCYTIMES`: defines cooling times for scoring cards n a simulation with radioactive decays.
- `EMF`: allows the user to activate the electromagnetic transport.
- `EMFCUT`: allows the user to set thresholds for electromagnetic transport.

Biasing

- `BIASING`: defines importance on region or particle basis.

Scoring

- `USRBIN`: scores particle fluence, dose, ambient dose equivalent, effective dose on region basis or on a user defined grid independent from the geometry.
- `USRBDX`: scores particle fluence or current at the boundary between two regions.
- `USRTRACK`: scores track-length fluences.
- `RESNUCLEi`: evaluates radionuclides generated by a simulation after a cooling time defined by `DCYTIMES` and applied by `DCYSCORE`.
- `DCYSCORE`: associates to a scoring `CARD` a time defined by `DCYTIMES`.
- `USERDUMP`: defines a collision tape and enables the call of user-written detector.

2.2.2 FLUKA Physics Overview

FLUKA adopts several physical models and algorithms. A complete overview can be find in [39]. In this thesis, a brief description of the main models is reported with all needed references for an in-depth study.

Electromagnetic interaction

FLUKA is able to transport photons and electron from 1 PeV to 1 keV. For photoelectric, pair production and total coherent effect the EPDL97 [40] photon cross section library is adopted. Also the breemstrahlung, electron pairs and the Landau-Pomeranchuk-Migdal effect are implemented.

Charged particle interaction

The scattering of charged particles is described by a Multiple scattering algorithm [41] and the ionization losses are implemented through the statistical approach described in [42].

Hadron-nucleus interactions

Hadron-nucleus interaction are described with different models based on the energy of the hadron. For energies over few *GeV* the Dual Parton Model is adopted [43]; for lower energies the transport is performed through isobar model [44, 45]. Lowering the energy hadron-nucleus collisions can be described as many hadron-hadron interactions and the PEANUT model is adopted [46, 47, 48]. The intronuclear cascade processes are described by the Generalized IntraNuclear Cascade (GINC) model inside the PEANUT model. The GINC model handles the transport of all nucleons with energies over 50 MeV and until all generated particles (except nucleons) have been emitted or absorbed. The

PEANUT model include equilibrium processes: evaporation (based on the Weisskopt-Ewing approach), fission, gamma de-excitation and the Fermi break-up model.

Low energy neutrons

Low energy neutron transport is handled by a multi-group algorithm. Group cross sections are based on cross section databases ENDF, JENDL, JEFF. In the case of ^{1}H, ^{6}Li, ^{40}Ar elements and ^{10}B(n,α)^{7}Li, ^{14}N(n,p)^{14}C reactions, pointwise cross sections are adopted. Also, photon generation by low energy neutrons is treated recurring to the energy group model through a downscattering matrix.

Nucleus-nucleus interactions

Different models, based on energy range classification, are adopted to simulate nucleus-nucleus reactions:

- $E > 5$ GeV/u: DMPJET-III model [49];
- 1 GeV/u $< E < 5$ GeV/u: Relativistic Quantum Molecular Dynamics model [50, 51];
- $E < 1$ GeV/u: Bolzmann Master Equation [52].

2.3 Line of Sight Model Implementation

Attenuation of secondaries generated by ion beam interaction with targets have been widely investigated, in particular on protons ranging from 100 MeV to 250 MeV [53], and also on heavier ions ranging from helium to uranium ions [10, 11, 12, 13, 14]. Line of sight models are conducted under uniform conditions, involving an ion beam impinging on a thick iron, copper, water, or ICRU tissue cube or cylinder, utilizing Monte Carlo simulations. The secondary particles produced are then transported through spherical concrete shielding, varying in thickness from 1 to 8 meters, and at different angles. Ambient dose equivalent values, denoted as $H^{*}(10)$, are assessed in these scenarios. The simulations allow for the calculation of secondary neutron emissions from the target materials and the attenuation curves of $H^{*}(10)$. These data can be employed for an initial estimation in the design of shielding for a hadron therapy center. In this chapter, the data published in the paper [54], conducted in collaboration with the CNAO radiation protection group, University of Pavia, and University of Basilicata, are presented. This includes neutron yields, neutron energy distributions, attenuation curves, and the introduction of the equivalent carbon ratio, denoted as ξ. This ratio is calculated by dividing the ambient dose equivalent value of an ion at a specific point in the shielding by the value for carbon ions. Since ion currents are proportional to the ambient dose equivalent, this ratio allows us to assess the impact of new ions on existing shielding. The study covers ions listed in Table 2.1, providing information on ion beams, beam energy, and the lengths of iron and ICRU tissue targets. The paper follows the same methodologies as the work in [10], which are described in detail in the text.

Table 2.1: List of ions with corresponding energies and iron target lengths considered in the present work.

Ion	**Beam Energy [MeV/u]**	**Iron Length [cm]**	**ICRU Length [cm]**
^{4}He	250	8.3	46.93
^{7}Li	306	9	51.08
^{12}C	400	6.11	34.83
^{16}O	400	4.5	25.67
^{56}Fe	306	1	5.61

2.3.1 Monte Carlo Model

Geometry

The geometry adopted for the simulation with the Monte Carlo code FLUKA is reported in Figure 2.2. In the center, a thick iron or ICRU tissue target is positioned, enclosed by a concrete spherical shielding with a thickness of 6 meters and a inner radius of 90 meters. The ion beam impacts the center of the target, as illustrated in Figure 2.2, and the target thickness exceeds the ion beam range in the target calculated with SRIM [55] by 20%. Table 2.1 provides a list of the ion beams and target configurations used in the simulations.

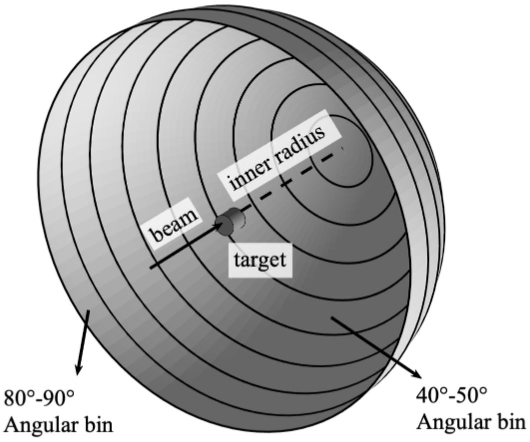

Figure 2.2: Geometry adopted for the simulations [54].

The concrete shielding has the composition detailed in Table 2.2 and is divided into 21 radii, starting from an inner radius of 90 cm, along with 18 angular bins. Each of the

Table 2.2: Concrete composition with a density 2.3 g/cm^3.

Element	Weight Fraction
H	0.010
C	0.001
O	0.529
Na	0.016
Mg	0.002
Al	0.034
Si	0.337
K	0.013
Ca	0.044
Fe	0.014

378 sections features a 10° aperture in both the planar and azimuth coordinates, and they all possess a uniform thickness of 30 cm. The geometry section of the input file can be divide into:

- 20 concentric spheres for the shielding;
- 1 cylinder for the target;
- 17 circular truncated cones in order to split the shielding in angular regions;
- 360 `regions` to split each concrete shell in angular bins (0°-10°, 10°-20°, etc..).

Methodology

The appropriate methodology for evaluating an attenuation curve involves running individual simulations for every angular bin and thickness, subsequently fitting the data to a parametric curve. For each ion-target combination, Monte Carlo simulations have been carried out for each region in order to obtain acccurate values of doses and fluences. By using this approach consider the interaction of secondaries with either the outer or lateral sections of the shielding could be taken into accout, potentially causing back-scatter or cross-talk effects in the scoring region. To mitigate these effects, the following strategies are employed:

- to avoid the cross-talk effect: the inner radius of the shielding is chosen of 90 m.
- to avoid the back-scattering: a user's routine that modify the normal scoring of FLUKA is implemented.

The routine is written in Fortran and has the capability to modify the default behavior of the `USRBDX` card. Specifically, it considers only the initial passage of a particle between two regions when evaluating fluence. This approach effectively eliminates back-scattering events, as any physical back-scattering that may occur does not influence the fluence scoring. The input configuration comprises 18 `USRBDX` cards used to score neutron energy distribution for each angular bin emitted from the target, along with 378 `USRBDX` cards employed to calculate the ambient dose equivalent values at the boundaries of each concrete shell for all angular bins (18 angular bins x 21 boundaries). To activate the Fortran routine, the `USRWEIG` card is used.

Furthermore, to enhance the statistical accuracy of the simulations, the Russian roulette and splitting geometry techniques are employed, and the importance values of regions are assigned using a `BIASING` card. Specifically, when a primary or secondary particle crosses the boundary between two regions, two events can occur:

- the particle importance of the first region is lower than the second: the geometry splitting occurs and the particle population decrease proportionally to to the ratio between regions.
- the particle importance of the first region is higher than the second: the Russian roulette occurs and the particle population increase proportionally to the ratio between regions.

The suggested approach in literature is to chose the importance in order to have a constant particle fluence in the whole shielding.

2.3.2 Results

The results of the simulations are presented in three main sections: neutron energy distributions, attenuation curves, and equivalent carbon ratios. Specifically, neutron yields have been calculated and neutron energy distribution are shown at different angles respect to the beam. In addition, ambient dose equivalent values have been assessed in order to calculate attenuation curves for helium at 250 MeV/u, lithium at 306 MeV/u, oxygen at 400 MeV/u and iron ions at 400 MeV/u. Lastly, using the attenuation curves data, the equivalent carbon ratio ξ at different angular bin and shielding thicknesses has been calculated. Tables and plots of ξ are then reported.

Neutron Energy Distribution

Typically, the neutron yield, which represents the number of neutrons emitted for each primary particle, and the neutron energy distribution are quantities required to evalaute the shielding. By multiplying the neutron yield by the ion current, the total number of neutrons emitted at a specific angle respect to the beam direction can be calculated. The neutron yield per primary particle of the beam is provided in Tables 2.3 and 2.4.

From Tables 2.3 and 2.4, it is evident that, based on the assumptions made in this study, iron targets produce more secondary neutrons than ICRU tissue targets. Neutron yields provide information about the total number of neutrons, without offering any details about their energy distribution.

Table 2.3: Neutron yields emitted from the iron target for selected ion beams in Table 2.1.

Ion	**Beam Energy [MeV/u]**	**Yield**	**Err%**
^{4}He	250	2.93	0.18
^{7}Li	306	6.44	0.11
^{12}C	400	7.08	0.11
^{16}O	400	6.41	0.19
^{56}Fe	306	3.07	0.21

Table 2.4: Neutron yields emitted from the ICRU tissue target for ion beams in Table 2.1.

Ion	**Beam Energy [MeV/u]**	**Yield**	**Err%**
^{4}He	250	1.18	0.18
^{7}Li	306	2.78	0.10
^{12}C	400	3.68	0.10
^{16}O	400	3.69	0.12
^{56}Fe	306	2.61	0.25

In Figure 2.3, the neutron energy distribution evaluated for the beams and targets listed in Table 2.1 is depicted in a lethargy plot. Notably, one can distinguish the spallation peak (around 100 MeV/u) and the evaporation peak (around 1 MeV/u) for all ion-target combinations, as well as a thermal peak (around 10^{-7} MeV/u) for the ICRU tissue target combinations. Figure 2.3 illustrates that the energy distribution exhibits a complex trend as a function of the particle's atomic number (Z), but some behaviors can be highlighted:

- the spallation neutron emission in the forward angle is strongly depend on the Z of the particle.
- the evaporation and thermal emissions can be considered isotropic for angular bins higher that 40°-50°.
- the emission of neutrons from iron beams depends strongly from the angular bin, while for other ions is almost isotropic.

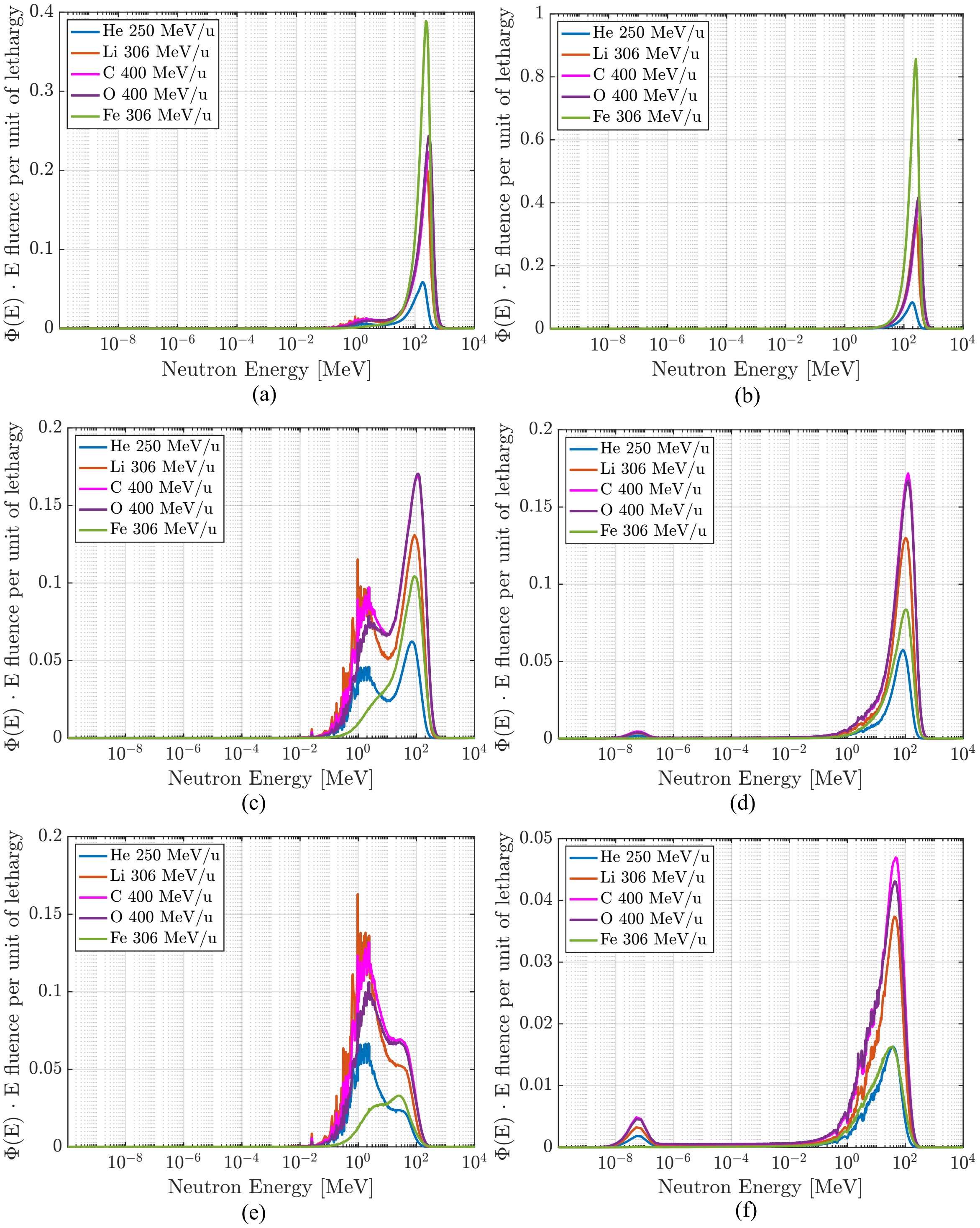

Figure 2.3: Neutron energy distributions for ions and iron (a), (c), (e) or ICRU tissue (b), (d), (f) targets list in Table 2.1. (a) Neutron energy distribution at 0°–10° angular bin with the iron targets. (b) Neutron energy distribution at 0°–10° angular bin with ICRU targets. (c) Neutron energy distribution at 40°-50° angular bin with the iron targets. (d) Neutron energy distribution at 40°–50° angular bin with ICRU targets. (e) Neutron energy distribution at 80°–90° angular bin with the iron targets. (f) Neutron energy distribution at 80°–90° angular bin with ICRU targets. [54].

Attenuation Curves

Attenuation curves are evaluated fitting ambient dose equivalent values at each boundary in the concrete shielding. The two fitting parameter formula is adopted:

$$H^*(10)(d)\, r^2 = H_0\, e^{-\rho \frac{d}{\lambda}}, \tag{2.5}$$

where $H^*(10)(d)$ is the ambient dose equivalent evalutated at the shielding thickness d, r is the distance between the center of the spherical shielding, ρ is the density of the shielding (2.3 g/cm^3) and H_0 and λ are respectively the source term expressed in [Sv·m^2] and the attenuation lengths expressed in [g/cm^2]. Usually, in literature a two attenuation curves approach is adopted: for shallow penetration H_1 and λ_1 are calculated and for deeper thicknesses H_2 and λ_2 are adopted. In particular from Figure 2.4, the attenuation curve can be divided into two different equilibrium regions one up to 1.20 m with H_1 and λ_1 and the other from 1.20 m and 6 m with H_2 and λ_2. The complete set of attenuation parameters calculated through simulations are presented in the Appendix A of the paper [54] and the parameters for carbon and iron ions for the iron targets are reported in Tables 2.5 and 2.6. These values are used in the next paragraph to evaluate equivalent carbon ratios.

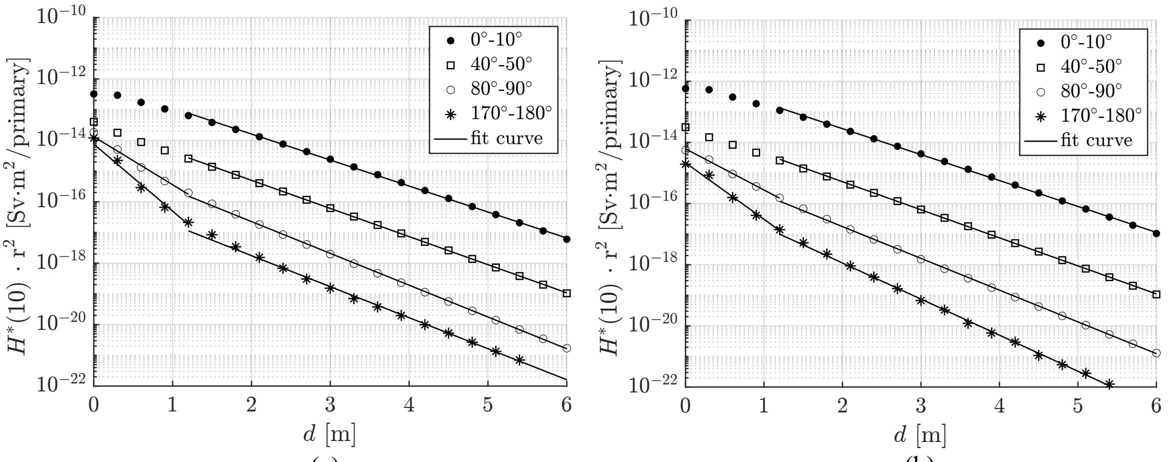

(a) (b)

Figure 2.4: Attenuation curves of ambient dose equivalent in concrete for 400 MeV/u carbon ions impinging on an iron target (a) and ICRU tissue target (b), for four representative angular bins [54].

Table 2.5: Values of fitting parameters H_1, λ_1, H_2, λ_2 for the carbon 400 MeV/u beam impinging on iron target.

Angular Bin	**H_1 [Sv·m^2]**	**Err%**	**λ_1 [g/cm^2]**	**Err%**	**H_2 [Sv·m^2]**	**Err%**	**λ_2 [g/cm^2]**	**Err%**
0°-10°	-	-	-	-	$8.0 \cdot 10^{-13}$	0.2	120.0	1
10°-20°	-	-	-	-	$2.5 \cdot 10^{-13}$	0.2	119.9	1
20°-30°	-	-	-	-	$1.1 \cdot 10^{-13}$	0.1	117.6	1
30°-40°	-	-	-	-	$6.1 \cdot 10^{-14}$	0.1	114.4	0.4
40°-50°	-	-	-	-	$3.4 \cdot 10^{-14}$	0.1	110.9	0.2
50°-60°	-	-	-	-	$1.8 \cdot 10^{-14}$	0.01	107.2	0.03
60°-70°	-	-	-	-	$9.6 \cdot 10^{-15}$	0.05	103.9	0.2
70°-80°	$1.7 \cdot 10^{-14}$	1	70.9	6	$4.9 \cdot 10^{-15}$	0.1	101.2	0.3
80°-90°	$1.3 \cdot 10^{-14}$	1	64.9	7	$2.7 \cdot 10^{-15}$	0.1	98.1	0.4
90°-100°	$1.2 \cdot 10^{-14}$	1	58.5	8	$1.5 \cdot 10^{-15}$	0.2	95.8	1
100°-110°	$1.1 \cdot 10^{-14}$	1	53.9	7	$8.6 \cdot 10^{-16}$	0.2	94.4	1
110°-120°	$8.7 \cdot 10^{-15}$	1	52.6	8	$5.8 \cdot 10^{-16}$	0.3	93.4	1
120°-130°	$8.2 \cdot 10^{-15}$	1	50.1	8	$4.2 \cdot 10^{-16}$	0.3	93.3	1
130°-140°	$7.2 \cdot 10^{-15}$	1	49.5	9	$3.3 \cdot 10^{-16}$	0.3	92.8	1
140°-150°	$6.9 \cdot 10^{-15}$	1	48.6	9	$2.6 \cdot 10^{-16}$	0.3	94.4	1
150°-160°	$6.7 \cdot 10^{-15}$	1	48.1	9	$2.3 \cdot 10^{-16}$	0.3	95.7	1
160°-170°	$7.4 \cdot 10^{-15}$	1	47.1	9	$1.8 \cdot 10^{-16}$	0.3	99.2	1
170°-180°	$7.5 \cdot 10^{-15}$	1	46.6	9	$1.8 \cdot 10^{-16}$	0.4	100.6	1

Table 2.6: Values of fitting parameters H_1, λ_1, H_2, λ_2 for the iron 306 MeV/u beam impinging on iron target.

Angular Bin	**H_1 [Sv·m^2]**	**Err%**	**λ_1 [g/cm^2]**	**Err%**	**H_2 [Sv·m^2]**	**Err%**	**λ_2 [g/cm^2]**	**Err%**
0°-10°	-	-	-	-	$1.1\cdot10^{-12}$	0.2	116.8	1
10°-20°	-	-	-	-	$2.5\cdot10^{-13}$	0.1	116.8	1
20°-30°	-	-	-	-	$7.9\cdot10^{-14}$	0.1	115.0	0.4
30°-40°	-	-	-	-	$3.4\cdot10^{-14}$	0.1	112.1	0.2
40°-50°	-	-	-	-	$1.7\cdot10^{-14}$	0.02	108.7	0.1
50°-60°	-	-	-	-	$7.7\cdot10^{-15}$	0.05	105.4	0.2
60°-70°	-	-	-	-	$3.5\cdot10^{-15}$	0.1	103.2	0.3
70°-80°	$7.2\cdot10^{-15}$	0.5	68.3	5	$1.6\cdot10^{-15}$	0.1	102.2	0.4
80°-90°	$5.3\cdot10^{-15}$	1	63.3	5	$8.1\cdot10^{-16}$	0.2	101.8	1
90°-100°	$4.0\cdot10^{-15}$	1	60.2	6	$4.7\cdot10^{-16}$	0.2	102.0	1
100°-110°	$3.2\cdot10^{-15}$	1	57.9	8	$3.2\cdot10^{-16}$	0.2	101.3	1
110°-120°	$2.8\cdot10^{-15}$	1	55.2	8	$2.2\cdot10^{-16}$	0.2	101.6	1
120°-130°	$2.6\cdot10^{-15}$	1	53.8	8	$1.8\cdot10^{-16}$	0.2	100.9	1
130°-140°	$2.3\cdot10^{-15}$	1	53.5	8	$1.5\cdot10^{-16}$	0.2	100.1	1
140°-150°	$2.1\cdot10^{-15}$	1	52.6	8	$1.3\cdot10^{-16}$	0.2	99.1	1
150°-160°	$2.2\cdot10^{-15}$	1	51.3	8	$1.2\cdot10^{-16}$	0.2	99.1	1
160°-170°	$2.0\cdot10^{-15}$	1	51.5	8	$1.2\cdot10^{-16}$	0.2	96.8	1
170°-180°	$2.0\cdot10^{-15}$	1	51.3	9	$1.5\cdot10^{-16}$	0.1	96.4	0.4

Equivalent Carbon Ratio

The equivalent carbon ratio is defined mathematically as follows [54]:

$$\xi = \frac{H^*(10)_{ion}}{H^*(10)_{Cion}}, \tag{2.6}$$

where $H^*(10)_{ion}$ and $H^*(10)_{Cion}$ are respectively the ambient dose equivalent for the ion of interest and for carbon ions in a given point of the shielding.

This ratio has been calculated using the attenuation curves with the attenuation parameters determined in the last paragraph. It applies to ion species listed in Table 2.1 and for angular bins provided in Tables 2.5 and 2.6. The complete set of results is published in Appendix B and presented in this thesis in Tables 2.9 to 2.16 at the end of the paragraph. Additionally, Tables 2.7 and 2.8 display the minimum, maximum, and the ratio between the minimum and the maximum (ratio) for iron and ICRU tissue targets. The carbon ratio provides insights into the physics of an ion in comparison to carbon ions. Specifically, it takes into account neutron generation and their attenuation in concrete. It is evident from Tables 2.7 and 2.8 that oxygen ions exhibit similar behaviors to iron ions for both types of targets.

Table 2.7: Minimum, maximum and ratio between minimum and maximum of ξ considering iron targets and beams listed in Table 2.1.

Ion Beam	**Energy [MeV/u]**	**Min**	**Max**	**Ratio**
^{4}He	250	$5.89{\cdot}10^{-2}$	$2.96{\cdot}10^{-1}$	5.0
^{7}Li	306	$1.80{\cdot}10^{-1}$	$7.12{\cdot}10^{-1}$	4.0
^{16}O	400	$9.38{\cdot}10^{-1}$	1.63	1.7
^{56}Fe	306	$3.20{\cdot}10^{-1}$	1.35	4.2

Table 2.8: Minimum, maximum and ratio between minimum and maximum of ξ considering ICRU tissue targets and beams listed in Table 2.1.

Ion Beam	**Energy [MeV/u]**	**Min**	**Max**	**Ratio**
^{4}He	250	$5.89{\cdot}10^{-2}$	$2.36{\cdot}10^{-1}$	4.0
^{7}Li	306	$3.93{\cdot}10^{-1}$	$6.59{\cdot}10^{-1}$	1.7
^{16}O	400	$8.76{\cdot}10^{-1}$	1.22	1.4
^{56}Fe	306	$2.50{\cdot}10^{-1}$	1.38	5.5

The equivalent carbon ratios can be plotted considering two functional dependencies:

1. as function of the thickness of the concrete shielding in Figure 2.5 in a fixed angular bin;
2. as function of the angle in Figure 2.6 for a fixed concrete depth;

Figures 2.5 to 2.6 yield important insights. Notably, the equivalent carbon ratio exceeds 1 only when the atomic number (Z) of the ion beam overtakes that of carbon ions, and this pattern is not consistent across all angles or concrete thicknesses. Another noteworthy trend is that the carbon ratio for iron ions spans a broader range of values compared to other ions, primarily due to the wide variability in their neutron production across different angular bins.

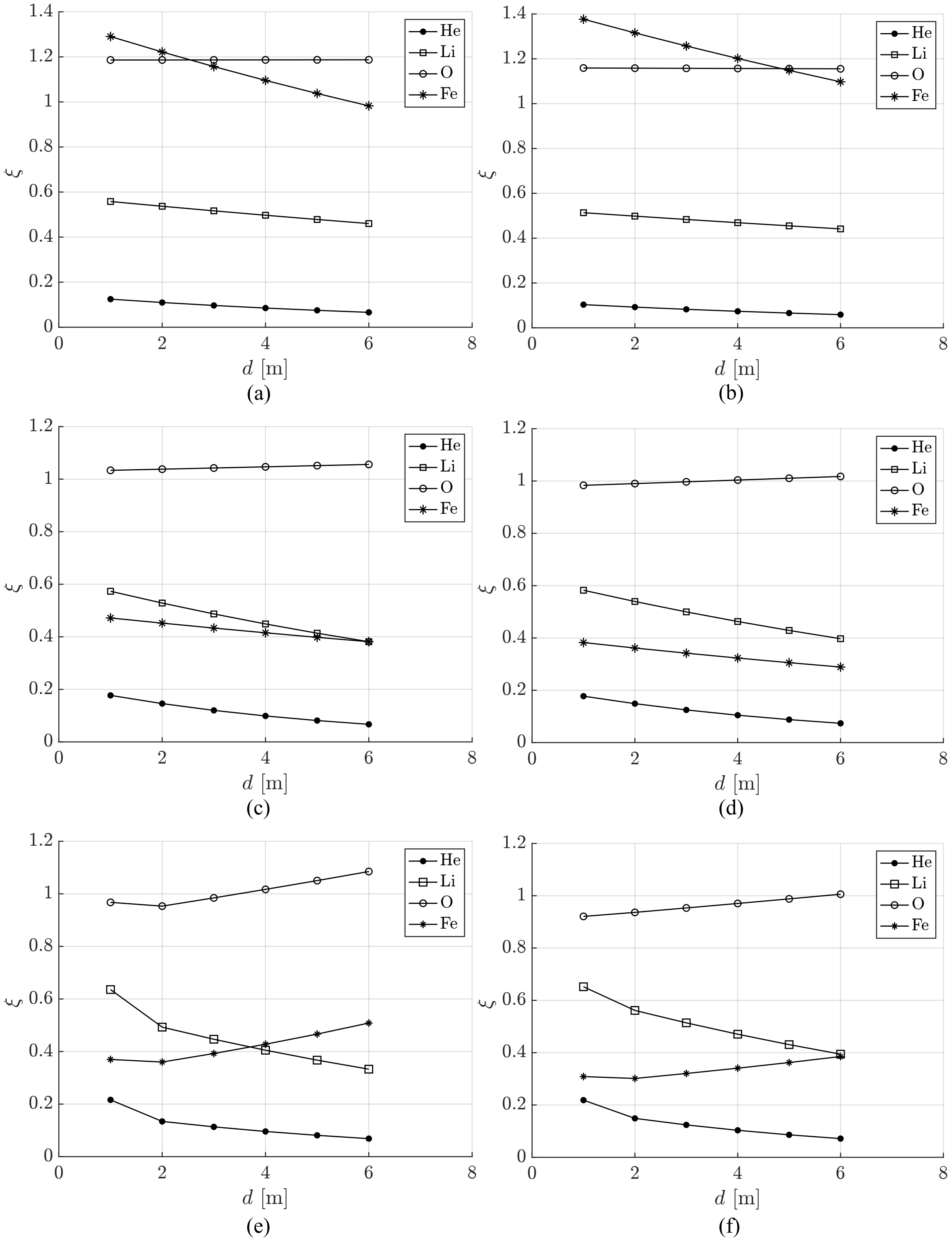

Figure 2.5: ξ as function of concrete thickness for ions and iron (a), (c), (e) or ICRU tissue (b), (d), (f) targets list in Table 2.1. (a) ξ at 0°–10° angular bin with the iron targets as function of concrete thickness. (b) ξ at 0°–10° angular bin with ICRU targets as function of concrete thickness. (c) ξ at 40°-50° angular bin with the iron targets as function of concrete thickness. (d) ξ at 40°–50° angular bin with ICRU targets as function of concrete thickness. (e) ξ at 80°–90° angular bin with the iron targets as function of concrete thickness. (f) ξn at 80°–90° angular bin with ICRU targets as function of concrete thickness. [54].

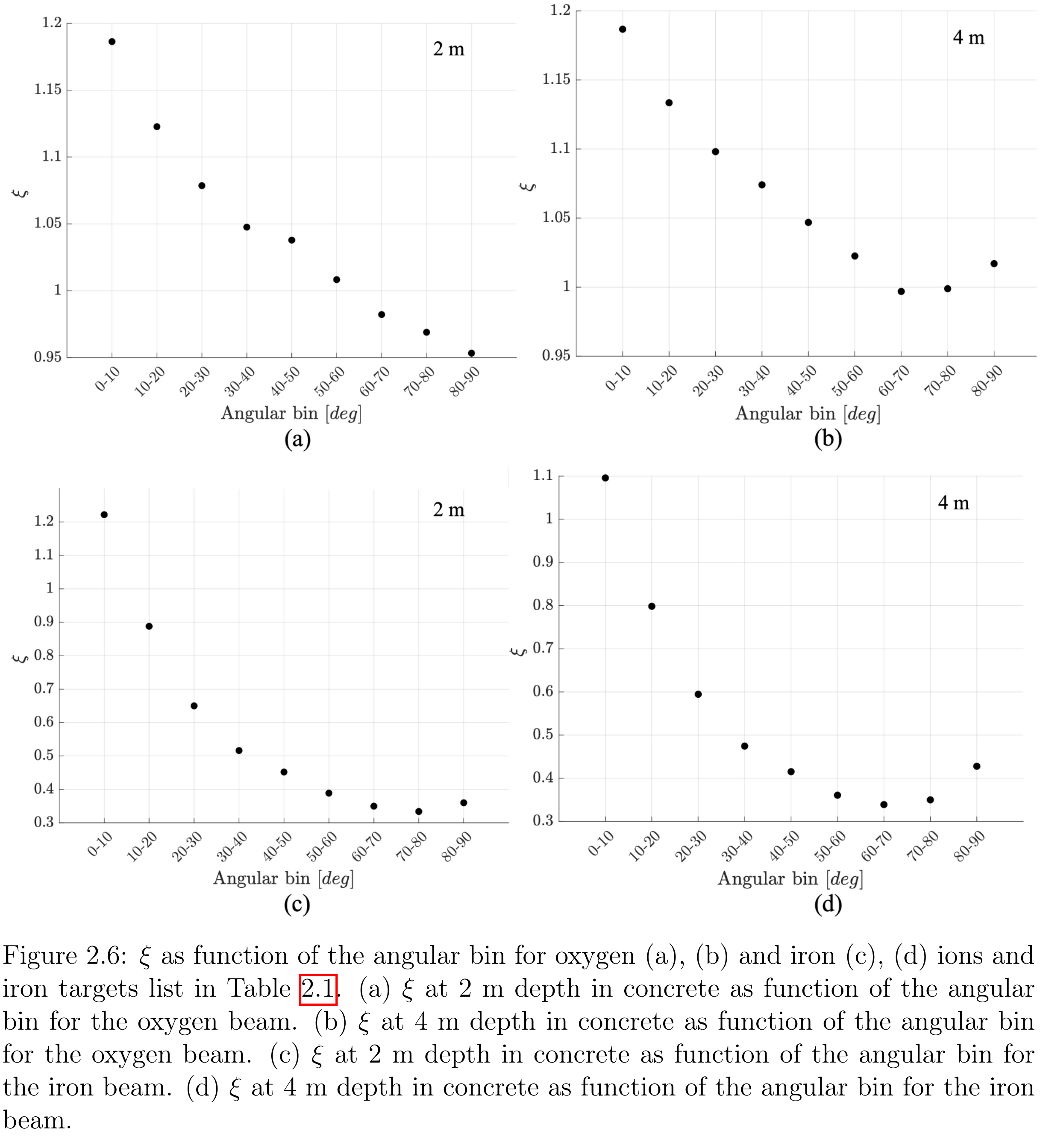

(a) (b) (c) (d)

Figure 2.6: ξ as function of the angular bin for oxygen (a), (b) and iron (c), (d) ions and iron targets list in Table 2.1. (a) ξ at 2 m depth in concrete as function of the angular bin for the oxygen beam. (b) ξ at 4 m depth in concrete as function of the angular bin for the oxygen beam. (c) ξ at 2 m depth in concrete as function of the angular bin for the iron beam. (d) ξ at 4 m depth in concrete as function of the angular bin for the iron beam.

Equivalent Carbon Ratio Data

Table 2.9: ξ ratios for the helium 250 MeV/u beam for the iron target.

Angular Bin	**1 m**	**2 m**	**3 m**	**4 m**	**5 m**	**6 m**
0°-10°	$1.29\cdot10^{-1}$	$1.09\cdot10^{-1}$	$9.60\cdot10^{-2}$	$8.45\cdot10^{-2}$	$7.44\cdot10^{-2}$	$6.55\cdot10^{-2}$
10°-20°	$1.97\cdot10^{-1}$	$1.53\cdot10^{-1}$	$1.31\cdot10^{-1}$	$1.13\cdot10^{-1}$	$9.70\cdot10^{-2}$	$8.34\cdot10^{-2}$
20°-30°	$2.12\cdot10^{-1}$	$1.58\cdot10^{-1}$	$1.33\cdot10^{-1}$	$1.13\cdot10^{-1}$	$9.57\cdot10^{-2}$	$8.10\cdot10^{-2}$
30°-40°	$2.10\cdot10^{-1}$	$1.48\cdot10^{-1}$	$1.24\cdot10^{-1}$	$1.04\cdot10^{-1}$	$8.69\cdot10^{-2}$	$7.29\cdot10^{-2}$
40°-50°	$2.12\cdot10^{-1}$	$1.45\cdot10^{-1}$	$1.20\cdot10^{-1}$	$9.88\cdot10^{-2}$	$8.14\cdot10^{-2}$	$6.71\cdot10^{-2}$
50°-60°	$2.09\cdot10^{-1}$	$1.40\cdot10^{-1}$	$1.14\cdot10^{-1}$	$9.35\cdot10^{-2}$	$7.63\cdot10^{-2}$	$6.24\cdot10^{-2}$
60°-70°	$2.16\cdot10^{-1}$	$1.35\cdot10^{-1}$	$1.10\cdot10^{-1}$	$9.01\cdot10^{-2}$	$7.35\cdot10^{-2}$	$5.99\cdot10^{-2}$
70°-80°	$2.19\cdot10^{-1}$	$1.36\cdot10^{-1}$	$1.11\cdot10^{-1}$	$8.98\cdot10^{-2}$	$7.28\cdot10^{-2}$	$5.90\cdot10^{-2}$
80°-90°	$2.15\cdot10^{-1}$	$1.31\cdot10^{-1}$	$1.12\cdot10^{-1}$	$9.61\cdot10^{-2}$	$8.24\cdot10^{-2}$	$7.06\cdot10^{-2}$
90°-100°	$2.30\cdot10^{-1}$	$1.32\cdot10^{-1}$	$1.19\cdot10^{-1}$	$1.07\cdot10^{-1}$	$9.61\cdot10^{-2}$	$8.65\cdot10^{-2}$
100°-110°	$2.40\cdot10^{-1}$	$1.59\cdot10^{-1}$	$1.46\cdot10^{-1}$	$1.34\cdot10^{-1}$	$1.23\cdot10^{-1}$	$1.13\cdot10^{-1}$
110°-120°	$2.40\cdot10^{-1}$	$1.79\cdot10^{-1}$	$1.67\cdot10^{-1}$	$1.56\cdot10^{-1}$	$1.45\cdot10^{-1}$	$1.36\cdot10^{-1}$
120°-130°	$2.71\cdot10^{-1}$	$1.91\cdot10^{-1}$	$1.74\cdot10^{-1}$	$1.58\cdot10^{-1}$	$1.44\cdot10^{-1}$	$1.31\cdot10^{-1}$
130°-140°	$2.85\cdot10^{-1}$	$2.05\cdot10^{-1}$	$1.88\cdot10^{-1}$	$1.72\cdot10^{-1}$	$1.58\cdot10^{-1}$	$1.45\cdot10^{-1}$
140°-150°	$2.87\cdot10^{-1}$	$2.07\cdot10^{-1}$	$1.88\cdot10^{-1}$	$1.70\cdot10^{-1}$	$1.54\cdot10^{-1}$	$1.40\cdot10^{-1}$
150°-160°	$2.95\cdot10^{-1}$	$2.47\cdot10^{-1}$	$2.11\cdot10^{-1}$	$1.81\cdot10^{-1}$	$1.55\cdot10^{-1}$	$1.33\cdot10^{-1}$
160°-170°	$2.92\cdot10^{-1}$	$2.49\cdot10^{-1}$	$1.75\cdot10^{-1}$	$1.23\cdot10^{-1}$	$8.68\cdot10^{-2}$	$6.11\cdot10^{-2}$
170°-180°	$2.92\cdot10^{-1}$	$2.14\cdot10^{-1}$	$1.08\cdot10^{-1}$	$5.49\cdot10^{-2}$	$2.78\cdot10^{-2}$	$1.41\cdot10^{-2}$

Table 2.10: ξ ratios for the lithium 306 MeV/u beam for the iron target.

Angular Bin	**1 m**	**2 m**	**3 m**	**4 m**	**5 m**	**6 m**
0°-10°	$5.37\cdot10^{-1}$	$5.37\cdot10^{-1}$	$5.17\cdot10^{-1}$	$4.97\cdot10^{-1}$	$4.78\cdot10^{-1}$	$4.60\cdot10^{-1}$
10°-20°	$6.34\cdot10^{-1}$	$5.80\cdot10^{-1}$	$5.51\cdot10^{-1}$	$5.24\cdot10^{-1}$	$4.98\cdot10^{-1}$	$4.73\cdot10^{-1}$
20°-30°	$6.27\cdot10^{-1}$	$5.63\cdot10^{-1}$	$5.27\cdot10^{-1}$	$4.94\cdot10^{-1}$	$4.63\cdot10^{-1}$	$4.34\cdot10^{-1}$
30°-40°	$6.05\cdot10^{-1}$	$5.26\cdot10^{-1}$	$4.90\cdot10^{-1}$	$4.57\cdot10^{-1}$	$4.26\cdot10^{-1}$	$3.97\cdot10^{-1}$
40°-50°	$6.11\cdot10^{-1}$	$5.28\cdot10^{-1}$	$4.87\cdot10^{-1}$	$4.49\cdot10^{-1}$	$4.14\cdot10^{-1}$	$3.81\cdot10^{-1}$
50°-60°	$6.17\cdot10^{-1}$	$5.19\cdot10^{-1}$	$4.74\cdot10^{-1}$	$4.34\cdot10^{-1}$	$3.97\cdot10^{-1}$	$3.63\cdot10^{-1}$
60°-70°	$6.33\cdot10^{-1}$	$5.14\cdot10^{-1}$	$4.67\cdot10^{-1}$	$4.25\cdot10^{-1}$	$3.86\cdot10^{-1}$	$3.51\cdot10^{-1}$
70°-80°	$6.14\cdot10^{-1}$	$5.03\cdot10^{-1}$	$4.59\cdot10^{-1}$	$4.18\cdot10^{-1}$	$3.81\cdot10^{-1}$	$3.48\cdot10^{-1}$
80°-90°	$6.36\cdot10^{-1}$	$4.93\cdot10^{-1}$	$4.47\cdot10^{-1}$	$4.05\cdot10^{-1}$	$3.67\cdot10^{-1}$	$3.33\cdot10^{-1}$
90°-100°	$6.41\cdot10^{-1}$	$4.90\cdot10^{-1}$	$4.53\cdot10^{-1}$	$4.18\cdot10^{-1}$	$3.86\cdot10^{-1}$	$3.57\cdot10^{-1}$
100°-110°	$6.81\cdot10^{-1}$	$5.30\cdot10^{-1}$	$4.84\cdot10^{-1}$	$4.41\cdot10^{-1}$	$4.03\cdot10^{-1}$	$3.68\cdot10^{-1}$
110°-120°	$6.58\cdot10^{-1}$	$4.93\cdot10^{-1}$	$4.74\cdot10^{-1}$	$4.55\cdot10^{-1}$	$4.37\cdot10^{-1}$	$4.20\cdot10^{-1}$
120°-130°	$6.63\cdot10^{-1}$	$5.06\cdot10^{-1}$	$4.69\cdot10^{-1}$	$4.35\cdot10^{-1}$	$4.03\cdot10^{-1}$	$3.74\cdot10^{-1}$
130°-140°	$6.58\cdot10^{-1}$	$5.04\cdot10^{-1}$	$4.92\cdot10^{-1}$	$4.80\cdot10^{-1}$	$4.68\cdot10^{-1}$	$4.56\cdot10^{-1}$
140°-150°	$7.12\cdot10^{-1}$	$5.42\cdot10^{-1}$	$5.11\cdot10^{-1}$	$4.82\cdot10^{-1}$	$4.55\cdot10^{-1}$	$4.29\cdot10^{-1}$
150°-160°	$6.85\cdot10^{-1}$	$4.98\cdot10^{-1}$	$4.43\cdot10^{-1}$	$3.94\cdot10^{-1}$	$3.51\cdot10^{-1}$	$3.12\cdot10^{-1}$
160°-170°	$6.63\cdot10^{-1}$	$4.87\cdot10^{-1}$	$4.24\cdot10^{-1}$	$3.69\cdot10^{-1}$	$3.22\cdot10^{-1}$	$2.80\cdot10^{-1}$
170°-180°	$6.54\cdot10^{-1}$	$5.66\cdot10^{-1}$	$4.24\cdot10^{-1}$	$3.17\cdot10^{-1}$	$2.38\cdot10^{-1}$	$1.78\cdot10^{-1}$

Table 2.11: ξ ratios for the oxygen 400 MeV/u beam for the iron target.

Angular Bin	**1 m**	**2 m**	**3 m**	**4 m**	**5 m**	**6 m**
0°-10°	1.22	1.19	1.19	1.19	1.19	1.19
10°-20°	1.12	1.12	1.13	1.13	1.14	1.14
20°-30°	1.07	1.08	1.09	1.10	1.11	1.12
30°-40°	1.05	1.05	1.06	1.07	1.09	1.10
40°-50°	1.02	1.04	1.04	1.05	1.05	1.06
50°-60°	$9.92\cdot10^{-1}$	1.01	1.02	1.02	1.03	1.04
60°-70°	$9.84\cdot10^{-1}$	$9.82\cdot10^{-1}$	$9.90\cdot10^{-1}$	$9.97\cdot10^{-1}$	1.00	1.01
70°-80°	$9.84\cdot10^{-1}$	$9.69\cdot10^{-1}$	$9.84\cdot10^{-1}$	$9.99\cdot10^{-1}$	1.01	1.03
80°-90°	$9.68\cdot10^{-1}$	$9.53\cdot10^{-1}$	$9.85\cdot10^{-1}$	1.02	1.05	1.08
90°-100°	$9.84\cdot10^{-1}$	$9.92\cdot10^{-1}$	1.02	1.05	1.09	1.12
100°-110°	$9.78\cdot10^{-1}$	1.04	1.08	1.12	1.16	1.20
110°-120°	$9.87\cdot10^{-1}$	1.05	1.05	1.05	1.06	1.06
120°-130°	$9.38\cdot10^{-1}$	1.03	1.07	1.11	1.16	1.20
130°-140°	1.01	1.18	1.25	1.33	1.42	1.51
140°-150°	1.03	1.21	1.22	1.22	1.22	1.23
150°-160°	$9.71\cdot10^{-1}$	1.15	1.24	1.34	1.45	1.57
160°-170°	1.03	1.45	1.36	1.28	1.20	1.12
170°-180°	1.03	1.14	1.14	1.14	1.14	1.14

Table 2.12: ξ ratios for the iron 306 MeV/u beam for the iron target.

Angular Bin	**1 m**	**2 m**	**3 m**	**4 m**	**5 m**	**6 m**
0°-10°	1.33	1.22	1.16	1.10	1.04	$9.83\cdot10^{-1}$
10°-20°	$9.62\cdot10^{-1}$	$8.88\cdot10^{-1}$	$8.42\cdot10^{-1}$	$7.98\cdot10^{-1}$	$7.57\cdot10^{-1}$	$7.18\cdot10^{-1}$
20°-30°	$6.96\cdot10^{-1}$	$6.50\cdot10^{-1}$	$6.22\cdot10^{-1}$	$5.95\cdot10^{-1}$	$5.69\cdot10^{-1}$	$5.44\cdot10^{-1}$
30°-40°	$5.66\cdot10^{-1}$	$5.16\cdot10^{-1}$	$4.95\cdot10^{-1}$	$4.74\cdot10^{-1}$	$4.55\cdot10^{-1}$	$4.36\cdot10^{-1}$
40°-50°	$4.98\cdot10^{-1}$	$4.52\cdot10^{-1}$	$4.33\cdot10^{-1}$	$4.15\cdot10^{-1}$	$3.98\cdot10^{-1}$	$3.81\cdot10^{-1}$
50°-60°	$4.39\cdot10^{-1}$	$3.89\cdot10^{-1}$	$3.75\cdot10^{-1}$	$3.61\cdot10^{-1}$	$3.47\cdot10^{-1}$	$3.35\cdot10^{-1}$
60°-70°	$3.97\cdot10^{-1}$	$3.50\cdot10^{-1}$	$3.44\cdot10^{-1}$	$3.39\cdot10^{-1}$	$3.34\cdot10^{-1}$	$3.28\cdot10^{-1}$
70°-80°	$3.71\cdot10^{-1}$	$3.34\cdot10^{-1}$	$3.42\cdot10^{-1}$	$3.50\cdot10^{-1}$	$3.58\cdot10^{-1}$	$3.67\cdot10^{-1}$
80°-90°	$3.70\cdot10^{-1}$	$3.60\cdot10^{-1}$	$3.92\cdot10^{-1}$	$4.28\cdot10^{-1}$	$4.66\cdot10^{-1}$	$5.08\cdot10^{-1}$
90°-100°	$3.87\cdot10^{-1}$	$4.16\cdot10^{-1}$	$4.83\cdot10^{-1}$	$5.60\cdot10^{-1}$	$6.50\cdot10^{-1}$	$7.54\cdot10^{-1}$
100°-110°	$3.92\cdot10^{-1}$	$5.16\cdot10^{-1}$	$6.11\cdot10^{-1}$	$7.23\cdot10^{-1}$	$8.55\cdot10^{-1}$	1.01
110°-120°	$4.00\cdot10^{-1}$	$5.74\cdot10^{-1}$	$7.02\cdot10^{-1}$	$8.58\cdot10^{-1}$	1.05	1.28
120°-130°	$4.27\cdot10^{-1}$	$6.12\cdot10^{-1}$	$7.41\cdot10^{-1}$	$8.96\cdot10^{-1}$	1.08	1.31
130°-140°	$4.52\cdot10^{-1}$	$6.52\cdot10^{-1}$	$7.83\cdot10^{-1}$	$9.39\cdot10^{-1}$	1.13	1.35
140°-150°	$4.52\cdot10^{-1}$	$6.69\cdot10^{-1}$	$7.52\cdot10^{-1}$	$8.47\cdot10^{-1}$	$9.53\cdot10^{-1}$	1.07
150°-160°	$4.42\cdot10^{-1}$	$6.09\cdot10^{-1}$	$6.63\cdot10^{-1}$	$7.21\cdot10^{-1}$	$7.85\cdot10^{-1}$	$8.55\cdot10^{-1}$
160°-170°	$4.19\cdot10^{-1}$	$5.88\cdot10^{-1}$	$5.54\cdot10^{-1}$	$5.22\cdot10^{-1}$	$4.92\cdot10^{-1}$	$4.63\cdot10^{-1}$
170°-180°	$4.23\cdot10^{-1}$	$5.80\cdot10^{-1}$	$5.94\cdot10^{-1}$	$6.09\cdot10^{-1}$	$6.24\cdot10^{-1}$	$6.39\cdot10^{-1}$

Table 2.13: ξ ratios for the helium 250 MeV/u beam for the ICRU tissue target.

Angular Bin	**1 m**	**2 m**	**3 m**	**4 m**	**5 m**	**6 m**
0°-10°	$1.05\cdot10^{-1}$	$9.20\cdot10^{-2}$	$8.22\cdot10^{-2}$	$7.35\cdot10^{-2}$	$6.56\cdot10^{-2}$	$5.86\cdot10^{-2}$
10°-20°	$1.89\cdot10^{-1}$	$1.52\cdot10^{-1}$	$1.32\cdot10^{-1}$	$1.15\cdot10^{-1}$	$9.95\cdot10^{-2}$	$8.63\cdot10^{-2}$
20°-30°	$2.08\cdot10^{-1}$	$1.56\cdot10^{-1}$	$1.35\cdot10^{-1}$	$1.18\cdot10^{-1}$	$1.02\cdot10^{-1}$	$8.85\cdot10^{-2}$
30°-40°	$2.08\cdot10^{-1}$	$1.53\cdot10^{-1}$	$1.30\cdot10^{-1}$	$1.11\cdot10^{-1}$	$9.43\cdot10^{-2}$	$8.03\cdot10^{-2}$
40°-50°	$2.14\cdot10^{-1}$	$1.49\cdot10^{-1}$	$1.25\cdot10^{-1}$	$1.05\cdot10^{-1}$	$8.82\cdot10^{-2}$	$7.42\cdot10^{-2}$
50°-60°	$2.09\cdot10^{-1}$	$1.44\cdot10^{-1}$	$1.19\cdot10^{-1}$	$9.89\cdot10^{-2}$	$8.20\cdot10^{-2}$	$6.80\cdot10^{-2}$
60°-70°	$2.10\cdot10^{-1}$	$1.39\cdot10^{-1}$	$1.15\cdot10^{-1}$	$9.55\cdot10^{-2}$	$7.92\cdot10^{-2}$	$6.57\cdot10^{-2}$
70°-80°	$2.16\cdot10^{-1}$	$1.36\cdot10^{-1}$	$1.16\cdot10^{-1}$	$9.79\cdot10^{-2}$	$8.29\cdot10^{-2}$	$7.02\cdot10^{-2}$
80°-90°	$2.17\cdot10^{-1}$	$1.47\cdot10^{-1}$	$1.23\cdot10^{-1}$	$1.03\cdot10^{-1}$	$8.67\cdot10^{-2}$	$7.27\cdot10^{-2}$
90°-100°	$2.20\cdot10^{-1}$	$1.62\cdot10^{-1}$	$1.35\cdot10^{-1}$	$1.13\cdot10^{-1}$	$9.36\cdot10^{-2}$	$7.79\cdot10^{-2}$
100°-110°	$2.26\cdot10^{-1}$	$1.63\cdot10^{-1}$	$1.46\cdot10^{-1}$	$1.30\cdot10^{-1}$	$1.16\cdot10^{-1}$	$1.03\cdot10^{-1}$
110°-120°	$2.39\cdot10^{-1}$	$1.80\cdot10^{-1}$	$1.51\cdot10^{-1}$	$1.27\cdot10^{-1}$	$1.07\cdot10^{-1}$	$8.98\cdot10^{-2}$
120°-130°	$2.32\cdot10^{-1}$	$1.78\cdot10^{-1}$	$1.57\cdot10^{-1}$	$1.38\cdot10^{-1}$	$1.22\cdot10^{-1}$	$1.07\cdot10^{-1}$
130°-140°	$2.39\cdot10^{-1}$	$1.70\cdot10^{-1}$	$1.45\cdot10^{-1}$	$1.23\cdot10^{-1}$	$1.05\cdot10^{-1}$	$8.99\cdot10^{-2}$
140°-150°	$2.23\cdot10^{-1}$	$1.82\cdot10^{-1}$	$1.19\cdot10^{-1}$	$7.79\cdot10^{-2}$	$5.10\cdot10^{-2}$	$3.34\cdot10^{-2}$
150°-160°	$2.28\cdot10^{-1}$	$2.16\cdot10^{-1}$	$1.40\cdot10^{-1}$	$9.12\cdot10^{-2}$	$5.92\cdot10^{-2}$	$3.84\cdot10^{-2}$
160°-170°	$2.13\cdot10^{-1}$	$1.66\cdot10^{-1}$	$1.02\cdot10^{-1}$	$6.28\cdot10^{-2}$	$3.86\cdot10^{-2}$	$2.37\cdot10^{-2}$
170°-180°	$2.31\cdot10^{-1}$	$1.70\cdot10^{-1}$	$1.05\cdot10^{-1}$	$6.52\cdot10^{-2}$	$4.05\cdot10^{-2}$	$2.51\cdot10^{-2}$

Table 2.14: ξ ratios for the lithium 306 MeV/u beam for the ICRU tissue target.

Angular Bin	**1 m**	**2 m**	**3 m**	**4 m**	**5 m**	**6 m**
0°-10°	$4.98\cdot10^{-1}$	$4.98\cdot10^{-1}$	$4.83\cdot10^{-1}$	$4.69\cdot10^{-1}$	$4.55\cdot10^{-1}$	$4.41\cdot10^{-1}$
10°-20°	$6.27\cdot10^{-1}$	$5.71\cdot10^{-1}$	$5.42\cdot10^{-1}$	$5.14\cdot10^{-1}$	$4.88\cdot10^{-1}$	$4.63\cdot10^{-1}$
20°-30°	$6.25\cdot10^{-1}$	$5.51\cdot10^{-1}$	$5.19\cdot10^{-1}$	$4.89\cdot10^{-1}$	$4.61\cdot10^{-1}$	$4.34\cdot10^{-1}$
30°-40°	$6.12\cdot10^{-1}$	$5.34\cdot10^{-1}$	$4.98\cdot10^{-1}$	$4.64\cdot10^{-1}$	$4.32\cdot10^{-1}$	$4.03\cdot10^{-1}$
40°-50°	$6.25\cdot10^{-1}$	$5.39\cdot10^{-1}$	$5.00\cdot10^{-1}$	$4.63\cdot10^{-1}$	$4.29\cdot10^{-1}$	$3.97\cdot10^{-1}$
50°-60°	$6.33\cdot10^{-1}$	$5.45\cdot10^{-1}$	$5.04\cdot10^{-1}$	$4.66\cdot10^{-1}$	$4.30\cdot10^{-1}$	$3.98\cdot10^{-1}$
60°-70°	$6.46\cdot10^{-1}$	$5.48\cdot10^{-1}$	$5.05\cdot10^{-1}$	$4.64\cdot10^{-1}$	$4.27\cdot10^{-1}$	$3.93\cdot10^{-1}$
70°-80°	$6.53\cdot10^{-1}$	$5.49\cdot10^{-1}$	$5.08\cdot10^{-1}$	$4.70\cdot10^{-1}$	$4.35\cdot10^{-1}$	$4.03\cdot10^{-1}$
80°-90°	$6.52\cdot10^{-1}$	$5.62\cdot10^{-1}$	$5.14\cdot10^{-1}$	$4.71\cdot10^{-1}$	$4.31\cdot10^{-1}$	$3.94\cdot10^{-1}$
90°-100°	$6.54\cdot10^{-1}$	$5.63\cdot10^{-1}$	$5.16\cdot10^{-1}$	$4.73\cdot10^{-1}$	$4.33\cdot10^{-1}$	$3.97\cdot10^{-1}$
100°-110°	$6.59\cdot10^{-1}$	$5.61\cdot10^{-1}$	$5.24\cdot10^{-1}$	$4.89\cdot10^{-1}$	$4.56\cdot10^{-1}$	$4.26\cdot10^{-1}$
110°-120°	$6.52\cdot10^{-1}$	$5.53\cdot10^{-1}$	$5.26\cdot10^{-1}$	$5.01\cdot10^{-1}$	$4.77\cdot10^{-1}$	$4.54\cdot10^{-1}$
120°-130°	$6.30\cdot10^{-1}$	$5.46\cdot10^{-1}$	$5.09\cdot10^{-1}$	$4.75\cdot10^{-1}$	$4.44\cdot10^{-1}$	$4.14\cdot10^{-1}$
130°-140°	$6.52\cdot10^{-1}$	$5.47\cdot10^{-1}$	$5.30\cdot10^{-1}$	$5.14\cdot10^{-1}$	$4.98\cdot10^{-1}$	$4.83\cdot10^{-1}$
140°-150°	$6.04\cdot10^{-1}$	$5.50\cdot10^{-1}$	$5.48\cdot10^{-1}$	$5.45\cdot10^{-1}$	$5.43\cdot10^{-1}$	$5.41\cdot10^{-1}$
150°-160°	$6.21\cdot10^{-1}$	$6.41\cdot10^{-1}$	$5.77\cdot10^{-1}$	$5.19\cdot10^{-1}$	$4.67\cdot10^{-1}$	$4.20\cdot10^{-1}$
160°-170°	$6.15\cdot10^{-1}$	$5.30\cdot10^{-1}$	$5.11\cdot10^{-1}$	$4.92\cdot10^{-1}$	$4.74\cdot10^{-1}$	$4.56\cdot10^{-1}$
170°-180°	$6.17\cdot10^{-1}$	$5.50\cdot10^{-1}$	$5.22\cdot10^{-1}$	$4.96\cdot10^{-1}$	$4.71\cdot10^{-1}$	$4.47\cdot10^{-1}$

Table 2.15: ξ ratios for the oxygen 400 MeV/u beam for the ICRU tissue target.

Angular Bin	**1 m**	**2 m**	**3 m**	**4 m**	**5 m**	**6 m**
0°-10°	1.19	1.16	1.16	1.16	1.16	1.16
10°-20°	1.10	1.08	1.08	1.09	1.10	1.10
20°-30°	1.04	1.05	1.06	1.07	1.07	1.08
30°-40°	1.01	1.02	1.03	1.03	1.04	1.05
40°-50°	$9.79\cdot10^{-1}$	$9.90\cdot10^{-1}$	$9.97\cdot10^{-1}$	1.00	1.01	1.02
50°-60°	$9.53\cdot10^{-1}$	$9.60\cdot10^{-1}$	$9.64\cdot10^{-1}$	$9.69\cdot10^{-1}$	$9.74\cdot10^{-1}$	$9.79\cdot10^{-1}$
60°-70°	$9.36\cdot10^{-1}$	$9.41\cdot10^{-1}$	$9.47\cdot10^{-1}$	$9.52\cdot10^{-1}$	$9.58\cdot10^{-1}$	$9.64\cdot10^{-1}$
70°-80°	$9.24\cdot10^{-1}$	$9.25\cdot10^{-1}$	$9.31\cdot10^{-1}$	$9.37\cdot10^{-1}$	$9.43\cdot10^{-1}$	$9.49\cdot10^{-1}$
80°-90°	$9.21\cdot10^{-1}$	$9.36\cdot10^{-1}$	$9.53\cdot10^{-1}$	$9.71\cdot10^{-1}$	$9.88\cdot10^{-1}$	1.01
90°-100°	$9.14\cdot10^{-1}$	$9.26\cdot10^{-1}$	$9.43\cdot10^{-1}$	$9.60\cdot10^{-1}$	$9.78\cdot10^{-1}$	$9.96\cdot10^{-1}$
100°-110°	$9.34\cdot10^{-1}$	$9.46\cdot10^{-1}$	$9.64\cdot10^{-1}$	$9.84\cdot10^{-1}$	1.00	1.02
110°-120°	$9.26\cdot10^{-1}$	$9.39\cdot10^{-1}$	$9.62\cdot10^{-1}$	$9.86\cdot10^{-1}$	1.01	1.04
120°-130°	$9.47\cdot10^{-1}$	$9.35\cdot10^{-1}$	$9.53\cdot10^{-1}$	$9.72\cdot10^{-1}$	$9.91\cdot10^{-1}$	1.01
130°-140°	$9.53\cdot10^{-1}$	$9.58\cdot10^{-1}$	$9.65\cdot10^{-1}$	$9.72\cdot10^{-1}$	$9.80\cdot10^{-1}$	$9.87\cdot10^{-1}$
140°-150°	$9.26\cdot10^{-1}$	$9.26\cdot10^{-1}$	$9.67\cdot10^{-1}$	1.01	1.05	1.10
150°-160°	$9.29\cdot10^{-1}$	$9.94\cdot10^{-1}$	1.03	1.06	1.10	1.14
160°-170°	$9.69\cdot10^{-1}$	$9.12\cdot10^{-1}$	$9.19\cdot10^{-1}$	$9.25\cdot10^{-1}$	$9.31\cdot10^{-1}$	$9.37\cdot10^{-1}$
170°-180°	$9.46\cdot10^{-1}$	$9.24\cdot10^{-1}$	1.00	1.08	1.17	1.27

Table 2.16: ξ ratios for the iron 306 MeV/u beam for the ICRU tissue target.

Angular Bin	**1 m**	**2 m**	**3 m**	**4 m**	**5 m**	**6 m**
0°-10°	1.38	1.32	1.26	1.20	1.15	1.10
10°-20°	$8.66\cdot10^{-1}$	$7.83\cdot10^{-1}$	$7.36\cdot10^{-1}$	$6.91\cdot10^{-1}$	$6.50\cdot10^{-1}$	$6.10\cdot10^{-1}$
20°-30°	$5.78\cdot10^{-1}$	$5.22\cdot10^{-1}$	$4.97\cdot10^{-1}$	$4.74\cdot10^{-1}$	$4.52\cdot10^{-1}$	$4.30\cdot10^{-1}$
30°-40°	$4.70\cdot10^{-1}$	$4.25\cdot10^{-1}$	$4.02\cdot10^{-1}$	$3.80\cdot10^{-1}$	$3.60\cdot10^{-1}$	$3.40\cdot10^{-1}$
40°-50°	$4.06\cdot10^{-1}$	$3.62\cdot10^{-1}$	$3.42\cdot10^{-1}$	$3.23\cdot10^{-1}$	$3.06\cdot10^{-1}$	$2.89\cdot10^{-1}$
50°-60°	$3.56\cdot10^{-1}$	$3.14\cdot10^{-1}$	$2.99\cdot10^{-1}$	$2.84\cdot10^{-1}$	$2.70\cdot10^{-1}$	$2.57\cdot10^{-1}$
60°-70°	$3.22\cdot10^{-1}$	$2.84\cdot10^{-1}$	$2.76\cdot10^{-1}$	$2.69\cdot10^{-1}$	$2.61\cdot10^{-1}$	$2.54\cdot10^{-1}$
70°-80°	$3.07\cdot10^{-1}$	$2.81\cdot10^{-1}$	$2.84\cdot10^{-1}$	$2.88\cdot10^{-1}$	$2.92\cdot10^{-1}$	$2.96\cdot10^{-1}$
80°-90°	$3.09\cdot10^{-1}$	$3.01\cdot10^{-1}$	$3.20\cdot10^{-1}$	$3.41\cdot10^{-1}$	$3.62\cdot10^{-1}$	$3.85\cdot10^{-1}$
90°-100°	$3.28\cdot10^{-1}$	$3.41\cdot10^{-1}$	$3.74\cdot10^{-1}$	$4.09\cdot10^{-1}$	$4.48\cdot10^{-1}$	$4.91\cdot10^{-1}$
100°-110°	$3.42\cdot10^{-1}$	$3.64\cdot10^{-1}$	$3.97\cdot10^{-1}$	$4.32\cdot10^{-1}$	$4.71\cdot10^{-1}$	$5.13\cdot10^{-1}$
110°-120°	$3.67\cdot10^{-1}$	$3.90\cdot10^{-1}$	$4.13\cdot10^{-1}$	$4.38\cdot10^{-1}$	$4.64\cdot10^{-1}$	$4.92\cdot10^{-1}$
120°-130°	$3.88\cdot10^{-1}$	$3.82\cdot10^{-1}$	$4.17\cdot10^{-1}$	$4.55\cdot10^{-1}$	$4.97\cdot10^{-1}$	$5.43\cdot10^{-1}$
130°-140°	$4.07\cdot10^{-1}$	$3.82\cdot10^{-1}$	$3.97\cdot10^{-1}$	$4.12\cdot10^{-1}$	$4.28\cdot10^{-1}$	$4.44\cdot10^{-1}$
140°-150°	$4.04\cdot10^{-1}$	$3.50\cdot10^{-1}$	$3.91\cdot10^{-1}$	$4.36\cdot10^{-1}$	$4.87\cdot10^{-1}$	$5.43\cdot10^{-1}$
150°-160°	$3.97\cdot10^{-1}$	$3.59\cdot10^{-1}$	$3.95\cdot10^{-1}$	$4.34\cdot10^{-1}$	$4.77\cdot10^{-1}$	$5.25\cdot10^{-1}$
160°-170°	$4.02\cdot10^{-1}$	$3.62\cdot10^{-1}$	$3.27\cdot10^{-1}$	$2.95\cdot10^{-1}$	$2.66\cdot10^{-1}$	$2.41\cdot10^{-1}$
170°-180°	$4.36\cdot10^{-1}$	$4.30\cdot10^{-1}$	$4.54\cdot10^{-1}$	$4.79\cdot10^{-1}$	$5.06\cdot10^{-1}$	$5.34\cdot10^{-1}$

2.3.3 Discussion on Line of Sight Model

Numerical results obtained in this work can be used for the design of the shielding of a hadron therapy center can be assessed using the attenuation curves calculated in this thesis. Additionally, equivalent carbon ratio data can be utilized to estimate the maximum currents required for accelerating new ions in a facility that already accelerates carbon ions. For shielding evaluations, the following approach can be employed:

1. make reasonable assumptions on the beam losses (in particular, position, direction and intensity) of the accelerating machine;

2. evaluate the points of measure;

3. adopt the Equation 2.5 to calculate ambient dose equivalent values with the attenuation curve data.

To estimate the new ion currents, obviously, the beam loss points must be known a priori. After the evaluation of carbon ion doses, they can be multiplied by the correct carbon ratio taking into account the angular bin and the thickness of the shielding. After collecting ambient dose equivalent values for all dose points the maximum current can be evaluated.

2.4 Simulations of CNAO center

In recent years, the radiation protection group at CNAO has developed a computational model in order to simulate the behaviour of the center, using the Monte Carlo code FLUKA. The final implementation of the model is also a result of this thesis and includes the synchrotron, the BNCT (Boron Neutron Capture Therapy), and the proton therapy facility with a rotating gantry. This comprehensive model allows for the study and formulation of assumptions regarding various radiation protection aspects, including:

- Shielding;
- Air activation;
- Material activation;
- Water activation.

In this thesis, the simulations of ions listed in Table 2.1 have been conducted within the existing synchrotron to assess doses both inside and outside the center. The following paragraphs will detail the geometrical model employed in the Monte Carlo simulations and the beam loss model used for these simulations.

2.4.1 Geometry of the center

The geometry of the center has been designed in few years from the radiation protection group at CNAO with the Monte Carlo code FLUKA. It has dimensions around 80 m x 80 m x 100 m and includes the buildings of the surrounding area, and the three floors of CNAO building. In Figures 2.8 to 2.12 a set of geometry top views are shown. In particular:

- Figure 2.8 shows the CNAO center and its surroundings in a radius of around 400 m. All structures in the model are built with realistic dimensions and filled with air.
- Figure 2.9 shows the inside of CNAO center with the actual synchrotron, the future BNCT facility and the future, proton therapy synchrotron with a rotating gantry. All buildings are implemented adopting realistic measures and materials. It can be seen from Figure 2.9 that the -1 floor at CNAO is surrounded by ground (in green) that contributes to dose attenuation.
- Figure 2.10 shows the synchrotron design with magnets and the dimensions of the concrete shielding around the accelerating machine. The model includes: a stainless steel vacuum chamber, 20 elements from septums, dipoles to dumps made by copper, iron and stainless steel. A list of the elements implemented with dimensions is shown in Table 2.7.

Figure 2.7: Geometry elements implemented in CNAO synchrotron [8].

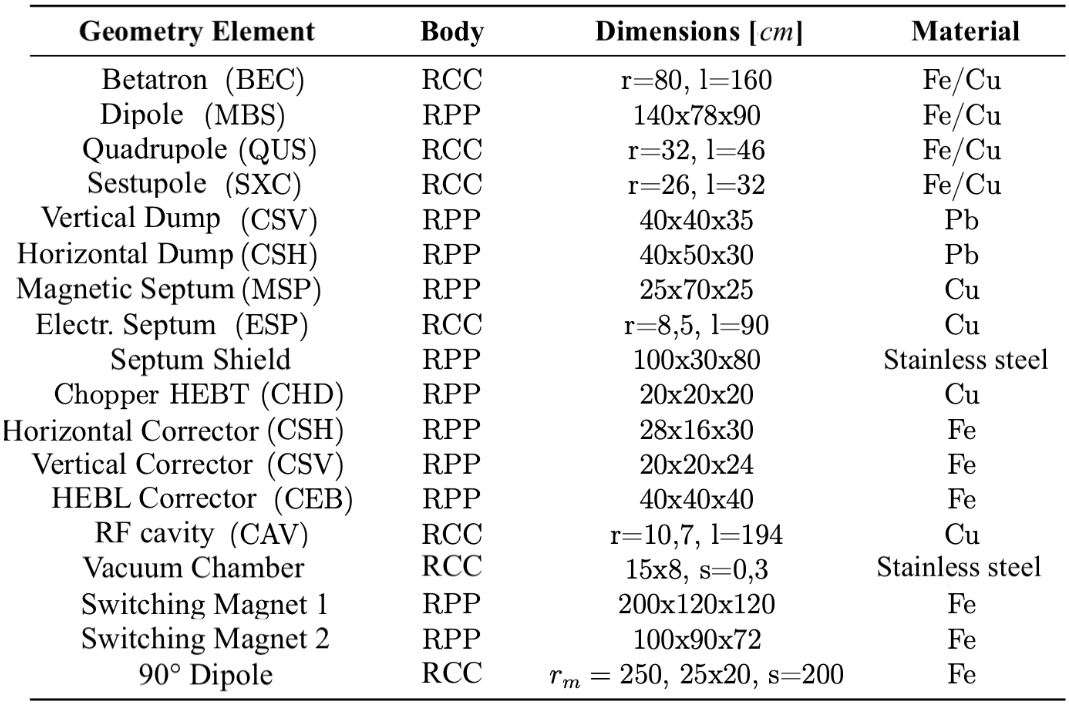

Geometry Element	**Body**	**Dimensions [cm]**	**Material**
Betatron (BEC)	RCC	r=80, l=160	Fe/Cu
Dipole (MBS)	RPP	140x78x90	Fe/Cu
Quadrupole (QUS)	RCC	r=32, l=46	Fe/Cu
Sestupole (SXC)	RCC	r=26, l=32	Fe/Cu
Vertical Dump (CSV)	RPP	40x40x35	Pb
Horizontal Dump (CSH)	RPP	40x50x30	Pb
Magnetic Septum (MSP)	RPP	25x70x25	Cu
Electr. Septum (ESP)	RCC	r=8,5, l=90	Cu
Septum Shield	RPP	100x30x80	Stainless steel
Chopper HEBT (CHD)	RPP	20x20x20	Cu
Horizontal Corrector (CSH)	RPP	28x16x30	Fe
Vertical Corrector (CSV)	RPP	20x20x24	Fe
HEBL Corrector (CEB)	RPP	40x40x40	Fe
RF cavity (CAV)	RCC	r=10,7, l=194	Cu
Vacuum Chamber	RCC	15x8, s=0,3	Stainless steel
Switching Magnet 1	RPP	200x120x120	Fe
Switching Magnet 2	RPP	100x90x72	Fe
90° Dipole	RCC	$r_m = 250$, 25x20, s=200	Fe

- Figure 2.11 shows the design and the shielding implemented for the treatment room 2 with the isocenter position (green cube).
- Figure 2.12 shows the design and the shielding implemented for the experimental room.

Geometry views

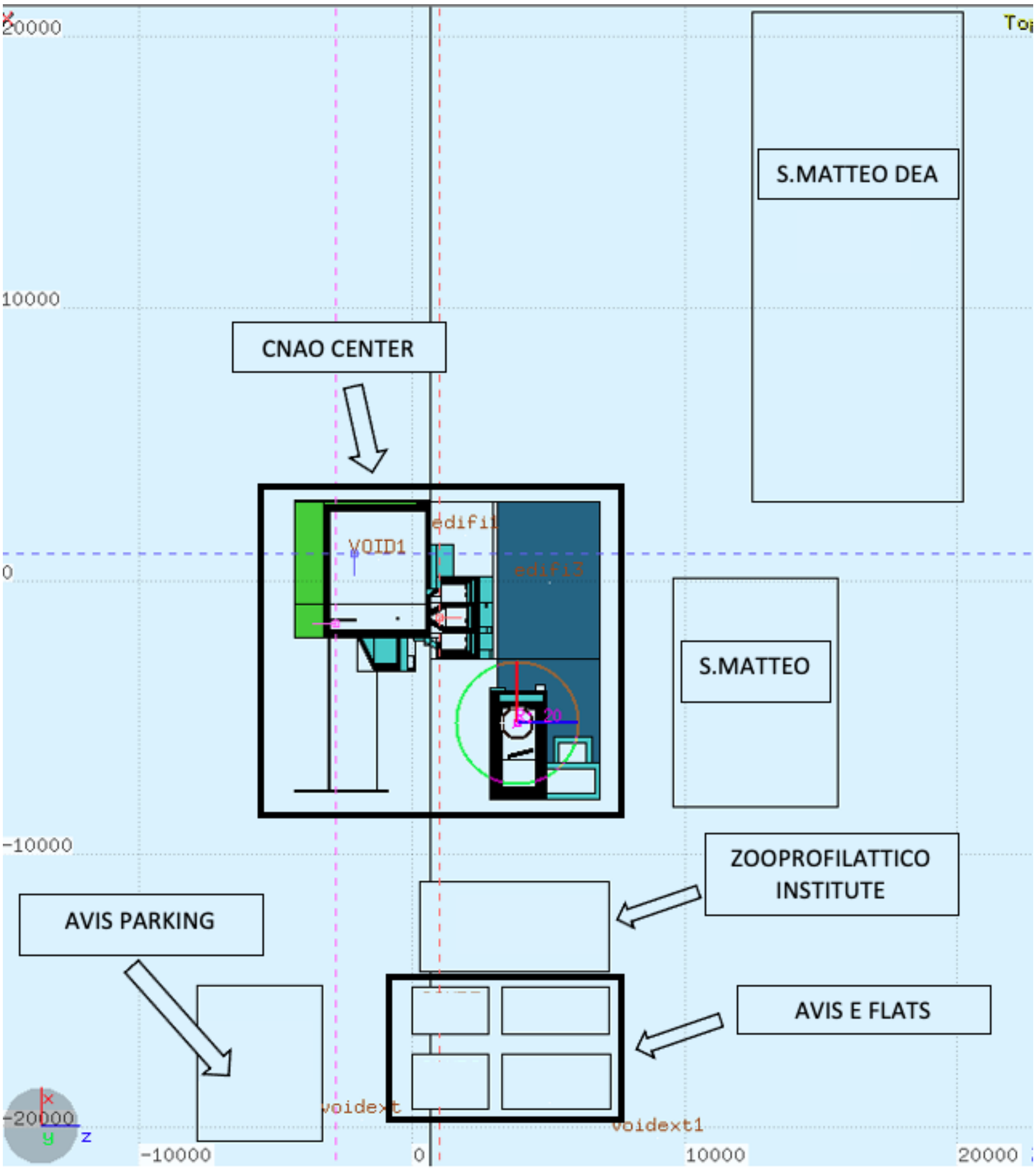

Figure 2.8: Geometry of CNAO implemented in FLUKA with surroundings buildings at street level, top view of floor 0.

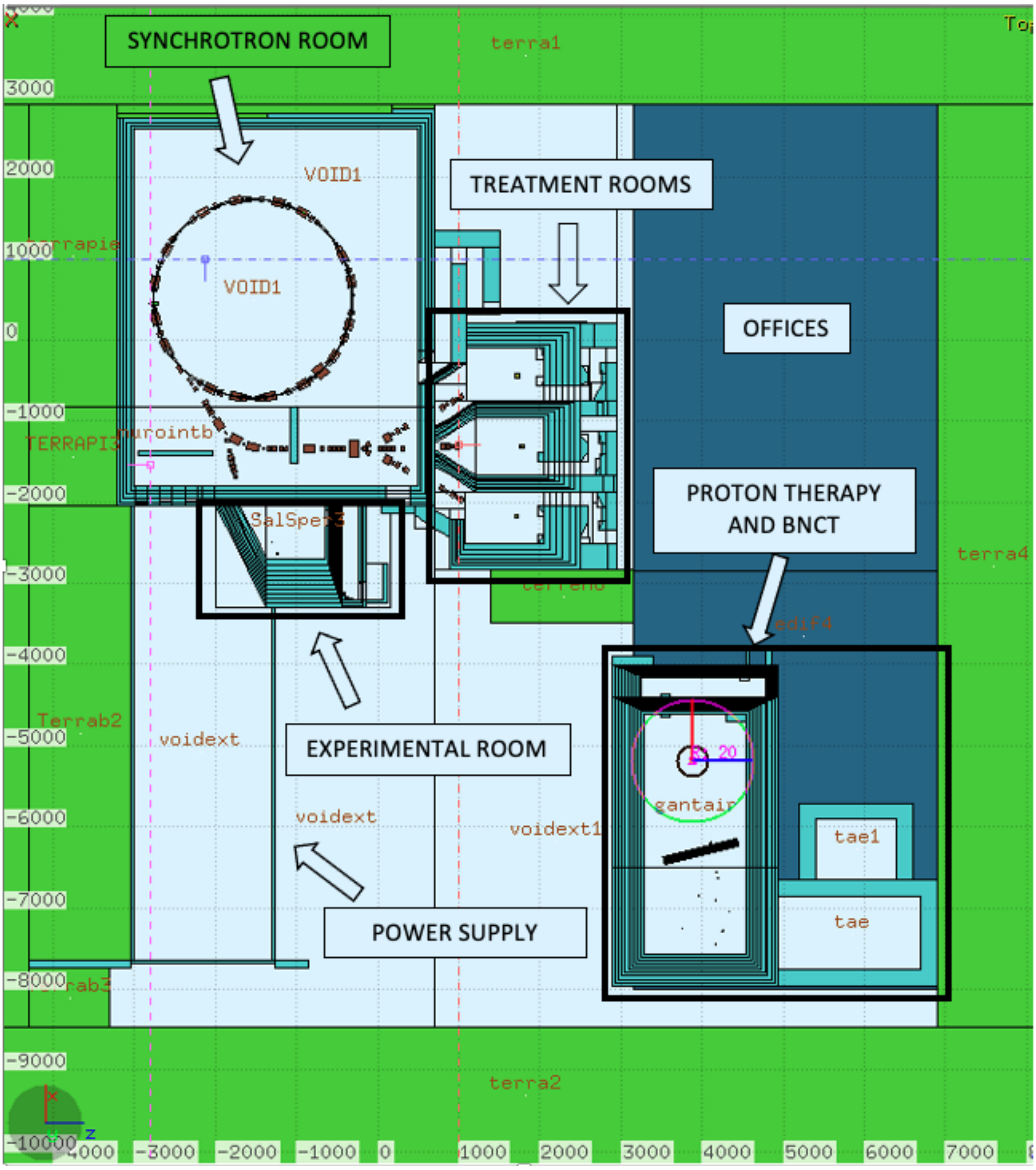

Figure 2.9: Geometry of CNAO center implemented in FLUKA at beam level, floor -1.

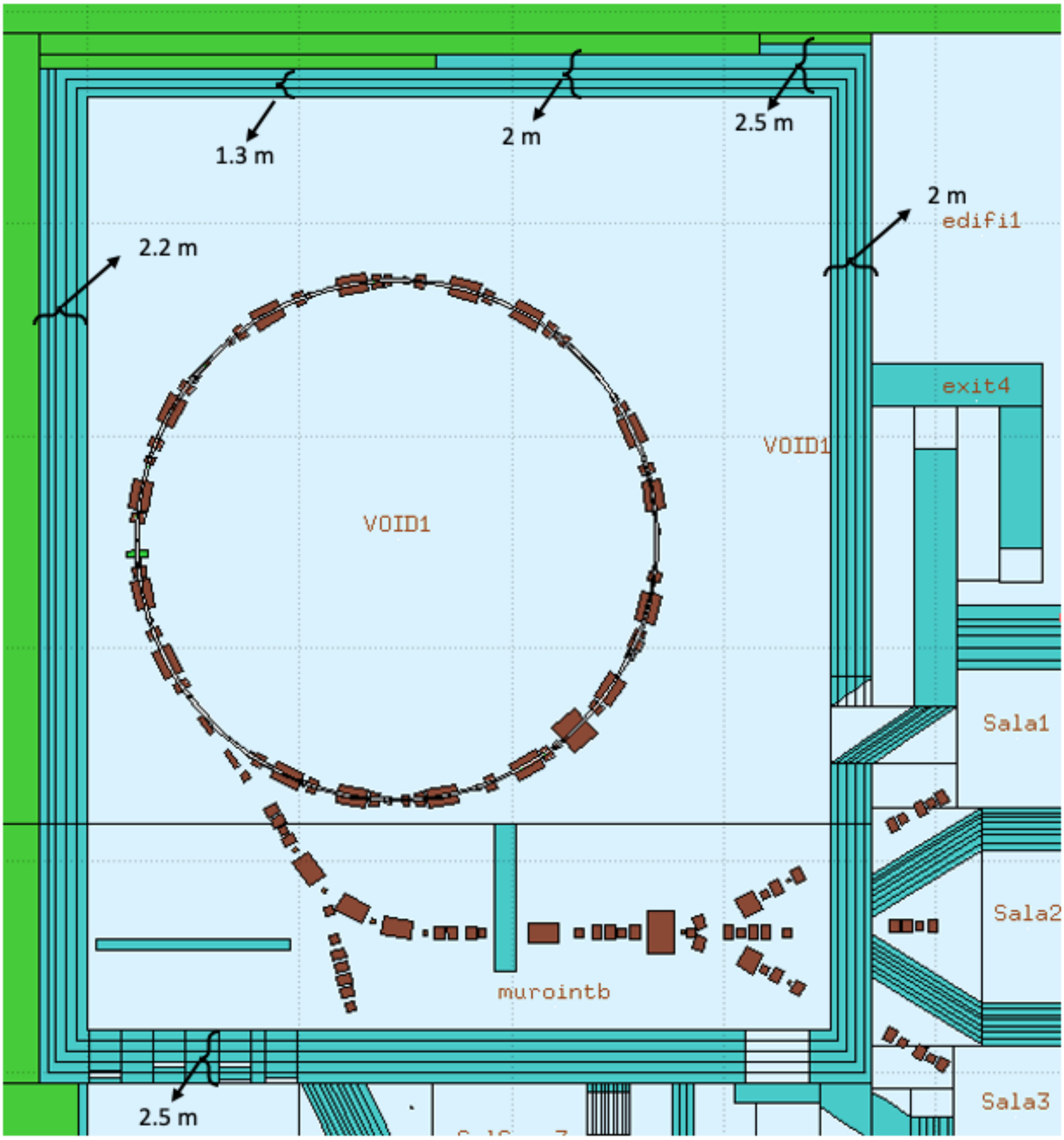

Figure 2.10: Shielding of synchrotron room, top view of floor -1.

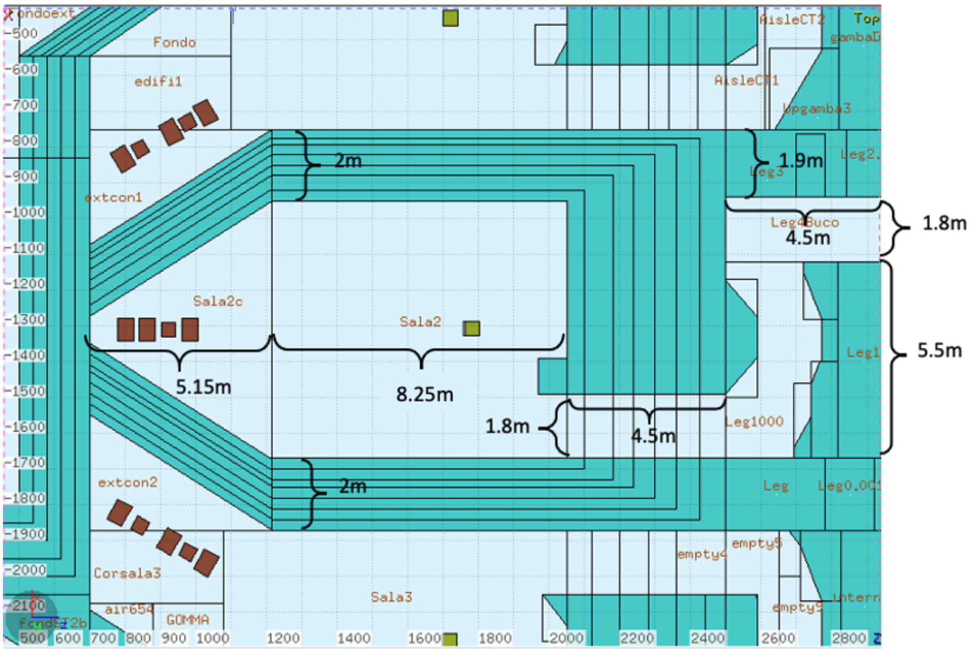

Figure 2.11: Shielding of treatment room 2, top view of floor -1.

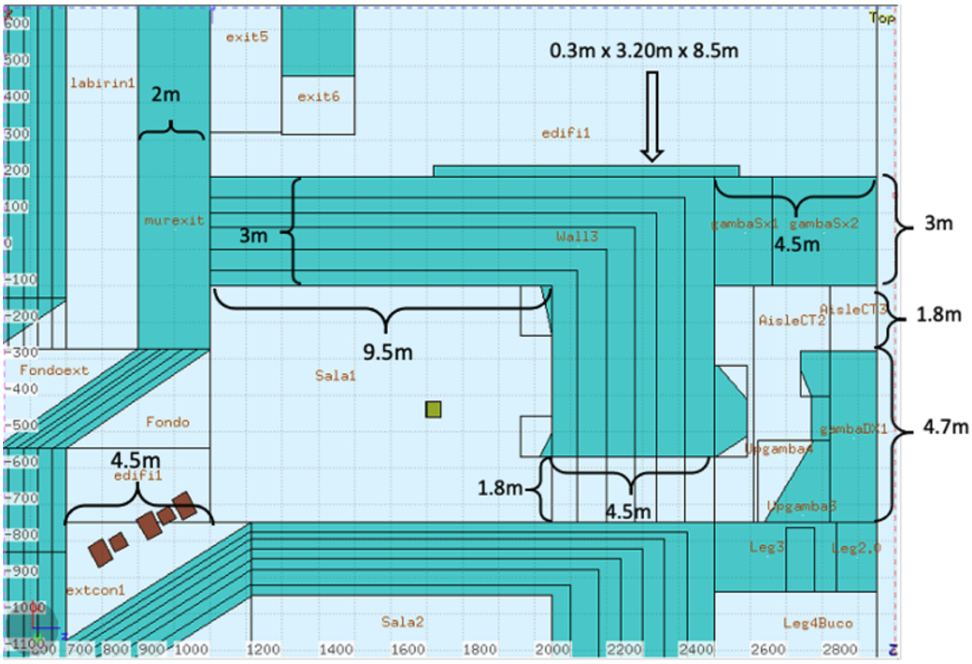

Figure 2.12: Shielding of experimental room, top view of floor -1.

2.4.2 Beam Loss Model

In order to run simulations for new ions it is necessary to build a model of the beam losses within the synchrotron. Beam losses can occur for two primary reasons:

1. Treatment or experimental losses: these occur when the beam is intentionally directed towards a patient or a target for treatment or experimentation.
2. Accidental losses: These are unintended losses and take place when the beam deviates from its ideal trajectory and strikes structural elements within the synchrotron, such as magnets, the vacuum chamber, or beam dumps.

Physically, these losses produce a secondary high energy secondary field with a spectrum that depends mainly on the energy and direction of the beam, the Z of the impinging ion and Z of the target and the thickness of the target (see Tables 2.3, 2.4 and Figure 2.3). To ensure the accurate assessment of doses both inside and outside the center, a beam loss model has been incorporated into the Monte Carlo code for the simulations. It's important to note that this model has been developed with a focus on radiation protection and, as such, is designed to be conservative in its approach. In the following list the main hypothesis adopted for the model are described:

- $\sim$50% of beam losses are due to treatments or experiments while the other 50% is due to accidental losses.
- 29 loss points have been identified and implemented in the simulations. Their positions are shown in Figure 2.13. An example of the loss percentages for each loss point is reported in Table 2.17.
- The percentages shown in Table 2.17 were evaluated with workloads reported in Table 2.18.
- The same beam loss distribution has been adopted for all beams. The aim is to evaluate the maximal current at which accelerate the new ions, at maximal energy, with the same current distribution of protons.

The distribution and percentages of beam losses have been described in accordance with recommendations of the experts of the radiation protection group, the research and development team at CNAO and machine physicists.

In the FLUKA software, users are typically limited to specifying a single starting point for the beam. To address this limitation, the beam loss model has been incorporated into the simulations using a user-written Fortran routine. The algorithm generates a random number between 0 and 1 and then assigning a beam loss location using the inverse cumulative method. The cumulative distribution is discrete, with the abscissa representing the beam loss point and the ordinate indicating the cumulative value of the normalized loss percentages (as seen in Tables 2.17 and 2.18). Figure 2.14 provides an example of this method, illustrating how a random number is extracted, a corresponding percentage is determined, and the algorithm assigns the beam loss point. For accurate simulation and proper transport, the code assigns three geometrical coordinates and three direction cosines to each loss point.

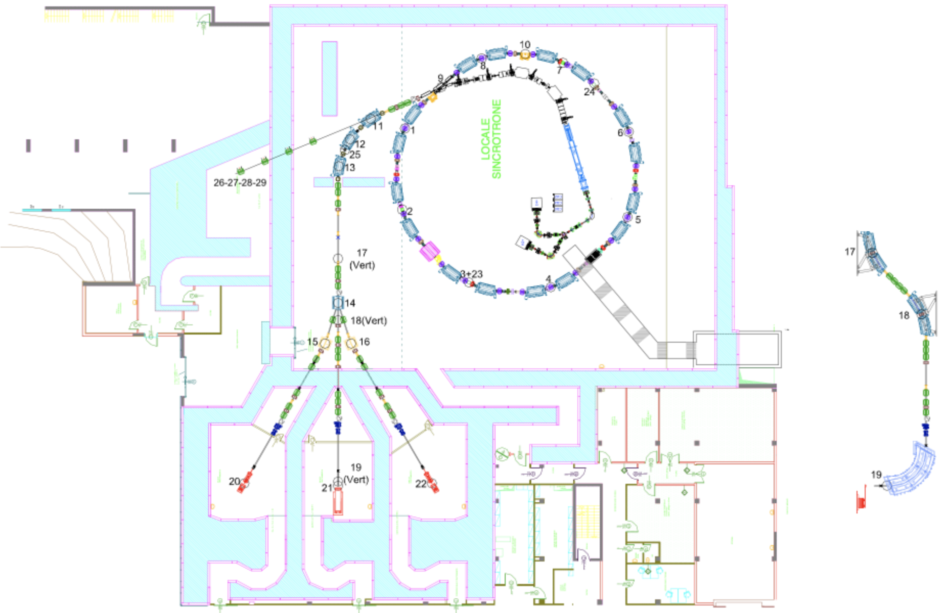

Figure 2.13: Beam loss map of the center for points from 1 to 29.

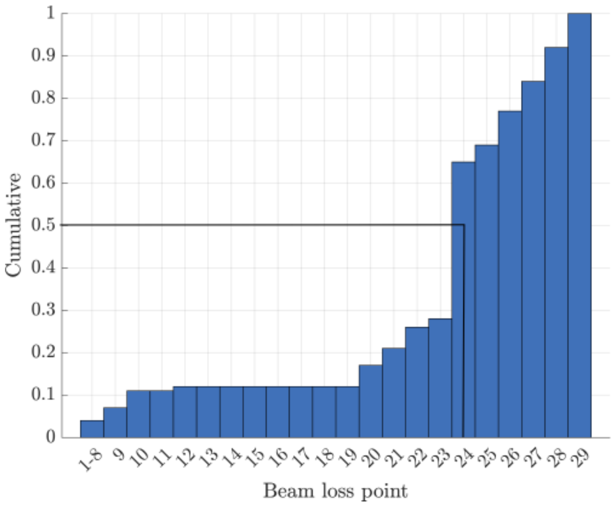

Figure 2.14: Cumulative discrete function for beam loss points.

Table 2.17: Description of beam loss points in Figure 2.13 for protons.

Loss point number	**Loss point element**	**Normalized Loss percentages**
1 to 8	Ring	3.70%
9	Magnetic septum	3.70%
10	Electrostatic septum	3.70%
11-12-13	Extraction dipoles	1.39%
14	Switching dipole	0.07%
15-16	Matching dipoles	0.06%
17-18-19	Vertical line dipole 1	0.04%
20-21-22	Isocenter TR rooms	14.16%
23	Vertical dump	2.22%
24	Horizontal dump	36.99%
25	Chopper dump	3.60%
26-27-28-29	Isocenters XPR room	31.2%

Table 2.18: Beam loss percentages hypothesis with therapy, experimental and total workloads for protons expressed in protons per year [p/year].

Loss point number	**Therapy workload [p/year]**	**Experimental workload [p/year]**	**Total workload [p/year]**	**Loss percentages per loss point**	**Normalized loss percentage**
1 to 8	$6.19{\cdot}10^{15}$	$6.34{\cdot}10^{15}$	$1.25{\cdot}10^{16}$	5%	3.70%
9	$6.19{\cdot}10^{15}$	$6.34{\cdot}10^{15}$	$1.25{\cdot}10^{16}$	5%	3.70%
10	$6.19{\cdot}10^{15}$	$6.34{\cdot}10^{15}$	$1.25{\cdot}10^{16}$	5%	3.70%
11	$5.15{\cdot}10^{15}$	$5.28{\cdot}10^{15}$	$1.04{\cdot}10^{16}$	0.63%	0.38%
12	$3.07{\cdot}10^{15}$	-	$3.07{\cdot}10^{15}$	0.63%	0.11%
13	$2.44{\cdot}10^{15}$	-	$2.44{\cdot}10^{15}$	0.63%	0.09%
14	$2.02{\cdot}10^{15}$	-	$2.02{\cdot}10^{15}$	0.63%	0.07%
15	$8.03{\cdot}10^{14}$	-	$8.03{\cdot}10^{14}$	0.63%	0.03%
16	$8.03{\cdot}10^{14}$	-	$8.03{\cdot}10^{14}$	0.63%	0.03%
17	$4.07{\cdot}10^{14}$	-	$4.07{\cdot}10^{14}$	0.63%	0.02%
18	$4.04{\cdot}10^{14}$	-	$4.04{\cdot}10^{14}$	0.63%	0.01%
19	$4.02{\cdot}10^{14}$	-	$4.02{\cdot}10^{14}$	0.63%	0.01%
20	$7.99{\cdot}10^{14}$	-	$7.99{\cdot}10^{14}$	100%	4.72%
21	$7.99{\cdot}10^{14}$	-	$7.99{\cdot}10^{14}$	100%	4.72%
22	$7.99{\cdot}10^{14}$	-	$7.99{\cdot}10^{14}$	100%	4.72%
23	$6.19{\cdot}10^{15}$	$6.34{\cdot}10^{15}$	$1.25{\cdot}10^{16}$	3%	2.22%
24	$6.19{\cdot}10^{15}$	$6.34{\cdot}10^{15}$	$1.25{\cdot}10^{16}$	50%	36.99%
25	$3.05{\cdot}10^{15}$	-	$3.05{\cdot}10^{15}$	20%	3.60%
26	$1.32{\cdot}10^{15}$	$1.32{\cdot}10^{15}$	$1.32{\cdot}10^{15}$	100%	7.80%
27	$1.32{\cdot}10^{15}$	$1.32{\cdot}10^{15}$	$1.32{\cdot}10^{15}$	100%	7.80%
28	$1.32{\cdot}10^{15}$	$1.32{\cdot}10^{15}$	$1.32{\cdot}10^{15}$	100%	7.80%
29	$1.32{\cdot}10^{15}$	$1.32{\cdot}10^{15}$	$1.32{\cdot}10^{15}$	100%	7.80%

2.4.3 Methodology

Monte Carlo simulations enable the user to determine ambient dose equivalent values within bins of a grid that is independent of the geometry, utilizing the `USRBIN` scoring card, as depicted in Figure 2.15. In this example, there are a total of 312,500 bins (NX x NY x NZ). To obtain the rate of ambient dose equivalent expressed in pSv/year, the user should multiply the output from the `USRBIN` card, which is expressed in pSv/primary, by the number of ions accelerated per year. The output from this card is a text file that contains a table with ten columns and a variable number of rows depending on the number of bins. The `USRBIN` cards have been used with two different modalities:

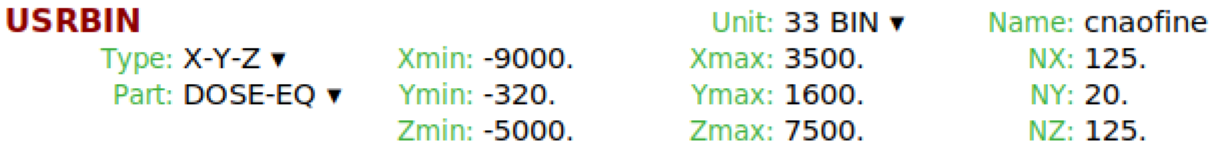

```
USRBIN                                          Unit: 33 BIN ▾      Name: cnaofine
          Type: X-Y-Z ▾       Xmin: -9000.      Xmax: 3500.           NX: 125.
          Part: DOSE-EQ ▾     Ymin: -320.       Ymax: 1600.           NY: 20.
                              Zmin: -5000.      Zmax: 7500.           NZ: 125.
```

Figure 2.15: Example of `USRBIN` card adopted in FLUKA simulations.

1. To compare ambient dose equivalent values in selected bins to calculate the maximum current for each ion beam.
2. To generate ambient dose equivalent rate maps.

In order to assess new ion doses around 390 dose bins have been taken into account. In particular, the points can be divided into:

- 13 external points: 5 points indicated in Figure 2.16 and 8 points indicated in Figure 2.8. In particular: Avis parking, Avis building, 3 flats, Zooprofilattico institute, S. Matteo and S. Matteo DEA.
- 230 internal points considered representative for ambient dosimetry including points inside and outside CNAO building in the CNAO center at floor -1, 0 and 1. These points include offices, areas outside the synchrotron, treatment and XPR room shieldings and points around the main building.
- 147 points in proton therapy and BNCT area at floor -1, 0 and 1 to evaluate the impact of synchrotron in the new buildings (view Figure 2.9).

The evaluation of currents are obtained by calculating the ratio between the dose of a new ion and the dose for carbon ion in a given point with raw data expressed in pSv/primary. In order to get ratios, it is necessary to run one simulation for each ion (^{4}He at 250 MeV/u, ^{7}Li at 306 MeV/u, ^{12}C at 400 MeV/u, ^{16}O at 400 MeV/u and ^{56}Fe at 306 MeV/u) and to handle 12 `USRBIN` text files for the extraction of dose points.

All data are processed with a MATLAB script that is able to extract a given dose point from the output of the `USRBIN` file. The input for the script consists of `USRBIN` files

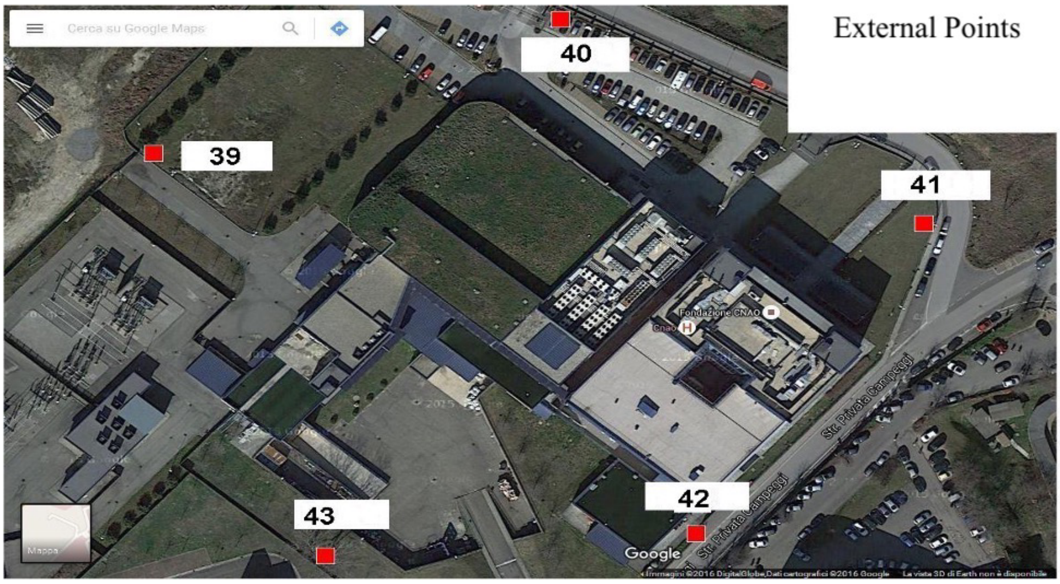

Figure 2.16: External point in which ambient dose equivalent has been evaluated.

containing the scoring data of interest, as well as the X, Y, and Z coordinates of scoring points within the geometry. These coordinates are manually inserted by the user into a text file. The output from the script provides a text file with the desired scoring data and the corresponding errors. The MATLAB script incorporates two functions:

- Function 1: This function is responsible for collecting the X, Y, Z coordinates of the scoring points, the number of bins, and the width of X, Y, Z bins. Additionally, it gathers matrices of scoring values and scoring errors from a `USRBIN` output file.
- Function 2: This function processes the X, Y, Z coordinates of the scoring points within the geometry, which are manually input by the user into a text file, to determine the corresponding X, Y, Z bin for each scoring point.

An example of `USRBIN` output file is shown in Figure 2.17. In particular, the file gives the X,Y,Z coordinates of the detector, the number of bins and their width as the user has set and a matrix containing the scoring data. In the example in Figure 2.17 the matrix counts 100 values divided into 5 X bins, 2 Y bins and 10 Z bins respectively 4, 10 and 2 *cm* wide. The format of the matrix gives information of how to read it: the matrix is divided into 10 Z bins (orange frame in the example), each Z bin is divide into 2 Y bins (blue frame in the example) and each Y bin contains 5 X bins. In the example, the value in the orange frame is found in the 3rd X bin, the 1st Y bin and the 3rd Z bin.

Once all the necessary data are collected and processed, it becomes feasible to compare and evaluate maximum values for the beam currents of new ions within the existing synchrotron shielding. Additionally, ambient dose equivalent dose maps can be generated using these reasonable beam currents.

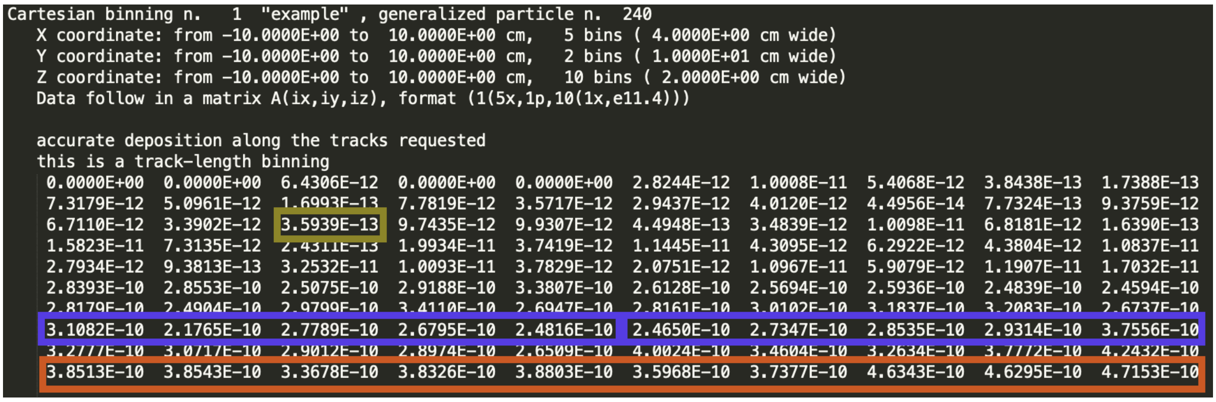

```
Cartesian binning n.   1  "example" , generalized particle n.  240
   X coordinate: from -10.0000E+00 to  10.0000E+00 cm,   5 bins ( 4.0000E+00 cm wide)
   Y coordinate: from -10.0000E+00 to  10.0000E+00 cm,   2 bins ( 1.0000E+01 cm wide)
   Z coordinate: from -10.0000E+00 to  10.0000E+00 cm,   10 bins ( 2.0000E+00 cm wide)
   Data follow in a matrix A(ix,iy,iz), format (1(5x,1p,10(1x,e11.4)))

   accurate deposition along the tracks requested
   this is a track-length binning
    0.0000E+00  0.0000E+00  6.4306E-12  0.0000E+00  0.0000E+00  2.8244E-12  1.0008E-11  5.4068E-12  3.8438E-13  1.7388E-13
    7.3179E-12  5.0961E-12  1.6993E-13  7.7819E-12  3.5717E-12  2.9437E-12  4.0120E-12  4.4956E-14  7.7324E-13  9.3759E-12
    6.7110E-12  3.3902E-12  3.5939E-13  9.7435E-12  9.9307E-12  4.4948E-13  3.4839E-12  1.0098E-11  6.8181E-12  1.6390E-13
    1.5823E-11  7.3135E-12  2.4311E-13  1.9934E-11  3.7419E-12  1.1445E-11  4.3095E-12  6.2922E-12  4.3804E-12  1.0837E-11
    2.7934E-12  9.3813E-13  3.2532E-11  1.0093E-11  3.7829E-12  2.0751E-12  1.0967E-11  5.9079E-12  1.1907E-11  1.7032E-11
    2.8393E-10  2.8553E-10  2.5075E-10  2.9188E-10  3.3807E-10  2.6128E-10  2.5694E-10  2.5936E-10  2.4839E-10  2.4594E-10
    2.8179E-10  2.4904E-10  2.9799E-10  3.4110E-10  2.6947E-10  2.8161E-10  3.0102E-10  3.1837E-10  3.2083E-10  2.6737E-10
    3.1082E-10  2.1765E-10  2.7789E-10  2.6795E-10  2.4816E-10  2.4650E-10  2.7347E-10  2.8535E-10  2.9314E-10  3.7556E-10
    3.2777E-10  3.0717E-10  2.9012E-10  2.8974E-10  2.6509E-10  4.0024E-10  3.4604E-10  3.2634E-10  3.7772E-10  4.2432E-10
    3.8513E-10  3.8543E-10  3.3678E-10  3.8326E-10  3.8803E-10  3.5968E-10  3.7377E-10  4.6343E-10  4.6295E-10  4.7153E-10
```

Figure 2.17: Example of `USRBIN` output file.

2.4.4 Results

The aim of the simulations is to assess ambient dose equivalent values inside (without taking into account synchrotron, treatment and XPR rooms) and outside CNAO center for ^{4}He at 250MeV/u, ^{7}Li at 306 MeV/u, ^{12}C at 400 MeV/u, ^{16}O at 400 MeV/u and ^{56}Fe at 306 MeV/u. As described in the last section, around 390 dose points have been evaluated both inside and outside the center. In order to evaluate the current at which accelerate the new ions, a current ratio has been introduced. The ratio has been calculated making the ratio between the dose value evaluated with carbon ions and with a selected ion. The worst case current ratio in Table 2.19 has been selected through the following process:

1. evaluate the ratio between the dose per primary of carbon ions and a selected ion;
2. multiplying the ratio for the maximum current allowed for carbon ions ($1.26{\cdot}10^{16}$ ions/year) to obtain μSv/year values for each beam;
3. select dose values higher than the radiological significance ($>$10 μSv/year) and with errors $<$10%.
4. calculate the worst case current ratio dividing the maximum dose by $1.26{\cdot}10^{16}$ ions/year.

These ratios multiplied by $1.26{\cdot}10^{16}$ ions/year indicate the maximum current at which each ion can be accelerated without overcoming carbon ion doses inside the center. In the last column of Table 2.19, expressed in ions/year, have been calculated, taking into account the maximum ratios and CNAO requirements for treatment and experimental activities for each ion.

As an example, in Figures 2.18 to 2.27 the ambient dose equivalent maps are shown with the ions/year reported in Table 2.20. Maps can be divided into groups:

- Figures 2.18 to 2.22: show the maps for the area surrounding CNAO with the external buildings (view Figure 2.8).

Table 2.19: Values of the current ratio between a selected ion beam and carbon ions to evaluate the maximum currents (Max Case) and the ratio that takes into account the requirements of CNAO center (Suggested Current Ratio).

Ion	**Beam Energy [MeV/u]**	**Max Case Current Ratio**	**Suggested Current Ratio**
^{4}He	250	2.75	2.5
^{7}Li	306	1.19	0.83
^{16}O	400	0.63	0.13
^{56}Fe	306	1.16	0.07

- Figures 2.23 to 2.27: show the maps for the CNAO center at beam level, floor -1 (view Figure 2.9).

Table 2.20: Values of ions/year adopted for the ambient dose equivalent maps.

Ion	**Beam Energy [MeV/u]**	**ions/year**
^{4}He	250	$3.15 \cdot 10^{16}$
^{7}Li	306	$1.05 \cdot 10^{16}$
^{12}C	400	$1.26 \cdot 10^{16}$
^{16}O	400	$1.68 \cdot 10^{15}$
^{56}Fe	306	$8.4 \cdot 10^{14}$

2.4.5 Ambient dose equivalent maps

Ambient dose equivalent surroundings, floor 0

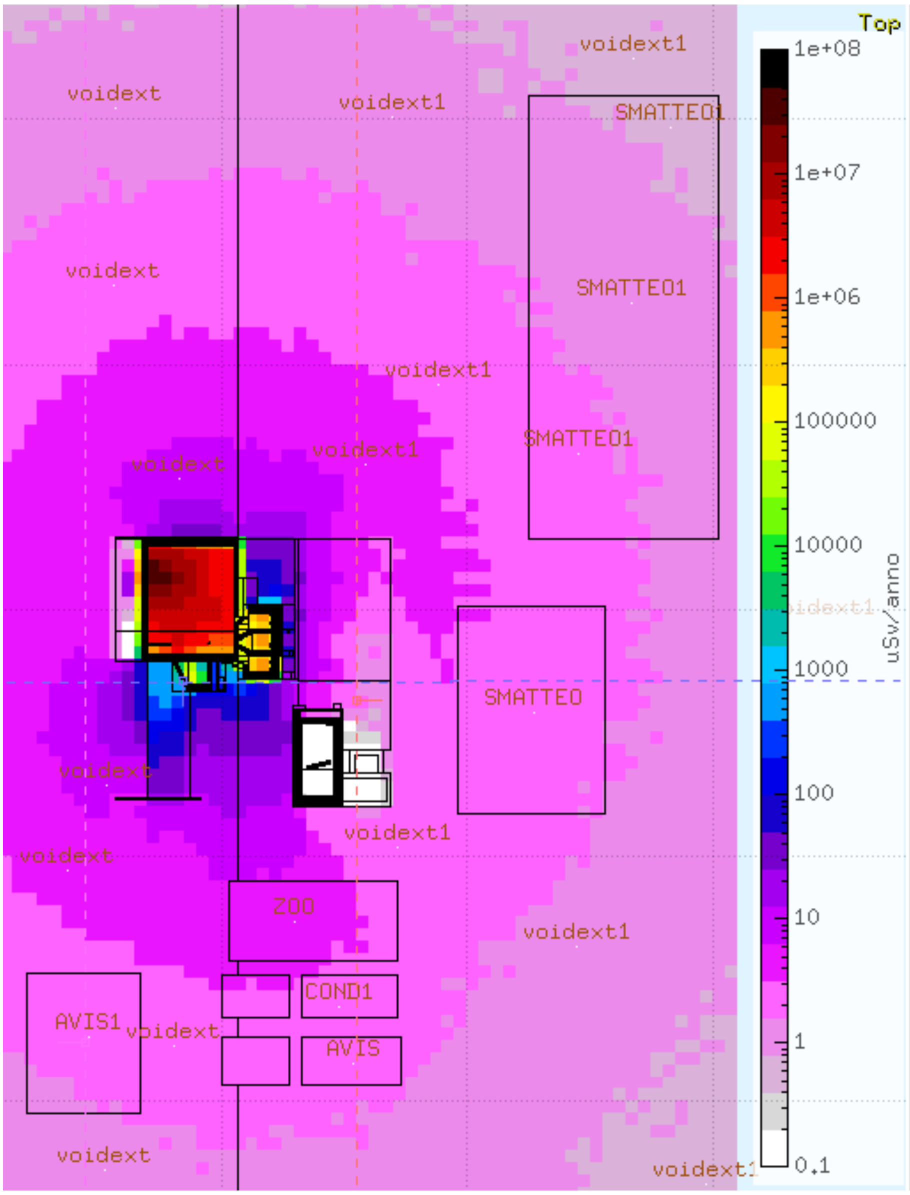

Figure 2.18: View of the surroundings of the center ambient dose equivalent map for 400 MeV/u carbon ion beam, floor 0, expressed in μ Sv/year.

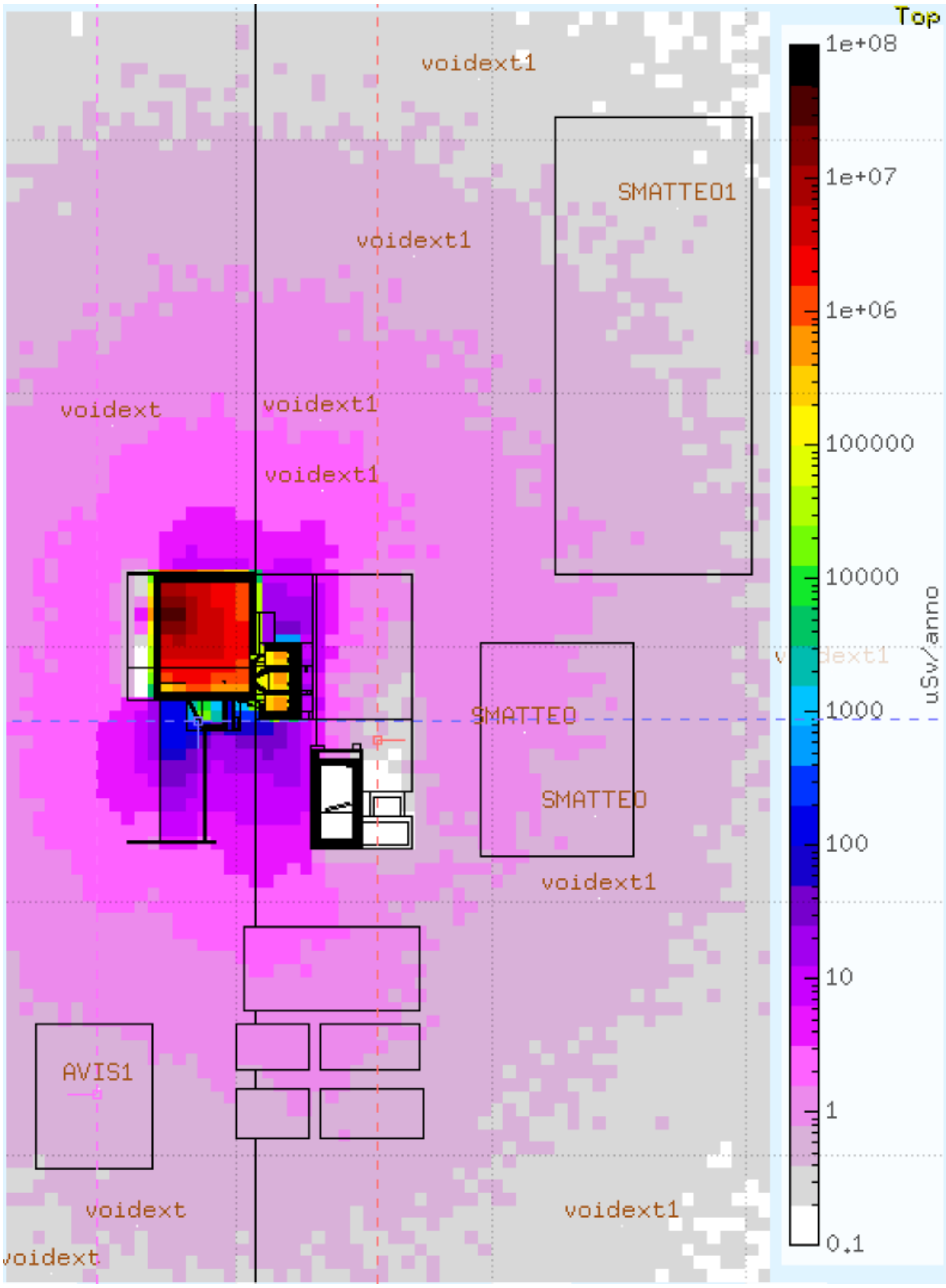

Figure 2.19: View of the surroundings of the center ambient dose equivalent map for 250 MeV/u helium beam, floor 0, expressed in μSv/year.

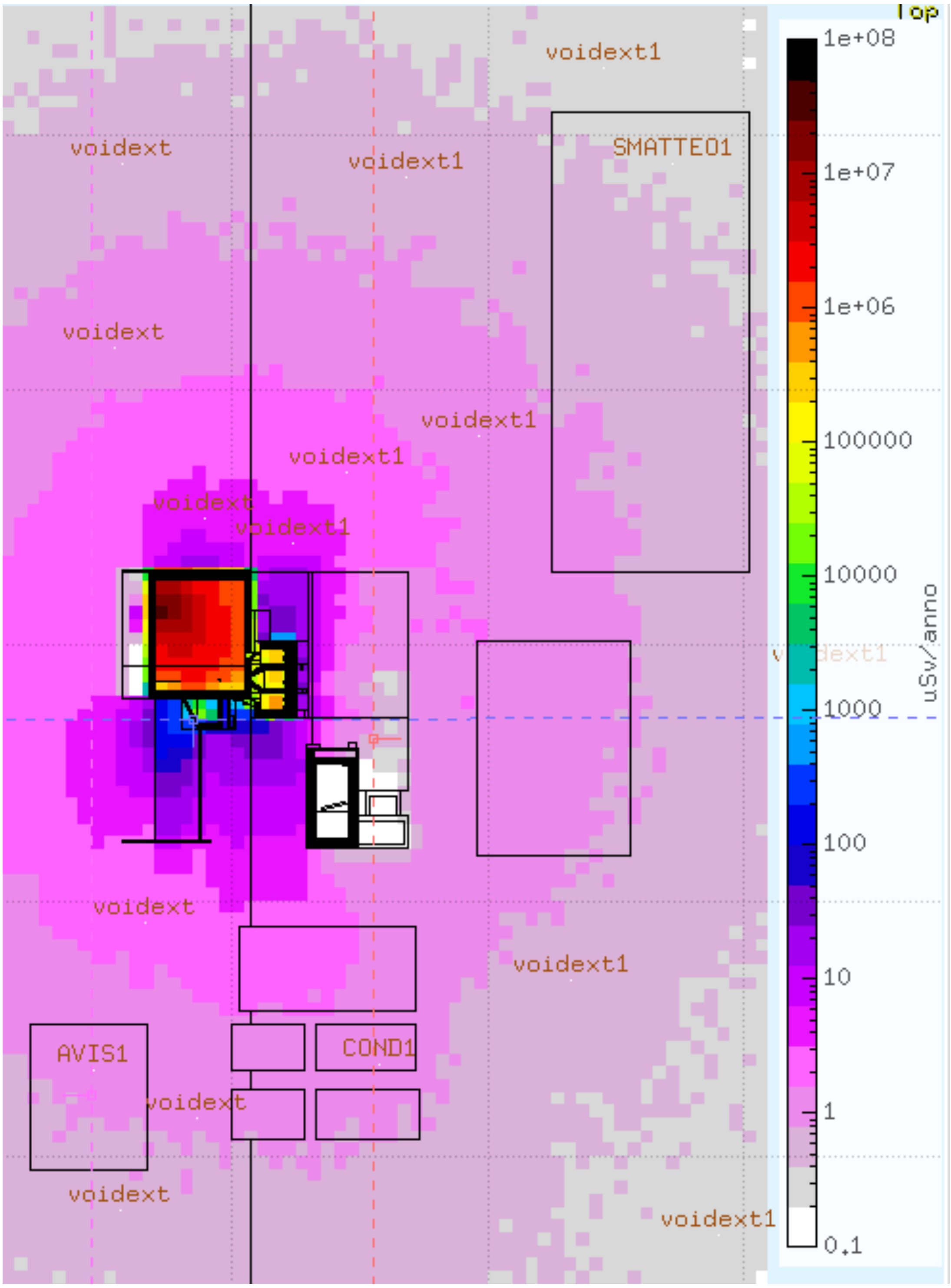

Figure 2.20: View of the surroundings of the center ambient dose equivalent map for 306 MeV/u lithium ion beam, floor 0, expressed in μSv/year.

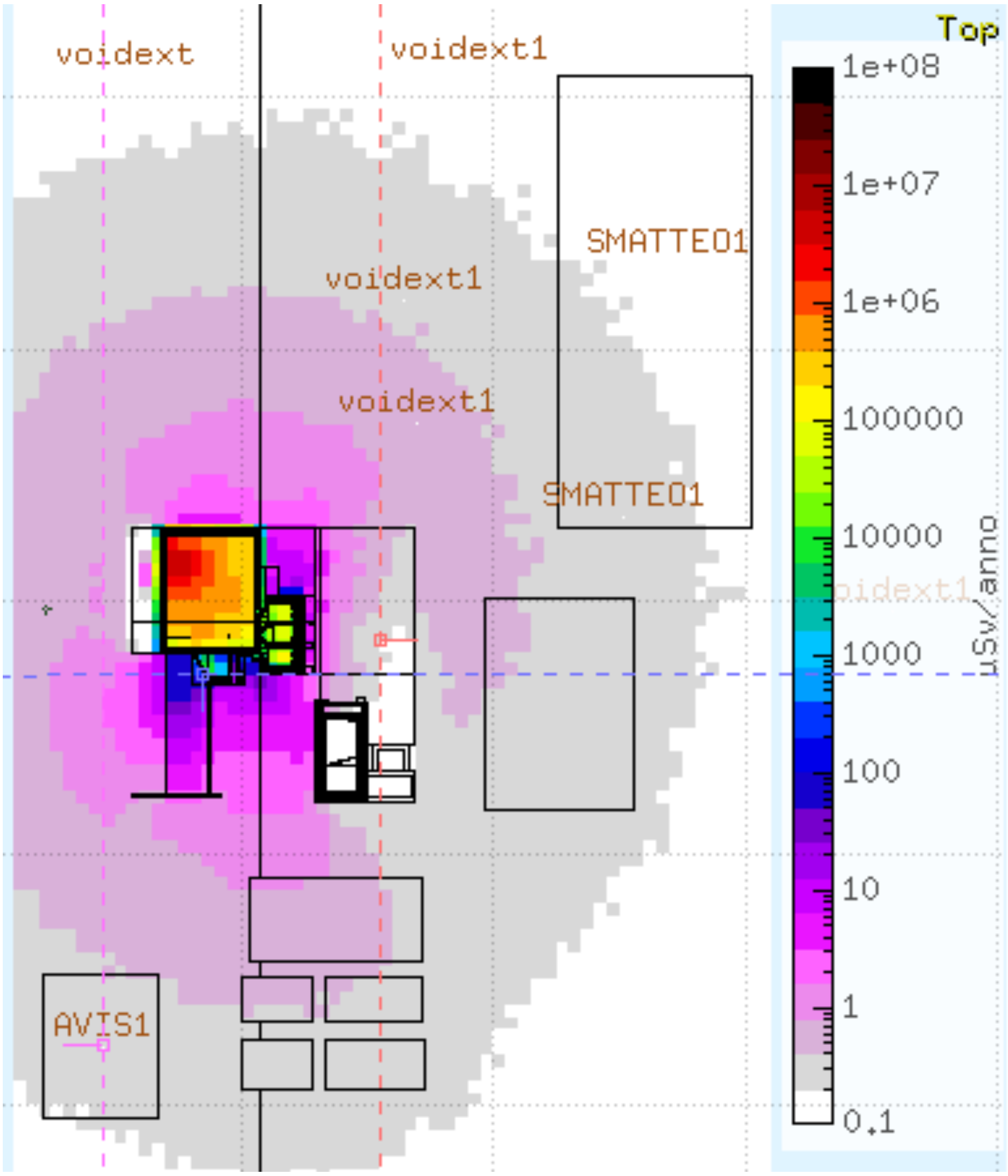

Figure 2.21: View of the surroundings of the center ambient dose equivalent map for 400 MeV/u oxygen ion beam, floor 0, expressed in μSv/year.

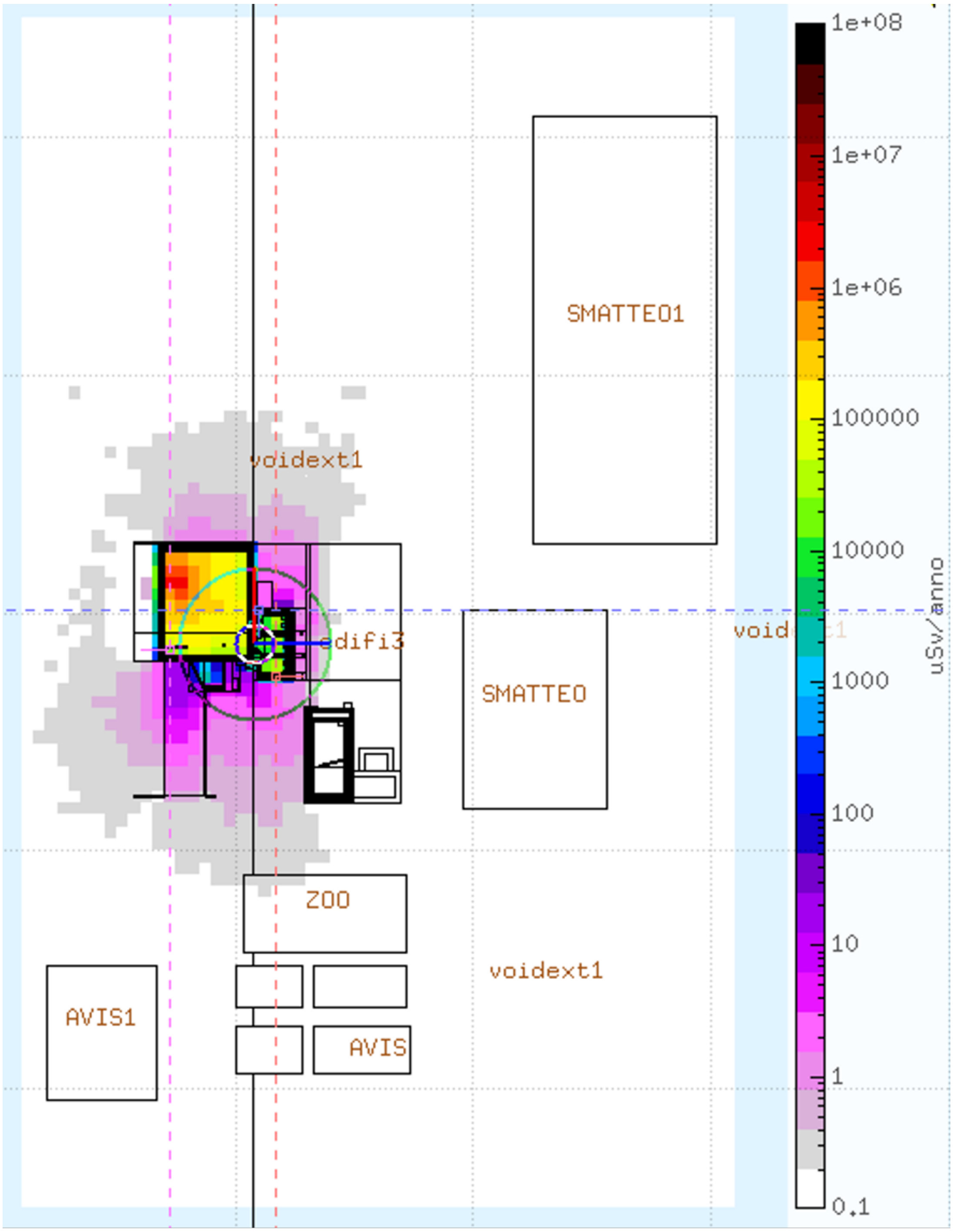

Figure 2.22: View of the surroundings of the center ambient dose equivalent map for 306 MeV/u iron ion beam, floor 0, expressed in μSv/year.

Ambient dose equivalent - floor -1

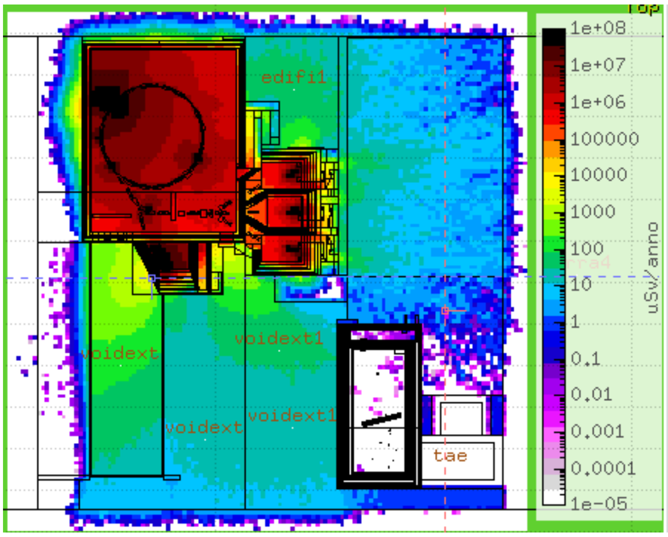

Figure 2.23: View of the internal of the center ambient dose equivalent map for 400 MeV/u carbon ion beam, floor -1, expressed in μSv/year.

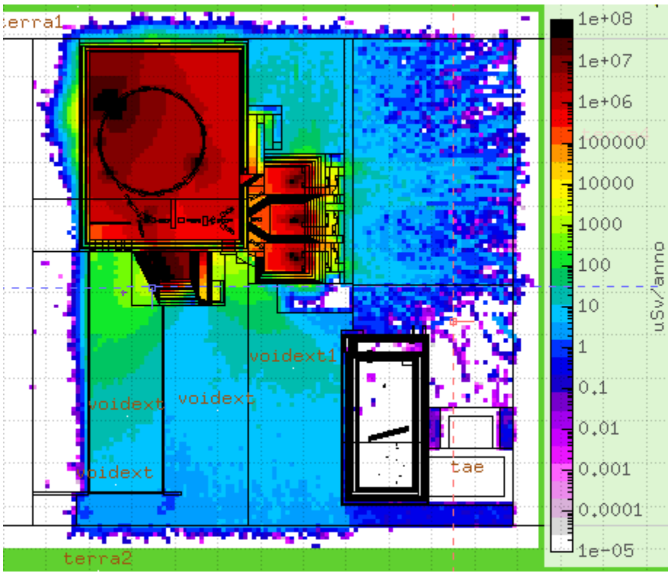

Figure 2.24: View of the internal of the center ambient dose equivalent map for 250 MeV/u helium beam, floor -1, expressed in μSv/year.

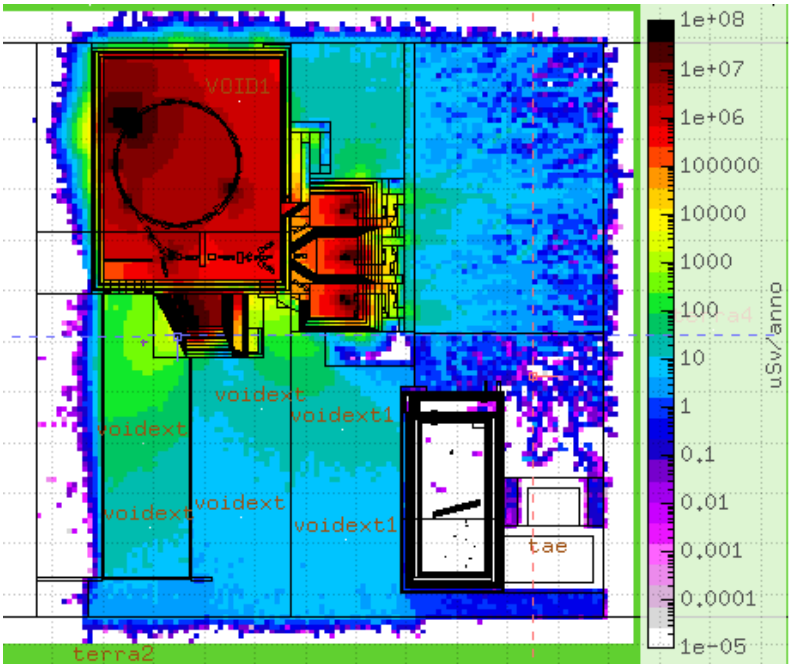

Figure 2.25: View of the internal of the center ambient dose equivalent map for 306 MeV/u lithium ion beam, floor -1, expressed in μSv/year.

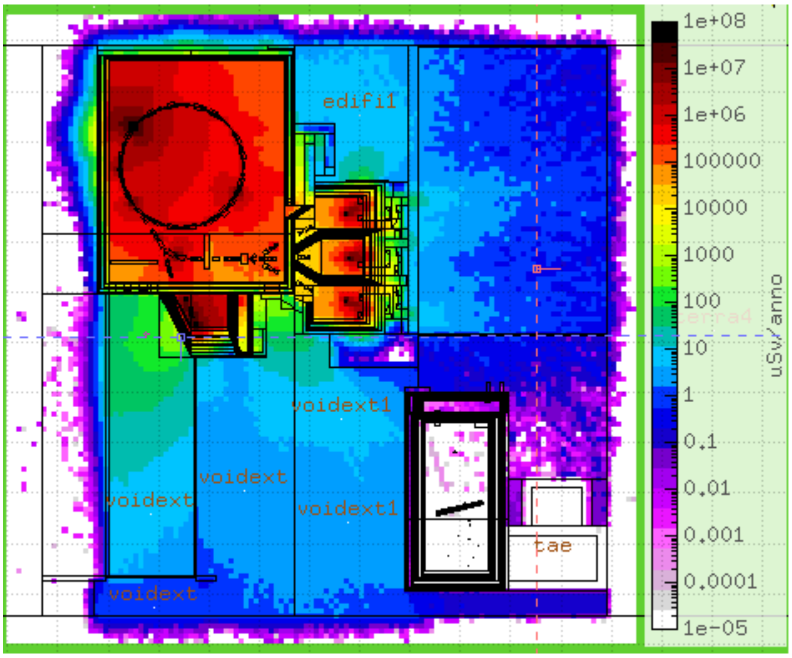

Figure 2.26: View of the internal of the center ambient dose equivalent map for 400 MeV/u oxygen ion beam, floor -1, expressed in μSv/year.

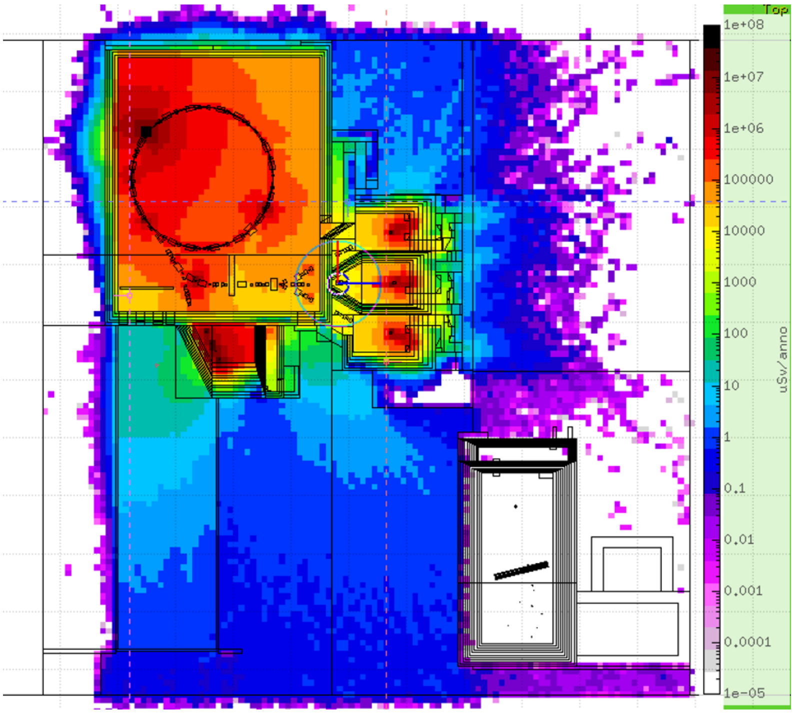

Figure 2.27: View of the internal of the center ambient dose equivalent map for 306 MeV/u iron ion beam, floor -1, expressed in μSv/year.

3 | Development of an Extended Range Rem Counter

In this chapter the characterization of a micro structured neutron detector (MSND) [56] rem counter has been carried out. The detector consist of a MSND surrounded by a polyethylene moderator and connected to a Raspberry Pi through GPIO pins. The MSND counts can be visualized in a 3.5 inches touch screen attached to the Raspberry Pi.

In the first section, the state of art of rem counters has been described with a focus on the nuclear reactions usually adopted for neutron detectors. Then, the tests conducted for the characterization of the rem counter have been presented. In particular, a square wave generator was employed to assess the suitability of the Raspberry Pi for this application. Lastly, the response function has been calculated with the Monte Carlo code FLUKA and the calibration factor and the linearity test has been evaluated at the Czech Metrology Center in Prague.

3.1 State of the art of Rem counters

Neutron detectors rely on nuclear reactions to detect neutrons. The most adopted concept is to employ reactions with the most significant cross-sections that result in the emission of charged particles. The measurable current is caused by ions losing energy inside the active volume of the detector. The primary goal of radiation protection is to establish a correlation between neutron counts and the equivalent ambient dose. Constructing neutron detectors presents a challenge because neutron energies span a wide range, from meV to GeV, and, usually, thermal neutrons exhibit high cross-sections. To detect thermal neutrons and slow down high-energy neutrons, a moderator is typically employed. In the following section, we introduce the key nuclear reactions used for thermal neutron detection.

3.1.1 Nuclear Reactions for Thermal Neutron Detectors

Rem counters use the large cross section of thermal neutrons on ^{10}B, ^{6}Li and ^{3}He to perform the primary nuclear reactions. The cross sections of the reactions are reported in Figure 3.1. The cross sections of the reactions are reported in Figure 3.1.

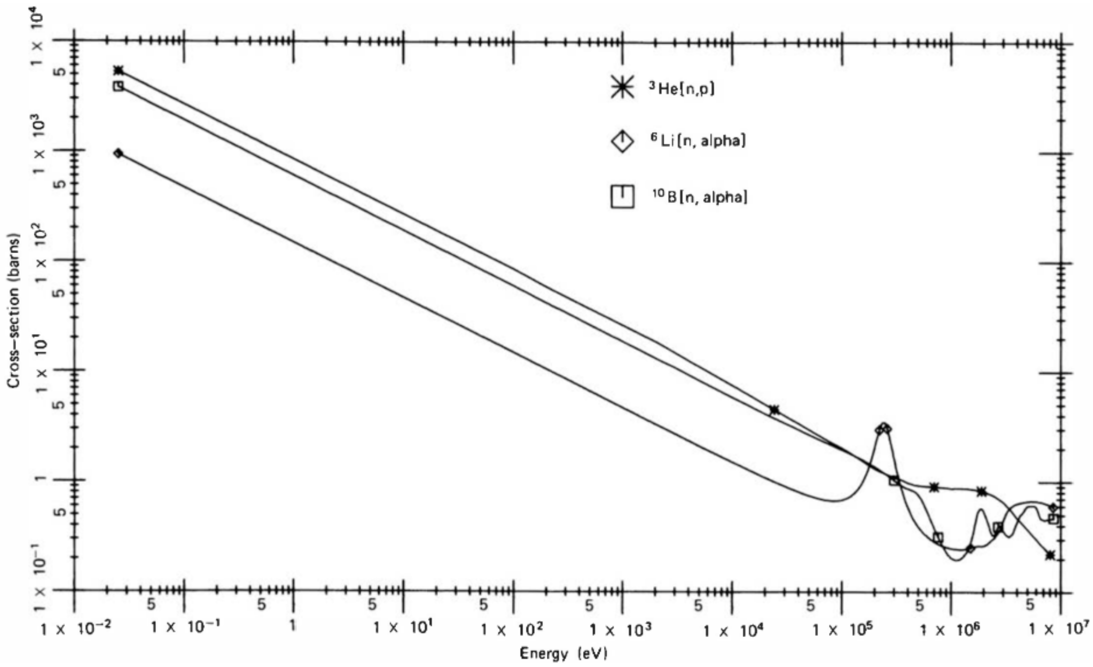

Figure 3.1: Cross sections for the nuclear reaction adopted for neutron detectors [57].

^{10}B Reaction

The thermal neutron capture on ^{10}B probably is the most widely used reaction in in detectors engineering. The reaction can be expressed as:

$$n + {}^{10}\mathrm{B} \longrightarrow \begin{cases} {}^{7}\mathrm{Li} \;\; + \alpha + 2.792\,\mathrm{MeV}\,(\mathrm{ground\,state}) \\ {}^{7}\mathrm{Li}^{*} + \alpha + 2.310\,\mathrm{MeV}\,(\mathrm{excited\,state}) \end{cases} \tag{3.1}$$

When a thermal neutron impinge on a ^{10}B target a ^{7}Li and an α particles are produced. The reaction has two possibility the first with ^{7}Li in the ground state with a Q-value of 2.792 MeV with a related branching of 6% and the second with ^{7}Li in an excited state with a Q-value of 2.310 MeV with a related branching of 94%. In this case, the energy for the emitted particles are 0.84 MeV for the ^{7}Li and 1.47 MeV for the α.

^{3}He Reaction

The other popular reaction also adopted for the detection of thermal neutron is the one based on the ^{3}He reaction:

$$n + {}^{3}\mathrm{He} \longrightarrow {}^{3}\mathrm{H} \; + \; \mathrm{p} \; + \; 0.764 \; MeV \tag{3.2}$$

If a thermal neutron impinge on a ^{3}He target a ^{3}H and a p are produced with a Q-value of 0.764 MeV. The energy for the emitted particles are 0.573 MeV for the p and 0.191 MeV for the ^{3}He.

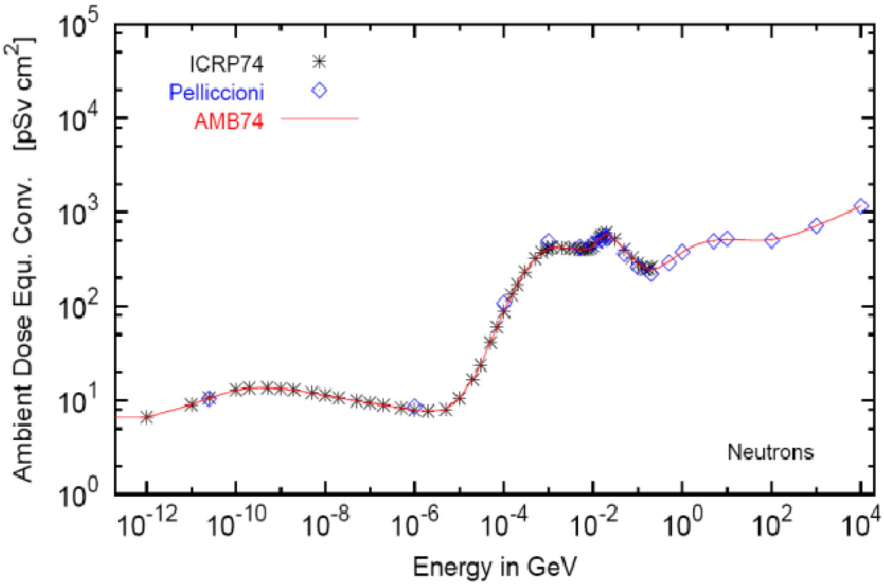

Figure 3.2: Conversion coefficient from fluence to ambient dose equivalent values for neutrons [58].

^{6}Li Reaction

Another nuclear reaction also adopted for the detection of thermal neutron is the following:

$$\mathrm{n} + {}^6\mathrm{Li} \longrightarrow {}^3\mathrm{H} \ + \ \alpha + \ 4.78 \ MeV \tag{3.3}$$

If a thermal neutron interacts on a ^{6}Li target a ^{3}H and an α are produced with a Q-value of 4.78 MeV. The ^{3}H is emitted with a energy of 2.73 MeV and the α with an energy of 2.05 MeV.

3.1.2 Rem Counters

Rem counters are the mostly used detectors for measuring neutron for ambient dose evaluations. These instruments are designed in order to have in its center a fluence of thermal neutrons proportional to the ambient dose equivalent. Mathematically the ambient dose equivalent, $H^*(10)$, can be evaluated as:

$$H^*(10) = \int_{E_{min}}^{E_{max}} h^*(10)(E)\phi(E)dE \tag{3.4}$$

$h^*(10)$ coefficients ([64]) are reported in Figure 3.2 in unit of pSv $\cdot$ cm^2 and are function of the incident neutron energy from E_{min} to E_{max}, while $\phi(E)$ represent the neutron fluence at energy E.

Due to my inability to solve the integral (3.4), $H^*(10)$ can be calculated through the sum:

$$H^*(10) = \sum_E h^*(10)(E)\phi(E) \tag{3.5}$$

The counts measured by the rem counter can be expressed as:

$$Counts = \sum_E R(E)\phi(E) \tag{3.6}$$

with $R(E)$ the response function of the rem counter as function of neutron energy. This function is calculated by the rem counter manufacturer mostly with Monte Carlo codes. From 3.5 and 3.6 it is straightforward to assess that:

$$H^*(10) \propto Counts \tag{3.7}$$

The proportionality constant can be calculated by a calibration factor and verified experimentally in a reference field with a Am-Be or ^{252}Cf a calibration source or at accredited facilities.

In Figure 3.3 the response of the most widely used commercial rem counters as function of neutron energy, expressed in counts · cm^2, is reported. It is evident that there is a significant difference between the Andersson-Braun and the Wendi and Linus (Long Interval Neutron Survey-meter) responses at high energies (>10 MeV). In fact, Wendi and Linus are extended-range rem counters with improved responses for high-energy neutrons,

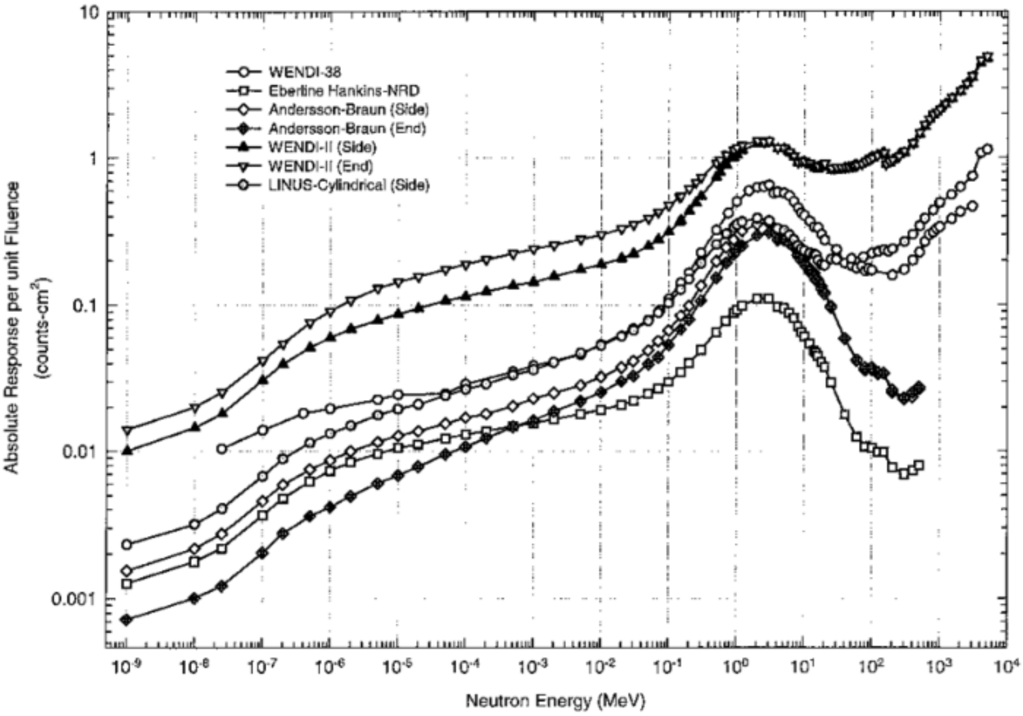

Figure 3.3: Rem counters response as function of energy [59].

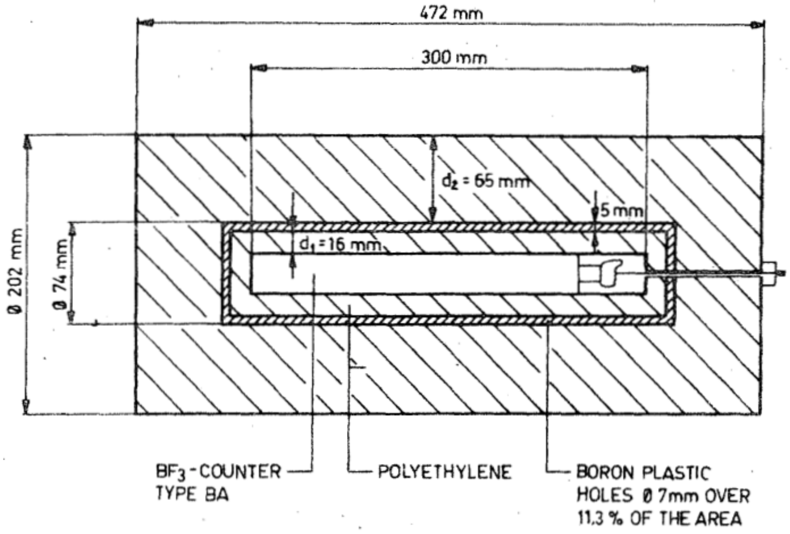

Figure 3.4: Design of Andersson-Braun rem counter

thanks to their unique moderator design. Usually, this moderator are made of a sphere polyethylene with some cadmium and lead inserts to improve the neutron detection at high energies. An example of this kind of moderator is described in [60]. In the following the most popular rem counters are introduced [60, 59, 61, 62, 63, 56].

The Andersson-Braun [61], Linus [62] and Lupin (Long interval Ultra-wide dynamic Pile-up free Neutron rem counter) [63] are examples of extended range rem counters based on BF_3, that adopts the ^{10}B reaction. In Figure 3.4 the Andersson-Braun rem counter is presented. A BF_3 proportional counter is placed in the center of two polyethylene shells with a 5 mm boron plastic insert (200 mg/cm^2). As it can be seen from Figure 3.3 the Andersson-Braun rem counter is able to detect neutrons up to 15 MeV.

An advancement of this rem counter is the Linus, whose geometry is reported in Figure 3.5. In this detector a lead layer of 1 cm is placed between the borated plastic and the outer polyethylene. This upgraded design allows the detection of neutrons up to 1 GeV. In fact, neutrons above 10 MeV interact with lead producing secondary neutrons that are then moderated by the inner layer of polyethylene and detected by the thermal neutron detector in the center of the rem counter.

The Lupin design is reported in Figure 3.6. This detector employs a different type of moderator with similar characteristics to the previous ones. The main differences are the design of the lead and the addition of cadmium inserts over the borated plastic. The substantial improvements of this device is its high sensitivity and the ability to response in intense pulsed fields up to 16 nSv/burst due to its logarithmic electronics [63].

In the next section the implementation of an extended rem counter based on a microstructured neutron detector is presented.

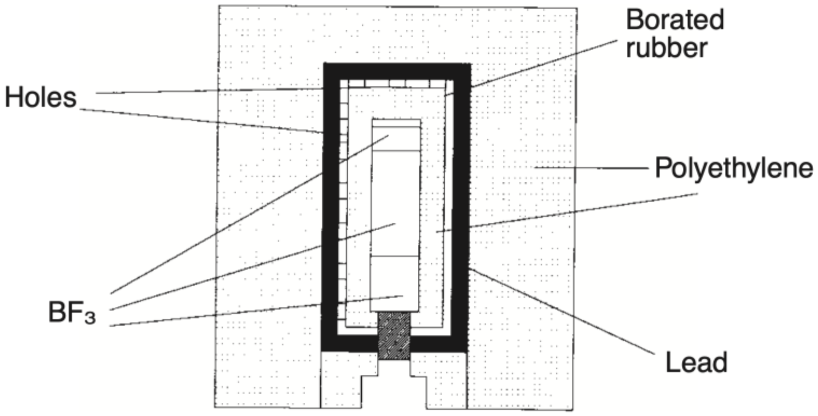

Figure 3.5: Design of the cylindrical Linus rem counter.

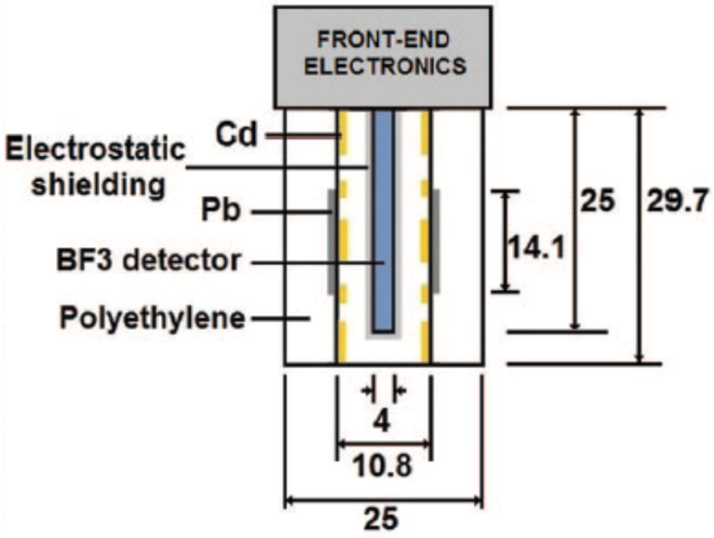

Figure 3.6: Design of the Lupin rem counter.

3.2 The MSND Extended Range Rem Counter Implementation

The rem counter consist of a microstructured neutron detector (MSND) enclosed by a plastic-based moderator witch incorporates cadmium and lead inserts to provide an extended range response. The MSND is connected to a Raspberry Pi model 4 through GPIO pins for data visualization and collection purposes.

MSND Detector and Moderator

The Domino neutron detector [56] is made of a microstructured semiconductor neutron detector (MSND®) technology with ^{6}Li conversion to yield an adjustable thermal-neutron detection efficiency of up to 30%. The active section of the detector consist of a 4 cm^2 x 0.5 μm diode. The manufactured claims a very high gamma-rejection up to 1:10^7. The sensor is equipped with an on board electronics with a pre-amplifier, shaping-amplifier, discriminator, analog-to-digital converter, temperature sensor, and voltage regulator to generate an output signal. The output signal from the Domino is a square wave with a pulse width between 5 and 50 μs. The detector Pile-up limit is $<$33 kcps or $>$66 kHz and its dead time is 150 μs, according to the detector manufacturer [56]. The pile-up limit indicates the maximum frequency at which pulses can arrive and can be detected with no superposition. If this limit is exceeded, the detector would count multiple pulses as one signal. The dead time indicates the time in which the detector acquires the incoming pulse and processes it with the electronics on board. The sensor is equipped with a pre-amplifier, shaping-amplifier, discriminator, analog-to-digital converter, temperature sensor, and voltage regulator to generate an output signal. If a signal arrives during the 150 μs dead time the pulses are not detected.

The Moderator

The moderator employed for the extended range rem counter is the one described in the reference [60] with a visual representation provided in Figure 3.7. This moderator boasts a 25 cm diameter and is constructed using two polyethylene shells separated by a lead shell, along with cadmium buttons strategically placed. At the center of this moderator, the DOMINO thermal neutron detector is installed through a polyethylene plug.

3.2.1 Testing the Connection between MSND and Raspberry Pi

The MSND is connected to the Raspberry Pi, which supplies power and allows data transmission via the General Purpose Input-Output (GPIO) pins. These GPIO pins function with on and off states, operating at a voltage of 3.3 V. In contrast, the MSND's signal is a 5 V square wave with frequencies of up to 66 kHz. The status of the GPIO pins can be monitored through Python or C scripts. The primary objective of this study is

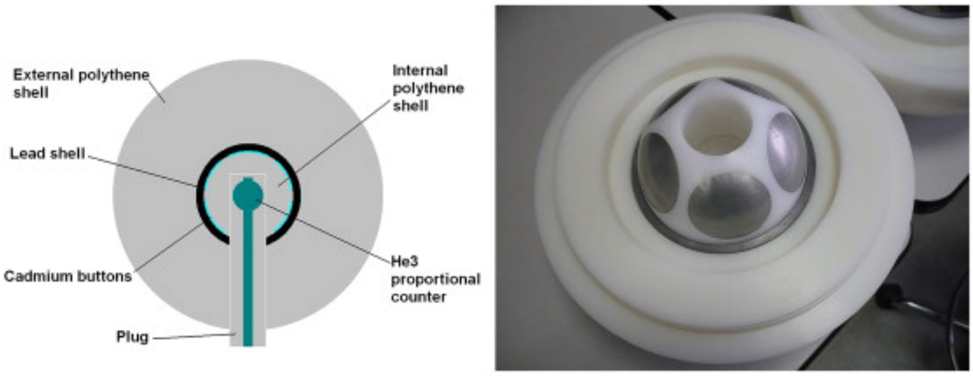

Figure 3.7: Design of the moderator adopted in this thesis [60].

to assess the Raspberry Pi system's ability to accurately measure square wave signals up to 66 kHz. In the experiments, an Arduino has been adopted as square wave generator, and the frequencies of the Arduino signals were measured using a digital oscilloscope, specifically the Picoscope 6. To evaluate the Raspberry Pi's response a Python or C script has been adopted, that update a counter when the GPIO pin is in the 'on' state.

The experimental setup is depicted in Figure 3.8. Arduino generates square waves that are routed both a digital picoscope and the Raspberry Pi via a breadboard. The signal signal is monitored on a PC using the Picoscope 6 software. Arduino has been set to generate square waves with values ranging from 0 to 5 volts, featuring a 50% duty cycle, and frequencies spanning from 1 to 90 kHz. The wavelength is set in Arduino IDE software through the command delayMicroseconds, that indicates the time of the high state (5 V) and low state (0 V) of the wave. The code used for wave generation is outlined in Figure 3.9. Finally, with the Picoscope 6, is it possible to measure the actual frequency of the wave emitted by the Arduino.

In preliminary tests, the frequency generated by the Arduino is checked using the digital Picoscope 6. The results of the measures are presented in Table 3.1. The data reveal that the Arduino can generate square waves with the frequencies of interest. However the set frequencies do not precisely match the measured ones. This discrepancy is attributed to a latency in the delay command of the Arduino. As shown in Table 3.2, the command delayMicroseconds has an inherent latency that must be taken into account. This latency is more prominent at lower frequencies and remains constant above 5 kHz, with a value of around 9 μs. Measured frequencies match the set values up to 10 kHz, but as the frequency increases, the deviation from the set frequency becomes noticeable. Importantly, this discrepancy does not pose an issue for the Raspberry Pi tests, as the actual frequency is continuously monitored by the Picoscope during each measurement.

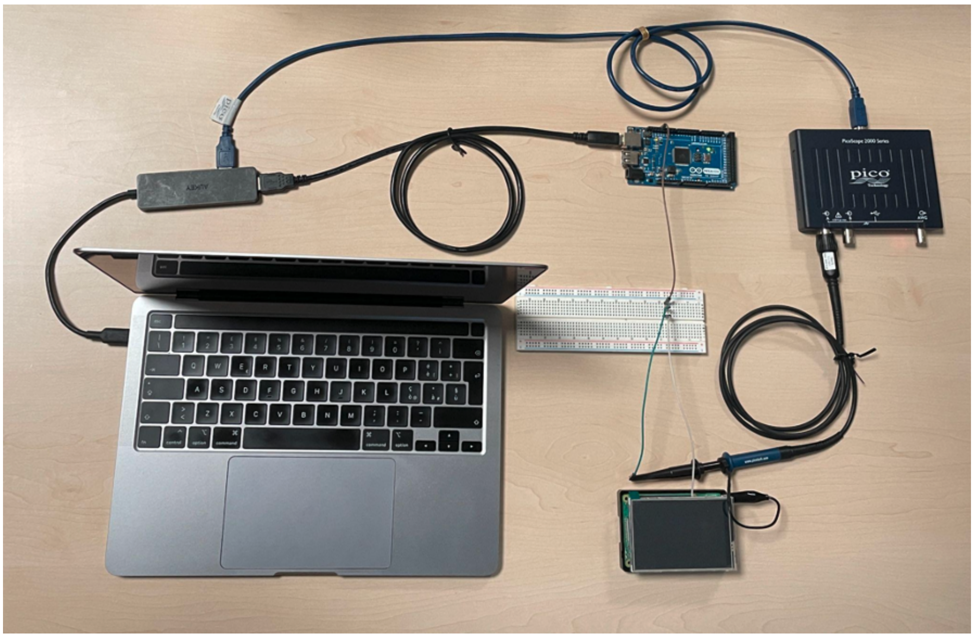

Figure 3.8: Experimental setup. From the left the Raspberry Pi, the breadboard, the Arduino and the digital picoscope.

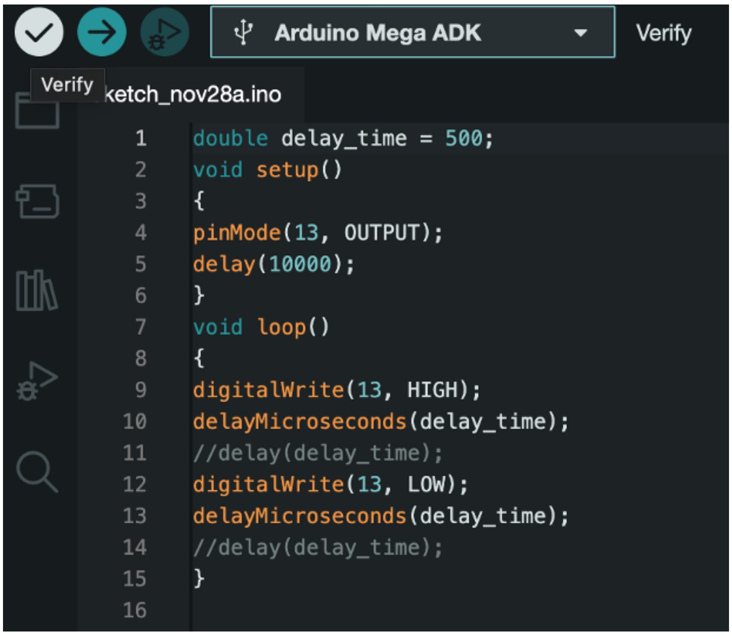

```
double delay_time = 500;
void setup()
{
pinMode(13, OUTPUT);
delay(10000);
}
void loop()
{
digitalWrite(13, HIGH);
delayMicroseconds(delay_time);
//delay(delay_time);
digitalWrite(13, LOW);
delayMicroseconds(delay_time);
//delay(delay_time);
}

```

Figure 3.9: Code used for wave generation in Arduino IDE.

Set Frequency [kHz] **Arduino**	**Measured Frequency [kHz]** **Picoscope**
0.10	0.10
0.25	0.25
0.50	0.50
1.00	0.99
2.50	2.43
5.00	4.77
10.00	9.17
20.00	17.00
33.33	25.83
50.00	34.89
100.00	53.76
125.00	60.30
166.67	68.57
250.00	79.60
500.00	90.40

Table 3.1: Comparison between frequencies set in Arduino software and frequencies measured by the picoscope.

Set Frequency **Arduino** **[kHz]**	**Measured Frequency** **Picoscope** **[kHz]**	**Set Period** **[μs]**	**Time added** **each period** **[μs]**
0.10	0.10	10000	64.41
0.25	0.25	4000	30.63
0.50	0.50	2000	19.79
1.00	0.99	1000	14.20
2.50	2.43	400	11.52
5.00	4.77	200	9.64
10.00	9.17	100	9.09
20.00	17.00	50	8.82
33.33	25.83	30	8.71
50.00	34.89	20	8.66
100.00	53.76	10	8.60
125.00	60.30	8	8.58
166.67	68.57	6	8.58
250.00	79.60	4	8.56
500.00	90.40	2	9.06

Table 3.2: Intrinsic latency of the Arduino delay command.

Data acquisition using the Raspberry Pi

The radiation protection group at CNAO has previously developed a Python code for data acquisition using the Raspberry Pi. The code logged each interaction in a text file, recording both the data and the timestamp of each count. While this implementation worked well in low rate fields, it exhibited limitations in high rates scenarios. The code may exhibit either of the following issues:

- Writing data to the text file after each count consumed significant processing time.
- Python is an interpreted language and struggles at high data rates.

A series of tests were conducted to identify and address these problems. The first issue was tackled by rewriting the Python code to display counts directly in a terminal instead of appending them to an external text file. The second problem was approached by developing code in a compiled language, specifically C. The following section presents the results of three tests:

1. The old Python code with text file logging.
2. The new Python code without text file logging.
3. C code with external text file logging.

In Figure 3.10 the Python code implemented for the first test is presented. A while loop continuously checks the state of the GPIO pin and if it detects a 5 V signal, it records the count, date, and time in a text file. For the second test, a revisited implementation of the Python code, as shown in Figure 3.11, was used. When the code reveals a signal, it displays the count directly in the terminal. The code used for the tests is detailed in Appendix B.1. This code employs the PiGPIO C library to control the GPIO pins of the Raspberry Pi and logs the counts at predefined time intervals, 1 second during the tests.

Testing the Raspberry Pi with Arduino

The data are collected using the experimental setup shown in Figure 3.8. The measured counts, as reported in Table 3.3, represent the primary values obtained from ten measurements, each lasting 60 seconds. The expected counts were determined with the assistance of the Picoscope. In Figure 3.11, we present the efficiency of the Raspberry Pi with the old code. The efficiency for each measurement was calculated by dividing the expected counts by the measured counts. As observed in Figure 3.11, the efficiency remains above 94% for frequencies up to 4.7 kHz but decreases to 57% at 9 kHz. These results indicate that the current efficiency levels are not sufficient for measuring high dose rates with the Domino detector, given its 150 μs dead-time and the 33 kcps pile-up limit.

The tests performed with the new python code are evaluated with the same methodology described previously for the old python test. Measured and expected counts obtained

```
import time
import RPi.GPIO as GPIO
import datetime


GPIO.setmode(GPIO.BCM)
GPIO.setup(26, GPIO.IN)
counter = 0
dest = "/home/pi/Desktop/pa7_100422conteggi.txt"

GPIO.add_event_detect(26, GPIO.RISING)
try:
       while True :
           if GPIO.event_detected(26):
              counter=counter+1
              print(counter)
              t = datetime.datetime.now().strftime("%Y/%m/%d-%H:%M:%S")
              vst = str(counter)
              out_file = open(dest,'a') # apre file.csv Append
              out_file.write(t + ' CEST,'+ vst + '\n' )
              out_file.close()
finally:
    GPIO.cleanup()
```

Figure 3.10: Python code adopted for tests with Arduino.

Set Frequency Arduino [kHz]	Measured Frequency Picoscope [kHz]	Measured Counts	Expected Counts
0.10	0.10	$5.96{\cdot}10^3$	$5.96{\cdot}10^3$
0.25	0.25	$1.49{\cdot}10^4$	$1.49{\cdot}10^4$
0.50	0.50	$2.97{\cdot}10^4$	$2.97{\cdot}10^4$
1.00	0.99	$5.92{\cdot}10^4$	$5.91{\cdot}10^4$
2.50	2.43	$1.46{\cdot}10^5$	$1.46{\cdot}10^5$
5.00	4.77	$2.70{\cdot}10^5$	$2.86{\cdot}10^5$
10.00	9.17	$3.17{\cdot}10^5$	$5.50{\cdot}10^5$

Table 3.3: Measured counts compared to expected counts as function of the frequency with the old python code.

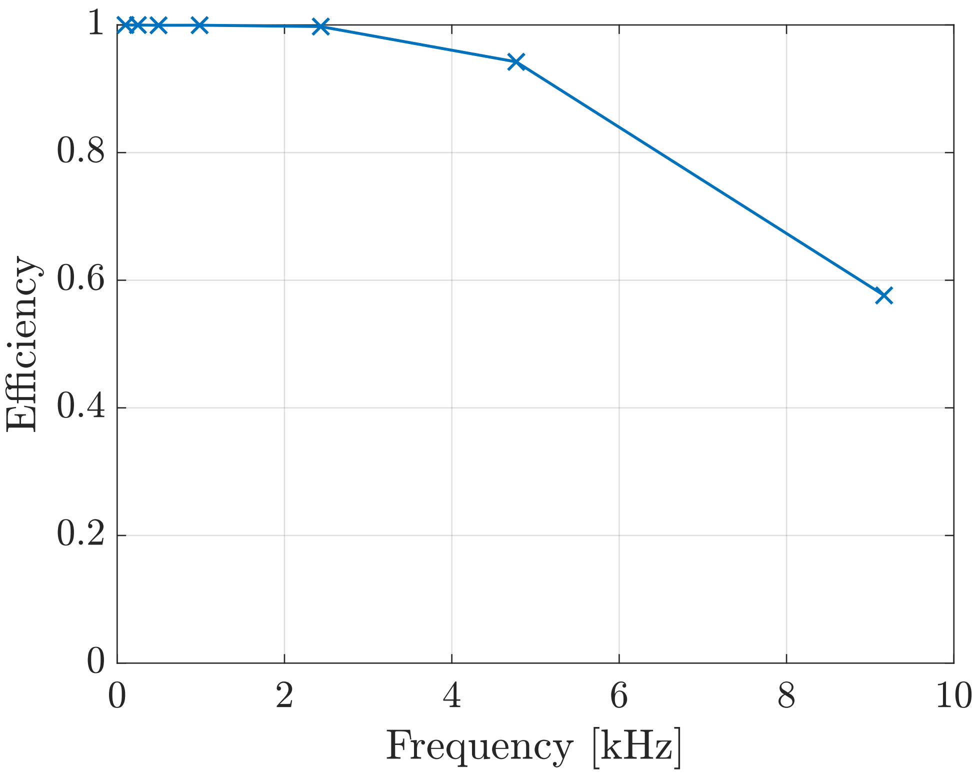

Figure 3.11: Efficiency of the experimental setup as function of the frequency measured by the Picoscope 6 with the old python code.

Set Frequency Arduino [kHz]	**Measured Frequency Picoscope [kHz]**	**Measured Counts**	**Expected Counts**
1.00	0.99	$5.92{\cdot}10^4$	$5.92{\cdot}10^4$
2.50	2.43	$1.46{\cdot}10^5$	$1.46{\cdot}10^5$
5.00	4.77	$2.86{\cdot}10^5$	$2.86{\cdot}10^5$
10.00	9.167	$5.49{\cdot}10^5$	$5.50{\cdot}10^5$
20.00	17	$1.02{\cdot}10^6$	$1.02{\cdot}10^6$
33.33	25.83	$1.54{\cdot}10^6$	$1.55{\cdot}10^6$
50.00	34.89	$2.07{\cdot}10^6$	$2.09{\cdot}10^6$
100.00	53.76	$3.22{\cdot}10^6$	$3.23{\cdot}10^6$
125.00	60.3	$3.57{\cdot}10^6$	$3.62{\cdot}10^6$
166.67	68.57	$4.06{\cdot}10^6$	$4.11{\cdot}10^6$
250.00	79.6	$4.74{\cdot}10^6$	$4.78{\cdot}10^6$
500.00	90.4	$4.54{\cdot}10^6$	$5.42{\cdot}10^6$

Table 3.4: Measured counts compared to expected counts as function of the frequency with the new python code.

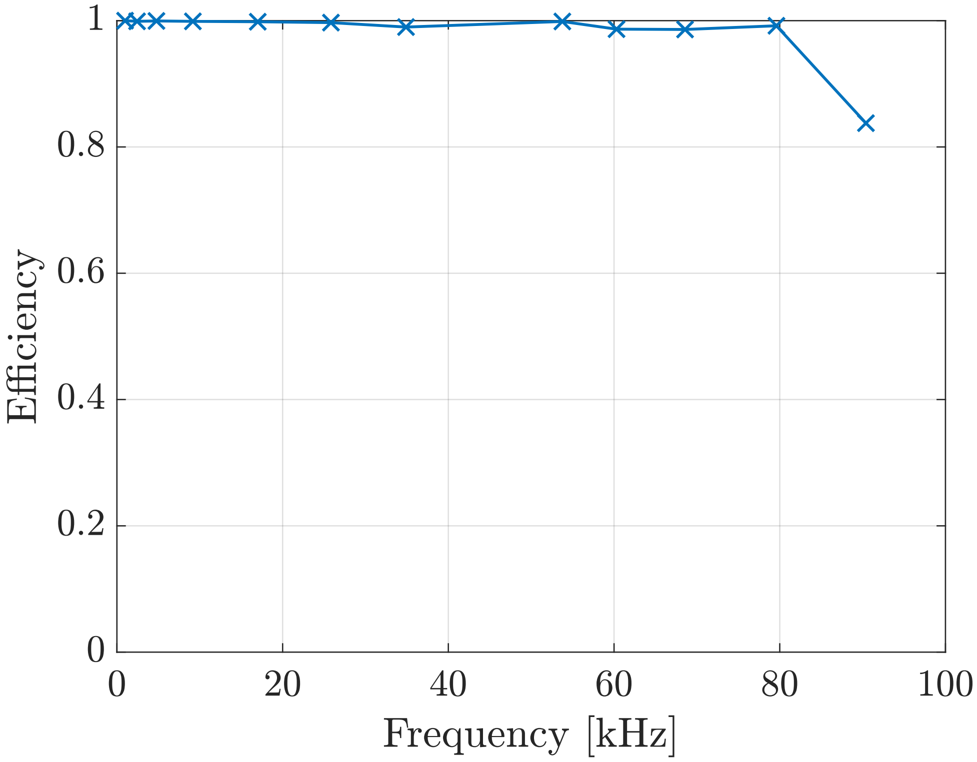

Figure 3.12: Efficiency of the experimental setup as function of the frequency measured by the Picoscope 6 with the new python.

with the new Python code are reported in Table 3.4 and in Figure 3.12 the efficiencies are shown. The results reveal that with the new code, the Raspberry Pi attains an efficiency exceeding 98% for frequencies up to 80 kHz, which significantly exceeds the pile-up limit of the Domino detector set at 66 kHz. However, this code only provides a numerical output at the end of each measurement without logging it into a file. To address this limitation, a C program was developed. This program checks the state of the diode every second and writes the data to an external text file, including the count, date, and time information. Testing the program using the experimental setup illustrated in Figure 3.8 show a 99.9% efficiency in detecting square waves, even beyond the maximum frequency of 90 kHz. For the final implementation of the rem counter software, a Python visualization code has also been developed to simplify the input of measurement parameters.

3.2.2 Software Implementation of the Rem Counter

The visualization software is written developed using the Python interface Tkinter. The final code can be found in Appendix B.1. In Figure 3.13 the interface adopted for measures is shown. With the final version, users can set various parameters for measurements, including the measurement time in seconds, the number of measurements to perform, the time between measurements, the name and location of the data file for the current measurements. The `Start Button` in the Python interface triggers the C program introduced

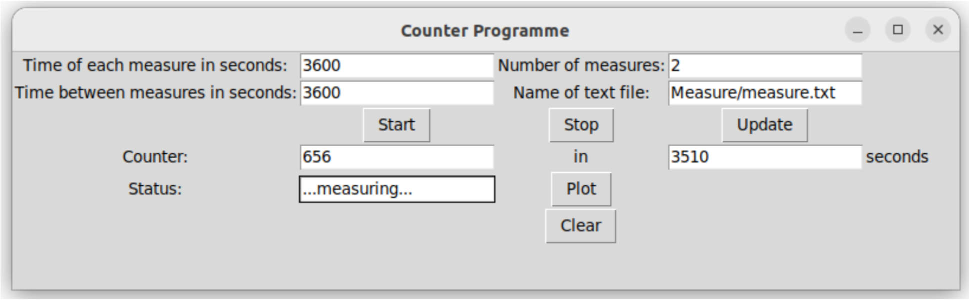

Time of each measure in seconds: 3600
Number of measures: 2
Time between measures in seconds: 3600
Name of text file: Measure/measure.txt
Counter: 656 in 3510 seconds
Status: ...measuring...

Figure 3.13: View of the counting interface written with the python interface Tkinter.

in the previous section, utilizing the input parameters provided in the user interface. The `Update Button` allows users to monitor the progress of the measurement, showing the time elapsed and the total count in the user interface. With the `Stop Button` button enables users to interrupt a measurement, with data up to that point being saved in the log file. The `Clear Button` is implemented to reset the measurement parameters. The output is a structured text file with four columns: date, time of measurement, progressive count number, and the measurement number in the series. Finally, the plot button saves data in a `data frame` python object and generates a plot of the current measure until that moment. Additionally, the `Plot Button` stores data in a Python `data frame` object and generates a plot of the current measurement. This feature provides users with a visual check of the measurement status.

3.3 Characterization of the MSND Rem Counter

The previous section was dedicated to explain the connection between the microstructured neutron detector and the Raspberry Pi, as well as the software implemented for data collection. The focus of this section is the characterization of the detector, with particular emphasis on the following aspects:

- The response function as function of the energy of the incident neutron with Monte Carlo methods;
- The calibration factor at the Czech Metrology Institute (CMI);
- The saturation as function of the dose rate at CMI.

The response function of a rem counter is a representation of the number of counts per unit fluence as a function of the energy of incident neutrons. In this thesis, this curve was computed using the Monte Carlo code FLUKA. It serves as a valuable tool to evaluate counts for the detector at various neutron fluences. As previously discussed in Section 3.1.2, the number of counts of a rem counter is directly proportional to the ambient dose equivalent, H*(10). To convert these counts into dosimetric evaluations in $H^*(10)$, they must be multiplied by a calibration factor. In this thesis, the calibration factor was determined through experimental procedures at the Czech Metrology Center in Prague, using an Am-Be source. Additionally, at CMI a linearity test of the detector has been carried out. The next section will outline the methodology employed to evaluate the response function of the rem counter.

3.3.1 Rem Counter Response Function

In this thesis, the response function of the rem counter was computed using Monte Carlo simulations with FLUKA. The simulations involved a mono-energetic neutron beam directed at the detector, considering 55 neutron energies spanning from 10^{-9} to 10^{3} MeV. The following section provides details on the simulation setup.

Geometry

The geometry of the detector is shown in Figure 3.14. At the center of the sphere, the MSND detector (depicted in Figure 3.15) is positioned. This detector is modeled with a 0.5 μm ^{6}LiF active material and is surrounded by the moderator (as shown in Figure 3.16). The active part of the detector spans 4 cm^2, and it is oriented to face the incoming neutron beam. The moderator comprises an outer sphere with a diameter of 25 cm and an inner sphere with a diameter of 11.2 cm. Within the space between these polyethylene spheres (green), there are provisions for a 6 mm lead insertion (grey) and 11 cadmium inserts, each 1 mm thick (yellow).

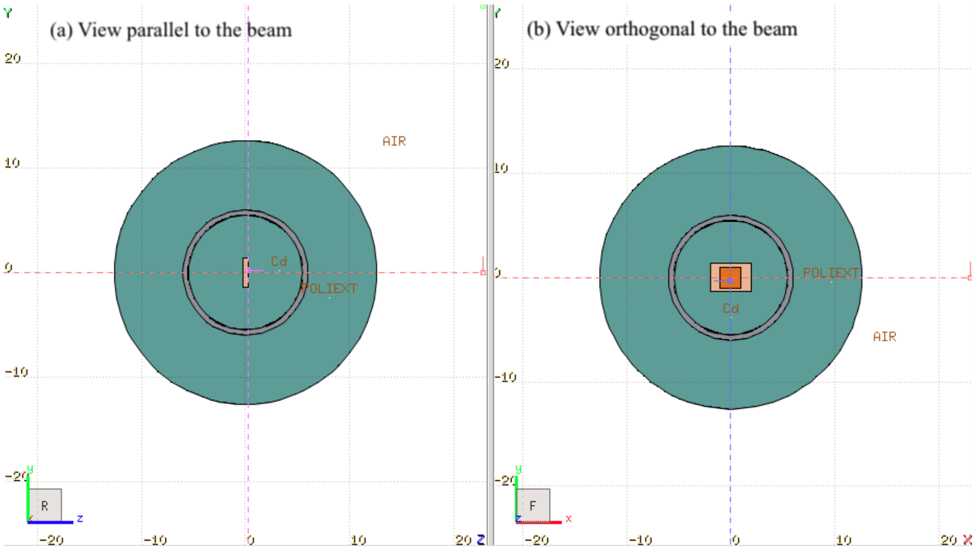

Figure 3.14: Geometry of the detector adopted in the Monte Carlo simulations. (a) View parallel to the beam. (b) View orthogonal to the beam.

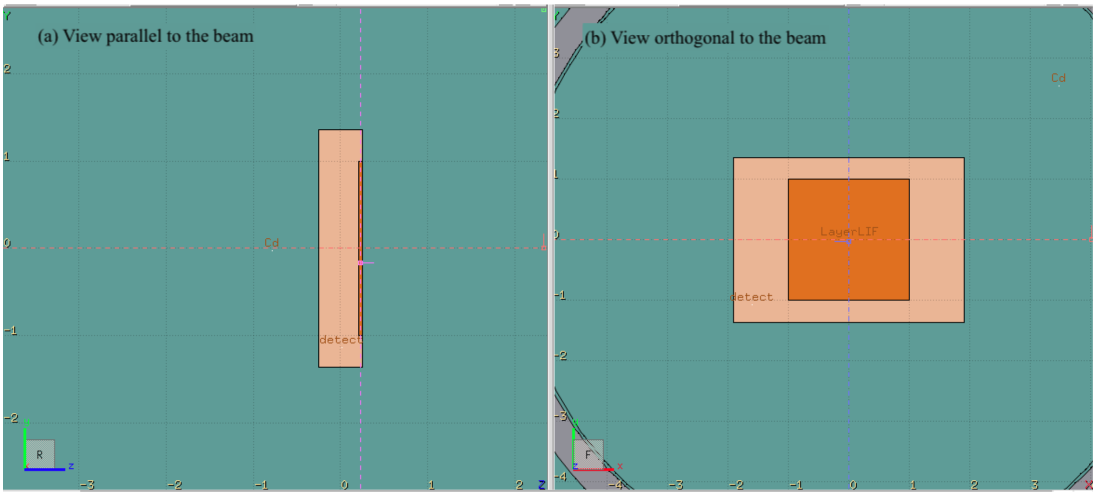

Figure 3.15: Geometry of the MSND adopted in the Monte Carlo simulations. (a) View parallel to the beam. (b) View orthogonal to the beam.

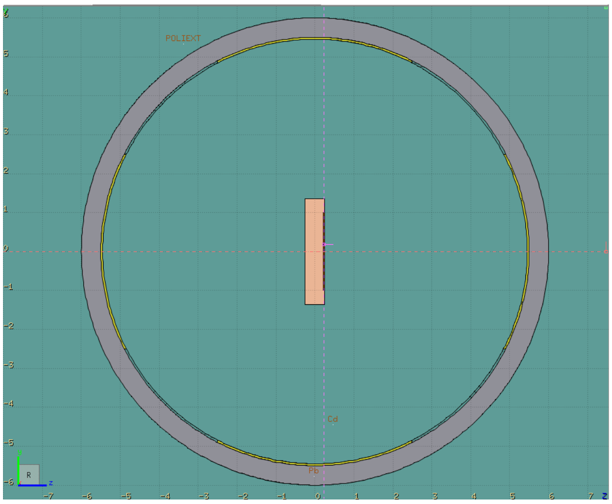

Figure 3.16: Design of the moderator adopted in the Monte Carlo simulations.

Beam

A mono-energetic neutron beam with a 25 x 25 cm^2 cross-sectional area was utilized for the simulations to irradiate the entire instrument. The rem counter was tested with 55 neutron energies, ranging from 10^{-9} to 10^3 MeV.

Results

Data were collected using the FLUKA card `DETECT` and normalized per unit of fluence. `DETECT` allows the user to calculate the number of counts generated inside the MSND for a fixed neutron energy. An example of the counts in each bin as a function of the energy deposition inside the MSND is presented in Figure 3.17. The energy deposition exhibits a distinct peak at 4.78 MeV, which corresponds to the Q-value of the thermal neutron reaction with ^{6}Li, as described in Formula 3.3.

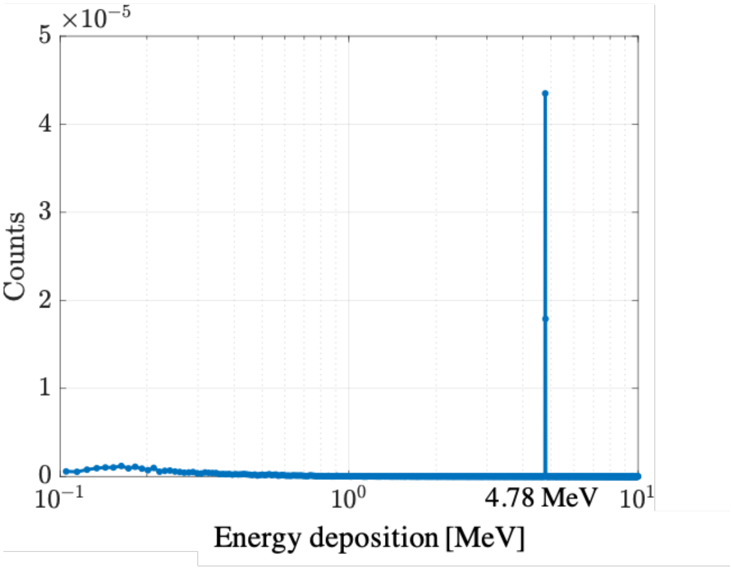

Figure 3.17: Plot of output of the card DETECT.

In Figure 3.18, the response expressed in counts·cm^2 as a function of the incident neutron energy is expressed. A qualitative comparison of the response functions of the MSND rem counter and other detectors found in the literature is possible from Figure 3.3. These plots exhibit a similar trend, with the response function increasing with energy, peaking around 2-3 MeV, reaching a minimum around 20 MeV, and then rising again at higher energies. In the following paragraph, the experimental conditions for measurements conducted at CMI and the evaluation of the calibration factor for the detector are presented.

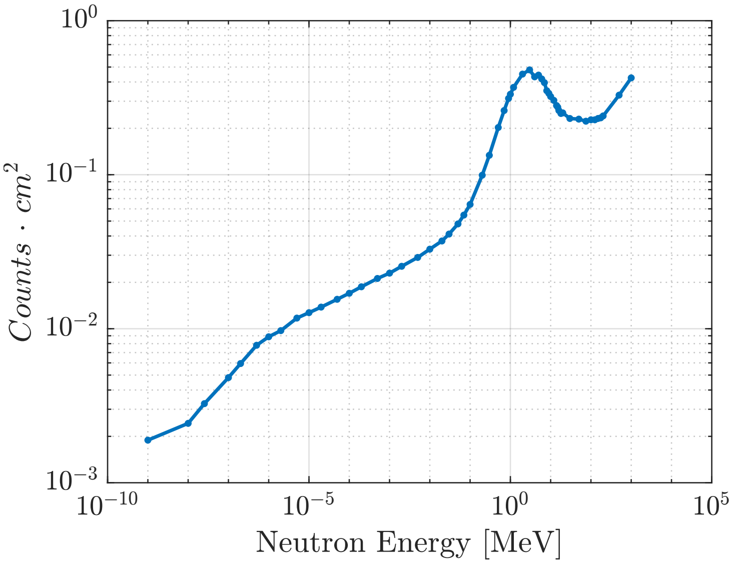

Figure 3.18: Response expressed in $counts \cdot cm^2$ of the rem counter as function of the incident neutron energy.

Furthermore, the comparison between the response function and the ICRP coefficients up to 1 GeV [64] is presented.

3.3.2 Calibration Factor Evaluation

In order to compare the detector's response curve with ICRP coefficients, it is necessary to calculate the calibration factor, denoted as k. This factor is used to convert the counts into pSv·cm^2. As mentioned earlier, the rem counter is designed in such a way that the number of thermal neutrons at the center of the moderator is proportionate to $H^*(10)$, irrespective of the neutron spectrum. Consequently, a single calibration factor can be calculated and applied to measurements for all neutron energies. Typically, the calibration process is carried out using a low-rate Am-Be or ^{252}Cf source.

Czech Metrology Institute

Calibration and metrological reliability confirmation measurements of both active and passive instruments used at the Czech Metrology Institute (CMI) were conducted at CNAO's Radiation Protection Service. CMI is an experimental facility located in Prague specializing in the calibration of instruments using various measurement standards. At CMI's Unit of Primary Metrology of Ionizing Radiation, there are radioactive sources for instrument calibration and calibrations related to environmental dose equivalents from neutrons. A picture of the calibration room at CMI is presented in Figure 3.19. Measurements were performed to metrologically verify neutron detectors, both active and passive, in use at CNAO. The measurements utilized Am-Be and ^{252}Cf sources at dose rates ranging from 30 μSv/h to 20 mSv/h, in locations where the neutron field and relative dose rates are certified. CMI maintains the primary standard (ECM 440-2/97-003) for the

Figure 3.19: The calibration room at CMI.

spectral response of neutron fluxes emitted at standard positions from these sources. By multiplying the neutron flux values by the coefficients provided by ICRP, dose values are obtained. The instruments tested included FHT 762 (serial numbers 42540/85 - 0160 and 42540/85 - 0156), CR39 trace dosimeters within passive rem counters, and active rem counters using MSNDs. The calibration factor for MSNDs was calculated using the following formula:

$$k = \frac{H^*(10)}{counts}; \tag{3.8}$$

where ambient dose equivalent, $H^*(10)$, and the counts are integrated over the measurement time t. The measurements were conducted with the detector positioned 50 cm from an Am-Be source with a dose rate of 36 $\pm 1.656\%$ μSv/h. Nine MSNDs were tested, each with one measurement. The positioning of the rem counter and the Am-Be source is depicted in Figure 3.20, and an example of the Am-Be spectrum is shown in Figure 3.21.

Figure 3.20: Positioning of rem counter in CMI calibration room with the Am-Be source.

As depicted in Figure 3.21, the peak of the spectrum is in correspondence of the maximum of the response function. The results of the measurements are presented in Table 3.5 and plotted in Figure 3.22. The mean value of the counts is 4785 ± 69 and the mean calibration factor can be calculated using the Formula 3.8:

$$k = \frac{6000\,[nSv]}{4785\,[counts]} = 1.25 \pm 0.06\, nSv/counts \tag{3.9}$$

The plot in Figure 3.23 shows the relationship between the detector's response, measured in ambient dose equivalent per unit fluence (Sv$\cdot$cm^2), and the incident neutron energy. The detector's response is also compared to the ICRP coefficients [64]. This behavior is

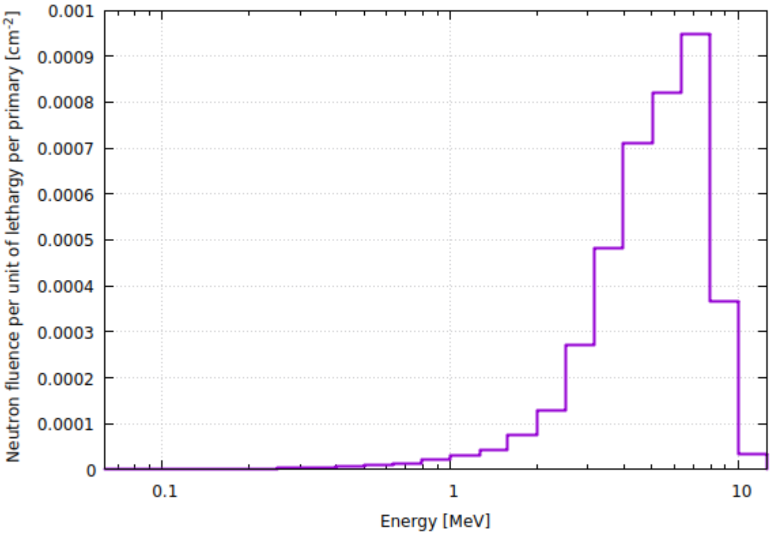

Figure 3.21: Lethergy plot of an Am-Be source.

Table 3.5: Results of the measures to calculate the calibration factor of the rem counter.

Diode Number	**Counts**	**Ref. Dose [μSv]**	**Cal. Coefficient [nSv/count]**
1	4896 ± 70	6.0 ± 0.3	1.23 ± 0.07
2	4420 ± 66	6.0 ± 0.3	1.36 ± 0.08
3	4773 ± 69	6.0 ± 0.3	1.26 ± 0.08
4	4912 ± 70	6.0 ± 0.3	1.22 ± 0.07
5	4907 ± 70	6.0 ± 0.3	1.16 ± 0.07
6	5148 ± 72	6.0 ± 0.3	1.17 ± 0.07
7	4715 ± 69	6.0 ± 0.3	1.27 ± 0.08
8	4727 ± 69	6.0 ± 0.3	1.27 ± 0.08
9	4567 ± 68	6.0 ± 0.3	1.31 ± 0.08

common for rem counters, as they are typically calibrated with neutron sources peaking around 1-2 MeV. The differences between the curves, as previously highlighted, are mainly attributed to the moderator's response.

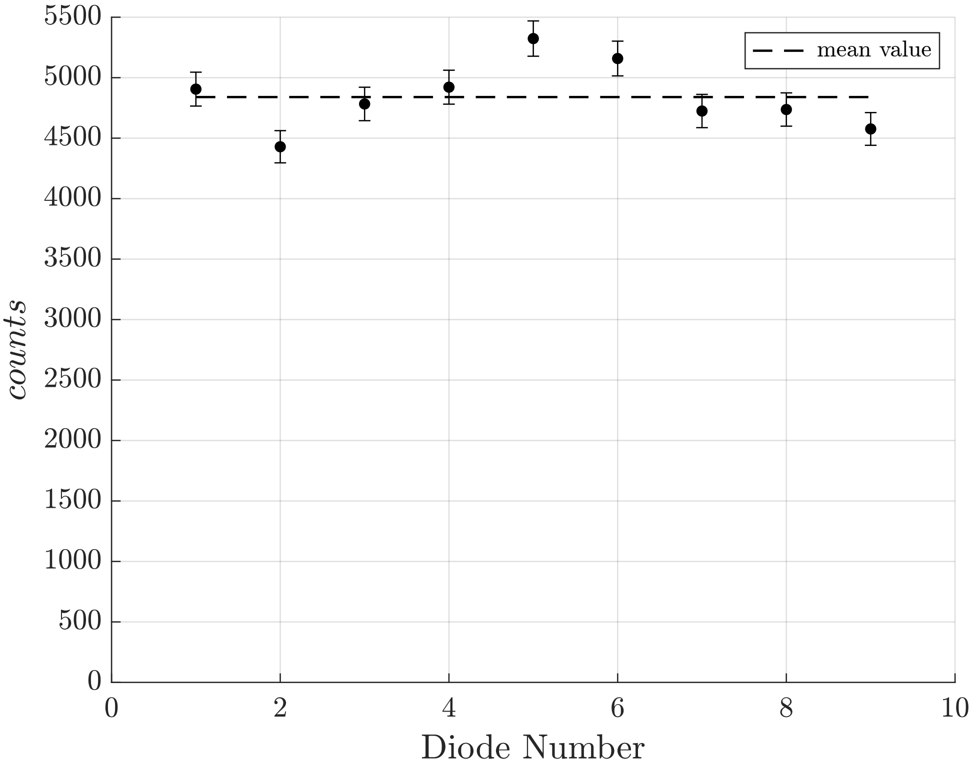

Figure 3.22: Plot of counts with mean value for 9 MSNDs.

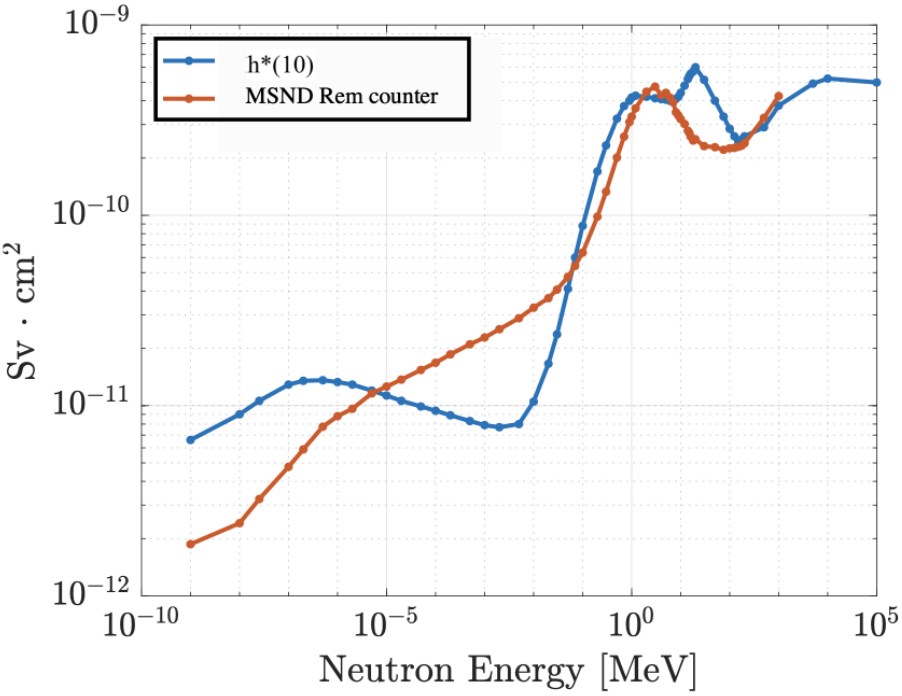

Figure 3.23: Response of the detector in ambient dose equivalent per unit of fluence, [Sv·cm^2], as function of the energy of the incident neutron compared with ICRP coefficients [64].

3.3.3 Linearity test of the Rem Counter

The saturation of the detector has been evaluated through a linearity test. In Figure 3.24, the counts per hour as a function of the dose rate in mSv/h are displayed. These measurements were conducted using a single MSND with a measurement duration of 5 minutes. The data is provided in Table 3.6. The 6% margin of error has been determined, taking into consideration the same percentage error as estimated for the calibration factor.

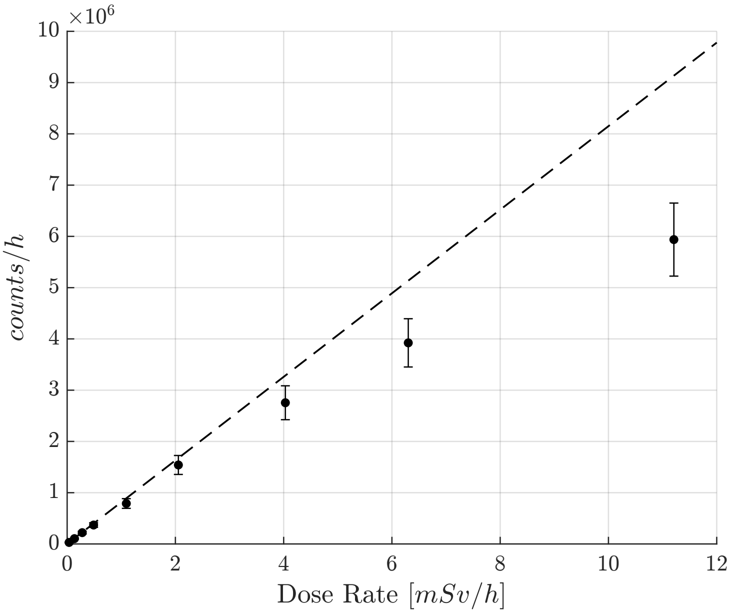

Figure 3.24: Plot of the linearity test of the rem counter.

Table 3.6: Results of the measurements for the linearity test of the rem counter.

Dose Rate [mSv]	**counts/h**
0.36	$2.94{\cdot}10^4 \pm 6\%$
0.14	$1.04{\cdot}10^5 \pm 6\%$
0.28	$2.21{\cdot}10^5 \pm 6\%$
0.49	$3.69{\cdot}10^5 \pm 6\%$
1.09	$7.89{\cdot}10^5 \pm 6\%$
2.05	$1.54{\cdot}10^6 \pm 6\%$
4.03	$2.75{\cdot}10^6 \pm 6\%$
6.30	$3.92{\cdot}10^6 \pm 6\%$
11.21	$5.94{\cdot}10^6 \pm 6\%$

The results indicate that the rem counter is reliable for dose rates up to 2 mSv/h, considering a two sigma error. Furthermore, the response it can be considered accettable for application up to 6 mSv/h. This finding ensures the reliability of MNSDs in high dose rate fields.

4 | Experimental Campaigns at CERN and CNAO

After calibrating the rem counter and testing its saturation limits, a series of measurements were conducted at the CERF facility at CERN. The instruments were tested in three different fields:

- The calibration room with an Am-Be source
- The concrete roof and the concrete side
- The iron roof

4.1 Measurements Performed at CERN Calibration Room

The CERN Radiation Protection Group operates a calibration facility where they annually calibrate about 8000 dosimeters and hundreds of portable and fixed detectors. The core of this facility is the calibration hall, a 13x13x13 m^3 room that is partially underground, utilizing the ground as shielding. The room is further shielded with 80 cm of concrete for the walls and 40 cm for the roof. The floor consists of a stainless steel grid to minimize neutron scattering. This calibration room is used for calibrating area monitors, dosimeters, and testing prototype detectors with both neutron and photon sources. The calibration room is shown in Figure 4.1 with the calibration bench and the source storage. Multiple Am-Be sources with different activities are available at the facility, ranging from 888 GBq to 100 MBq, ensuring a range of dose rates from μSv/h to mSv/h. These sources are stored in borated polyethylene containers covered by steel and are surrounded by 80 cm of concrete blocks. They can be remotely extracted using a pneumatic system. Detectors can be placed on the calibration bench and controlled from a control room, providing a safe and controlled environment for calibration, as shown in Figure 4.1.

The rem counters were tested using a 100 GBq Am-Be source, with dose rates of 80 and 200 μSv. The results of the measurements are summarized in Table 4.1. The data show excellent agreement between the reference and calculated doses. The calibration factor used for these measurements was the previously calculated value of 1.25 ± 0.06 nSv/count. The error on the measured dose was evaluated by propagating the calibration

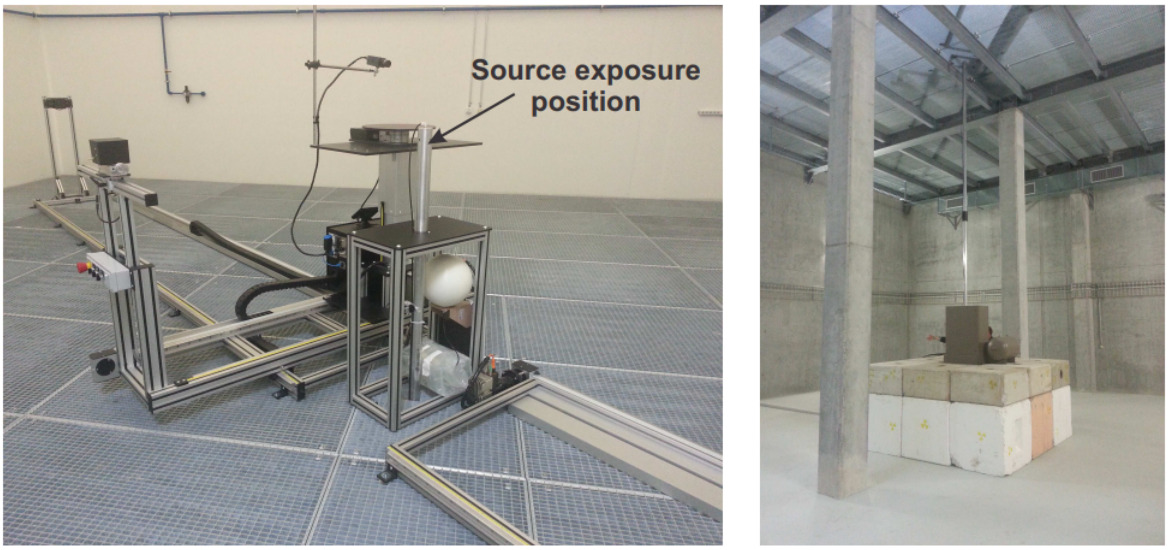

Figure 4.1: Photo of calibration facility at Cern with the exposure tube and calibration bench on the left and the source storage on the right [65].

Table 4.1: Measures at calibration facility at Cern.

Meas. Number	**Dose Rate [μSv/h]**	**Integrated Dose [μSv]**	**Meas. Dose [μSv]**
1	200	10	10.8 ± 0.6
2	200	10	9.5 ± 0.6
3	200	10	9.6 ± 0.6
4	80	5	4.7 ± 0.3
5	80	5	5.2 ± 0.3
6	80	5	4.8 ± 0.3
7	80	5	5.3 ± 0.3
8	80	5	4.8 ± 0.3
9	80	5	5.2 ± 0.3

factor's error. These measurements confirm the accuracy and reliability of the calibration factor determined at the Czech Metrology Institute.

4.2 Measurements Performed at CERF Facility

The CERF facility at CERN is located in the North Experimental Area and is primarily used for dosimetry measurements with a 450 GeV/c proton beam provided by the Super Proton Synchrotron (SPS). The facility's geometry, as simulated in FLUKA, is depicted in Figure 4.2, showing reference positions for measurements [66], [30]. Measurements at CERF can be performed in reference positions on either the concrete or iron roof. The neutron fields in these positions is produced by the interaction of a 120 GeV/c proton beam with a 50 cm thick copper target, which can be positioned under the iron or concrete roof, generating fields with different neutron spectra. There are two reference areas of 2x2 m^2, divided into 50x50 cm^2 reference positions. Additionally, there are eight scoring positions on the side of the copper target. Reference dosimetric values have been evaluated using Monte Carlo simulation and rem counters by CERN staff, as detailed in a previous work [30]. These values are well below the 2 mSv/h saturation limit determined in the linearity test. The measured reference dose rates for different positions are as follows:

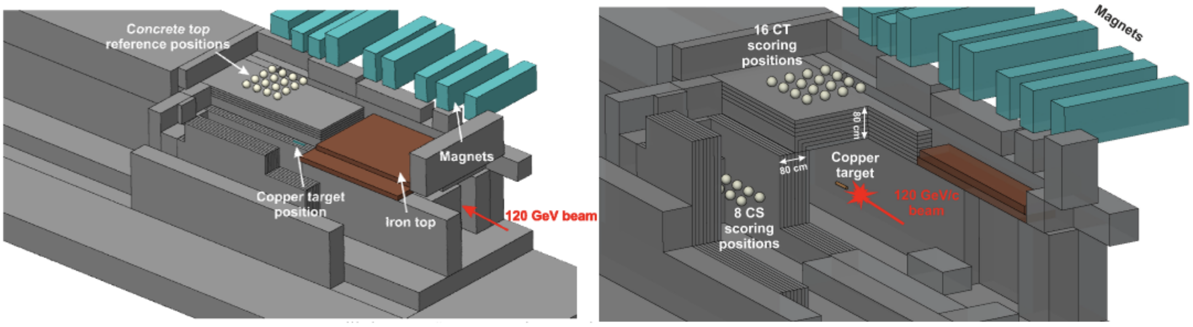

Figure 4.2: Geometry of the facility build in FLUKA [66], [30], showing reference positions.

- CS (Concrete Side): 5-250 μSv/h;
- CT (Concrete Top): 5-250 μSv/h;
- IT (Iron Top): 18-360 μSv/h.

The reference dosimetric values obtained from the CERF facility are indeed well below the saturation limit of 2 mSv/h, as determined in the linearity test discussed in Section 3.3.3. This confirms that the rem counter can reliably operate in the specified reference positions at the facility without reaching its saturation limit. Furthermore, the ability of the facility to supply IC-Counts for each measurement enables the assessment of $H^*(10)$. These IC-Counts can be used for validating measurement results and assessing the accuracy of the rem counter's response in different positions, considering both incident particle fluence and ionization chamber counts. The combination of reference dosimetric values and IC-Counts, along with the detailed characteristics of the facility's neutron spectra, enhances the reliability and accuracy of the measurements conducted at CERF.

Another important consideration in these measurements is the examination of spectra at the designated reference positions. Figure 4.3 illustrates the spectra obtained at three specific locations: one on the concrete top (CT8), another on the concrete side (CS2), and a third on the iron top (IT4). These spectra are considered as representative of all reference positions. As depicted in Figure 4.3, it becomes evident that there is a disparity in neutron emissions when examining a lethargy plot on the iron top (IT) in comparison to the spectra observed on the concrete side (CS) and the concrete top (CT). All these spectra exhibit common features, including a thermal neutron peak (ranging from 10^{-8} to 10^{-7} MeV), an evaporation peak (at around 10^{2} MeV), and a spallation peak (around 100 MeV). However, the IT spectrum also displays a broader peak between 10^{-2} and 10^{0} MeV.

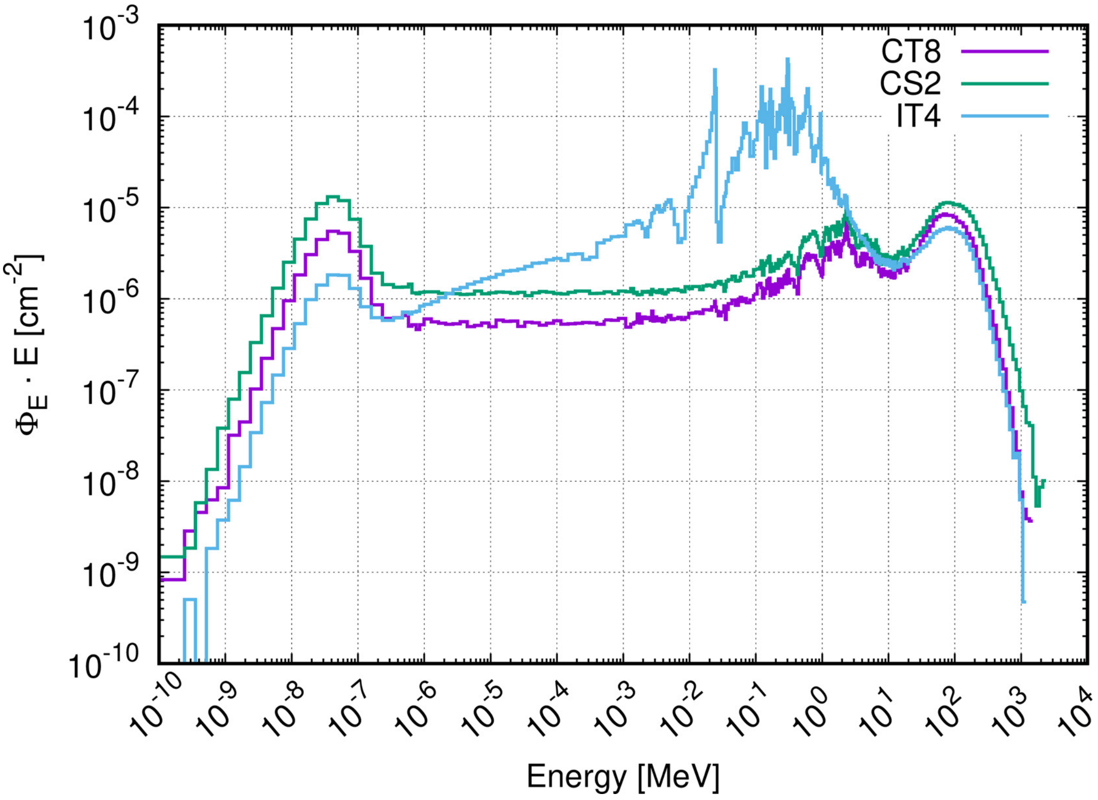

Figure 4.3: Neutron lethargy plot on the concrete top (CT8), the concrete side (CS2) and on the iron top (IT4) [30].

Results

Figure 4.4, illustrates the available positions for measurements on the concrete top (CT positions). The results of the measurements on the concrete side, the concrete top, and the iron top are presented in Tables 4.2, 4.3, and Table 4.4, respectively. The rem counter dose rate is calculated by multiplying the adopted calibration factor (1.25 nSv/count) by the counts recorded on the MSND. The FLUKA dose rate is computed by multiplying

Table 4.2: Results of the measurements performed on the concrete side.

Meas. Number	**Pos**	**Meas. Time [m]**	**FLUKA H*(10) [μSv]**	**Rem Counter H*(10) [μSv]**	**Ratio Rem C./FLUKA**
1	CS1	30	12.21	10.15	0.83
2	CS1	31	13.21	11.15	0.84
3	CS1	30	25.44	18.67	0.73
4	CS1	24	19.14	16.12	0.84
5	CS1	23	18.05	15.38	0.85
6	CS1	19	14.05	11.62	0.83
7	CS1	15	76.11	60.73	0.80
8	CS1	17	48.20	41.99	0.87
9	CS1	10	37.15	32.08	0.86
10	CS1	11	37.31	32.27	0.86
11	CS1	11	35.61	30.41	0.85
12	CS2	30	12.60	11.63	0.92
13	CS2	31	13.64	14.10	1.03
14	CS2	30	26.27	23.00	0.88
15	CS2	24	19.76	18.43	0.93
16	CS2	23	18.64	17.35	0.93
17	CS2	19	14.51	13.52	0.93
18	CS2	15	78.59	72.43	0.92
19	CS2	17	49.78	38.73	0.78
20	CS2	10	38.36	30.02	0.78
21	CS2	11	38.53	30.20	0.78
22	CS2	11	36.77	25.78	0.70

Table 4.3: Results of the measurements performed on the concrete top.

Meas. Number	**Pos**	**Meas. Time [m]**	**FLUKA H*(10) [μSv]**	**Rem Counter H*(10) [μSv]**	**Ratio Rem C./FLUKA**
1	CT1	17	28.32	22.44	0.79
2	CT1	10	21.82	17.42	0.80
3	CT1	11	21.92	17.33	0.79
4	CT1	11	20.92	16.66	0.80
5	CT10	12	17.21	15.05	0.87
6	CT10	10	12.81	11.47	0.90
7	CT10	10	8.45	7.87	0.93
8	CT10	15	8.86	8.45	0.95
9	CT10	6	23.60	20.31	0.86
10	CT11	12	17.28	16.12	0.93
11	CT11	10	12.86	12.22	0.95
12	CT11	10	8.48	8.15	0.96
13	CT11	15	8.89	8.53	0.96
14	CT11	6	23.70	22.05	0.93
15	CT2	12	14.05	12.85	0.91
16	CT2	10	10.46	9.93	0.95
17	CT2	10	6.90	6.70	0.97
18	CT2	15	7.23	7.02	0.97
19	CT2	6	19.27	17.84	0.93
20	CT3	17	29.75	25.45	0.86
21	CT3	10	22.93	19.74	0.86
22	CT3	11	23.03	20.01	0.87
23	CT3	11	21.98	18.13	0.82
24	CT3	12	13.98	11.69	0.84
25	CT3	10	10.41	8.69	0.83
26	CT3	10	6.86	5.88	0.86
27	CT3	15	7.20	6.22	0.86
28	CT3	6	19.18	16.32	0.85
29	CT5	17	34.04	29.04	0.85
30	CT5	10	26.23	22.06	0.84
31	CT5	11	26.35	22.31	0.85
32	CT5	11	25.15	21.66	0.86

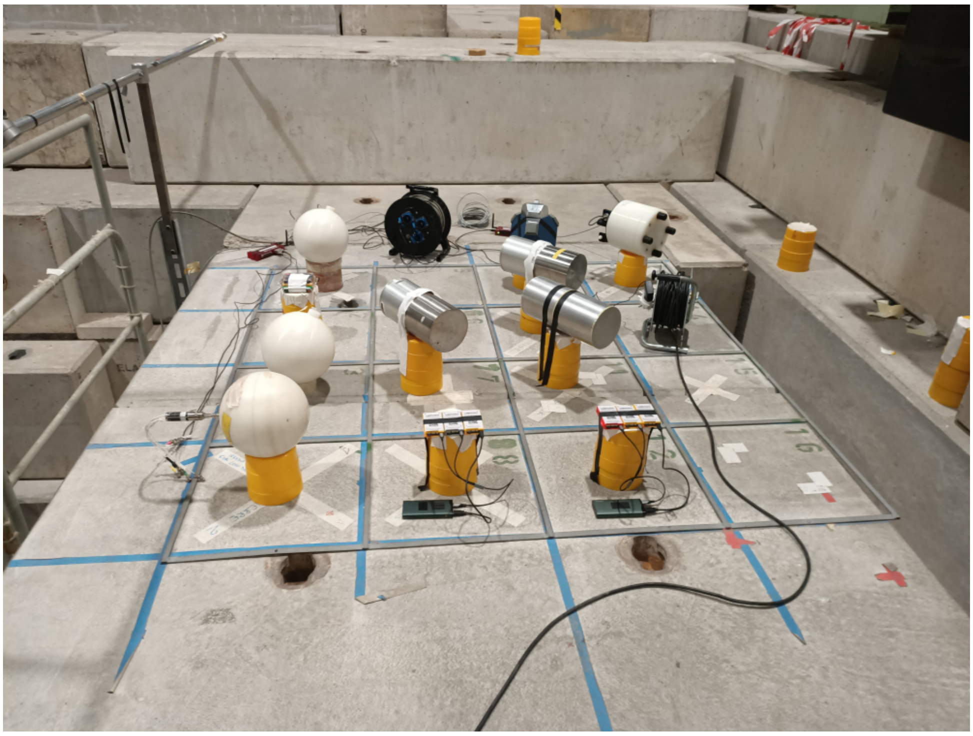

Figure 4.4: Positions available on the concrete top (CT).

the FLUKA reference values at a given reference position by the IC-counts provided by the facility team. The data indicate a consistent underestimation of the ambient dose equivalent on the concrete side by approximately 15% with a standard deviation of 1%. Similarly, for the concrete top, there is an average underestimation of 12% with a standard deviation of 1%.

The measurements carried out on the iron top reveal a more significant underestimation, approximately 30% with a standard deviation of 2%, when compared to FLUKA reference values. This elevated underestimation, in contrast to the concrete positions, can be attributed to the varying neutron emissions from the iron top, as they fall within an energy range where the rem counter tends to underestimate the ICRP coefficients.

Table 4.4: Results of the measurements performed on the iron top.

Meas. Number	**Pos**	**Meas. Time [m]**	**FLUKA H*(10) [μSv]**	**Rem Counter H*(10) [μSv]**	**Ratio Rem/FLUKA**
1	IT1	3	16.19	11.06	0.68
2	IT1	3	15.16	10.10	0.67
3	IT1	5	13.95	9.22	0.66
4	IT1	5	16.45	10.89	0.66
5	IT1	3	14.07	9.41	0.67
6	IT14	3	17.84	13.18	0.74
7	IT14	3	16.72	11.46	0.69
8	IT14	5	15.38	10.42	0.68
9	IT14	5	18.13	12.08	0.67
10	IT14	3	15.51	10.62	0.68
11	IT16	3	18.59	13.02	0.70
12	IT16	3	17.41	11.79	0.68
13	IT16	5	16.02	11.05	0.69
14	IT16	5	18.89	13.07	0.69
15	IT16	3	16.16	11.30	0.70
16	IT4	3	19.09	14.57	0.76
17	IT4	3	17.89	13.52	0.76
18	IT4	5	16.46	12.24	0.74
19	IT4	5	19.40	14.76	0.76
20	IT4	3	16.60	12.63	0.76
21	IT9	3	20.04	14.44	0.72
22	IT9	3	18.78	13.16	0.70
23	IT9	5	17.27	11.76	0.68
24	IT9	5	20.36	14.06	0.69
25	IT9	3	17.43	12.46	0.71

4.2.1 Discussion of Measurements Conducted at CERF

The Rem counter dose values consistently exhibit underestimations when compared to the reference doses at the CERF facility. This section presents a series of Monte Carlo simulations performed to elucidate this behavior. Given that the response curve of the detector doesn't align perfectly with the ICRP curve (refer to Figure 3.23), and the calibration factor is determined using an Am-Be source, it becomes feasible to simulate the detector's response in a known neutron field.

A collection of simulations, employing the same assumptions as those outlined in Section 3.3.1, has been executed:

- The MSND was modeled with a 0.5 μm x 4 cm^2 ^{6}LiF active detector.
- A 25 cm diameter polyethylene-based moderator was employed, featuring cadmium and lead inserts.
- The simulations involved an isotropic neutron beam with an Am-Be source, as shown in Figure 3.21, covering spectra from the concrete side, concrete top, and iron top.
- The evaluation of detector counts was performed using the FLUKA card `DETECT`.

The spectrum adopted for simulations are shown in a lethargy plot respectively in Figures 4.5, 4.6 and 4.7. The objective is to determine the counts per primary of the MSND for each spectrum and then make comparisons with the Am-Be source. Specifically, by multiplying the ratio between the counts obtained using a specific spectrum and those from the Am-Be source, we can derive the response of the detector in the respective neutron field. The results are presented in Table 4.5.

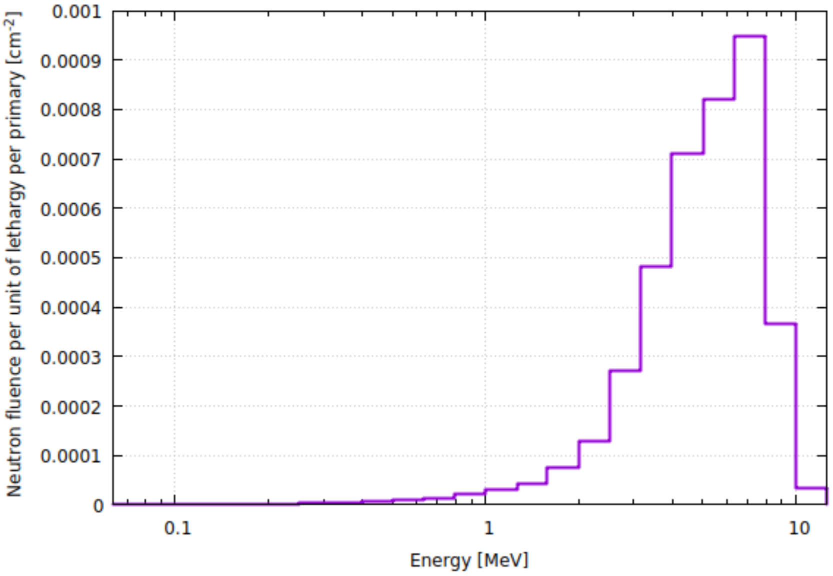

Figure 4.5: Spectrum adopted for simulations with Am-Be source.

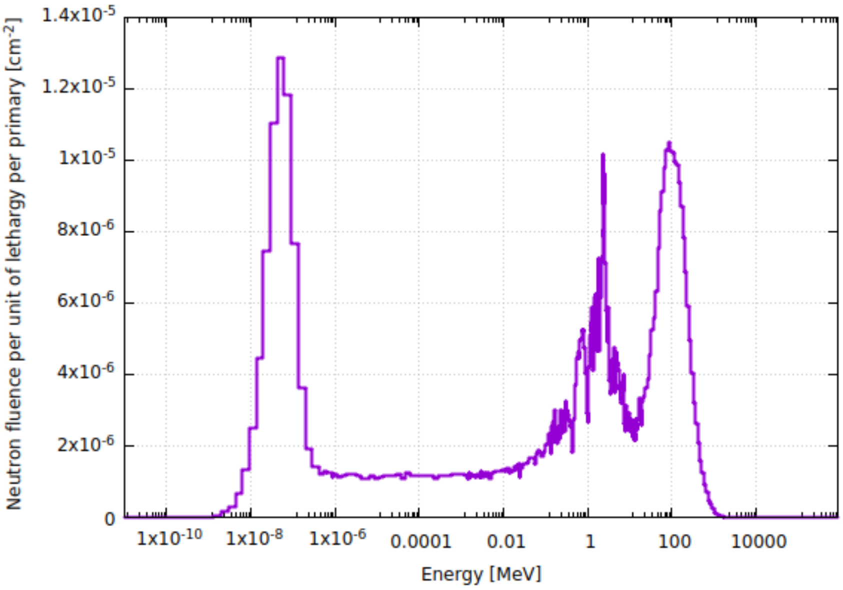

Figure 4.6: Spectrum adopted for simulations with CT and CS source.

Table 4.5: Comparison between detector response in different fields expressed with the ratio between a given spectrum and Am-Be spectrum.

Spectrum	**Counts/primary**	**Ratio**	**CERF Ratio**
Am-Be	1.77x10^{-3}	1.00	1.00
CS-CT	1.61x10^{-3}	1.10	1.15
IT	1.32x10^{-3}	1.34	1.30

Considering the uncertainties associated with the IC-Counts at the CERF facility, the geometry of the MSND detector, and the spectrum, the results demonstrate a high level of agreement. It is important to stress that this approach is not meant to replace the doses calculated by the rem counter but rather to confirm the accuracy of its estimations. Results presented in Table 4.5 confirm the reliability both of the rem counter's model implemented in FLUKA and of the detector's response as function of neutron energy shown in Figure 3.18.

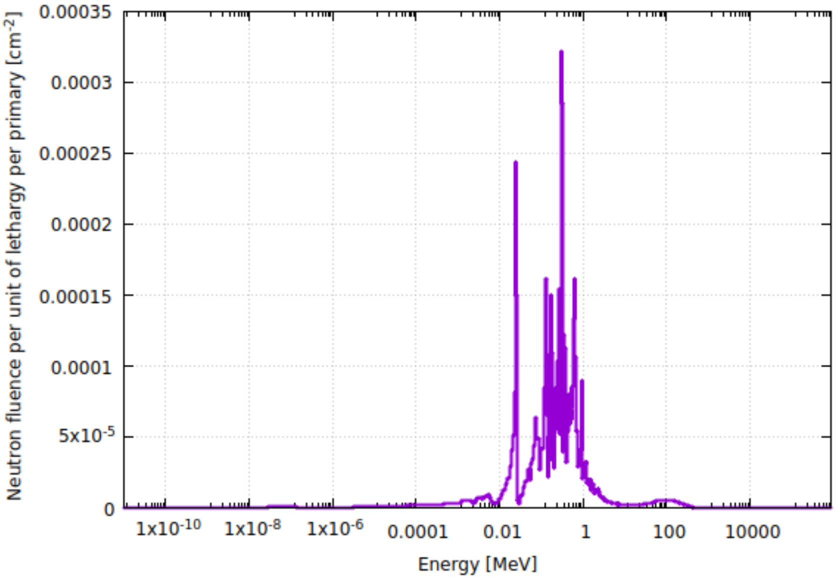

Figure 4.7: Spectrum adopted for simulations with IT source.

4.3 Measurements Performed at CNAO

This section is dedicated to measurements using the extended-range rem counter conducted within the synchrotron room at CNAO. The results of these measurements are then compared to Monte Carlo simulations incorporating the beam loss model as presented in Section 2.4.2. The first paragraph outlines the methodology employed for the Monte Carlo simulations and provides details about the experimental setup. The second paragraph delves into the results of the measurements and their subsequent discussion. The final paragraph presents the conclusions drawn from the comparisons between experimental data and Monte Carlo simulations.

4.3.1 Methodology

Geometry and Positioning

The Monte Carlo simulations were conducted using the same geometry as described in Section 2.4.1. To simulate the extended-range rem counters, four spheres with a diameter of 25 cm were incorporated. These spheres were positioned as depicted in Figure 4.8, and in the simulations, they were placed in correspondence with the actual locations of the rem counters within the synchrotron room, as illustrated in Figure 4.9. The selection of these positions was driven by specific considerations. The synchrotron room is only accessible for extraordinary maintenance or during scheduled maintenance, which occurs approximately 3 to 4 times a year. Additionally, it was essential to ensure that the detectors could be controlled remotely via wired connections. While CNAO has extended its cable network to a few locations within the synchrotron room, these conditions limited the available measurement points. Another critical factor in position selection was to

Figure 4.8: Position of spheres in the synchrotron room.

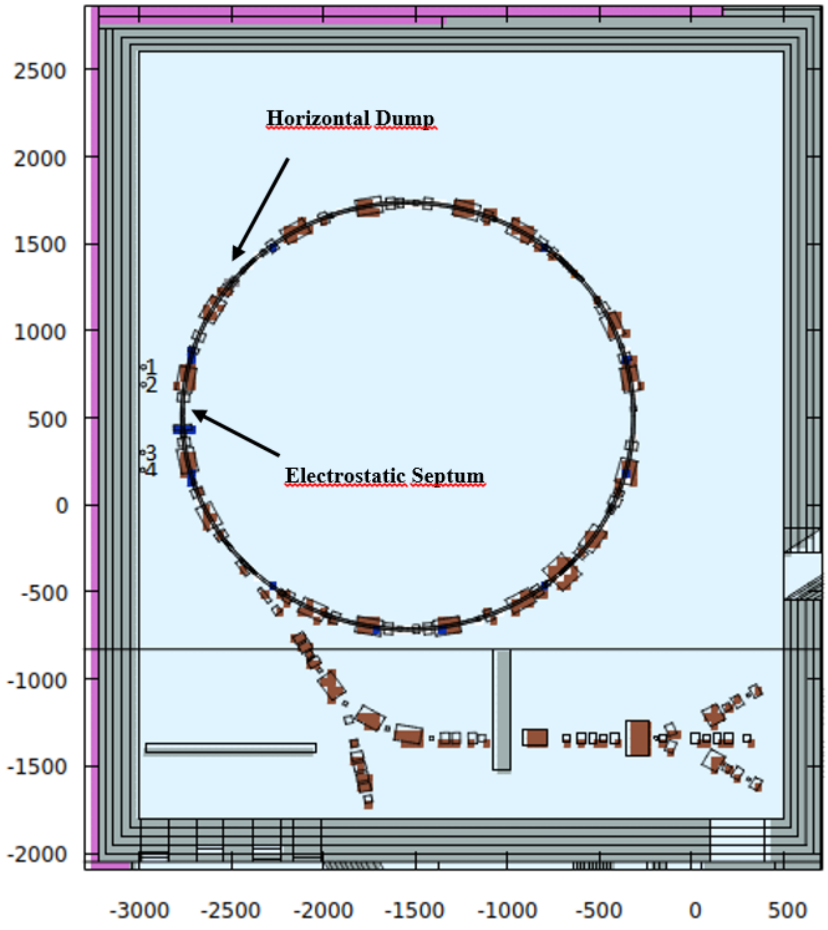

Figure 4.9: Position of spheres in the simulations inside the synchrotron room.

ensure that the chosen locations had field intensities consistent with the rem counter measurement ranges, which can reach up to 2 mSv/h. Furthermore, it was advantageous to position the detectors in proximity to a beam loss point. Specifically, the spheres were placed around 90 degrees from beam loss number 10, as indicated in Figure 2.13, and along the tangent of beam loss number 24. Beam loss number 24 represents the horizontal dump loss and is the most intense in the model, as denoted in point 24 of Table 2.17.

Beam Implementation

Another crucial aspect is the selection of the beam loss model. For these simulations, the same model as described in the routine outlined in Section 2.4.2 was used. The intensity of each beam loss point, as detailed in Table 2.18, was determined by considering the actual number of particles accelerated in the synchrotron, whether intended for medical treatments or for experimental rooms. The real workloads employed during the measurements were extracted from the CNAO History database. This tool allows users to retrieve information about the particles accelerated in the synchrotron, their energy, and their intended destinations during the selected time period. The measurements were conducted over a 32-hour period, spanning from 04/10/2023 at 9:16 to 05/10/2023 at 17:16. During this time frame, the workloads obtained from CNAO History are detailed in Table 4.6. The proton and carbon ion spectra, as depicted in Figures 4.10 and 4.11, indicate that protons were accelerated within the range of 60 to 226 MeV, while carbon ions were accelerated in the range of 120 to 400 MeV/u. Indeed, it's essential to highlight that, in contrast to the simulations conducted in Chapter 2, only a small percentage of these particles reached their maximum energy levels.

It's important to emphasize that the model was designed as a cautionary tool and developed for assessments over the course of a year of the center's activity. In contrast, the measurements were conducted over a much shorter duration, lasting 32 hours. Consequently, it's anticipated that the Monte Carlo simulations may slightly overestimate the ambient dose equivalent values due to this shorter time frame of measurement.

Table 4.6: Particles per in the selected period destined for therapy and experimental room for protons and carbon ions.

Particle	**Therapy workload** [$particles$]	**Experimental workload** [$particles$]
Protons	1.93x10^{14}	1.93x10^{11}
Carbon ions	1.85x10^{12}	2.52x10^{11}

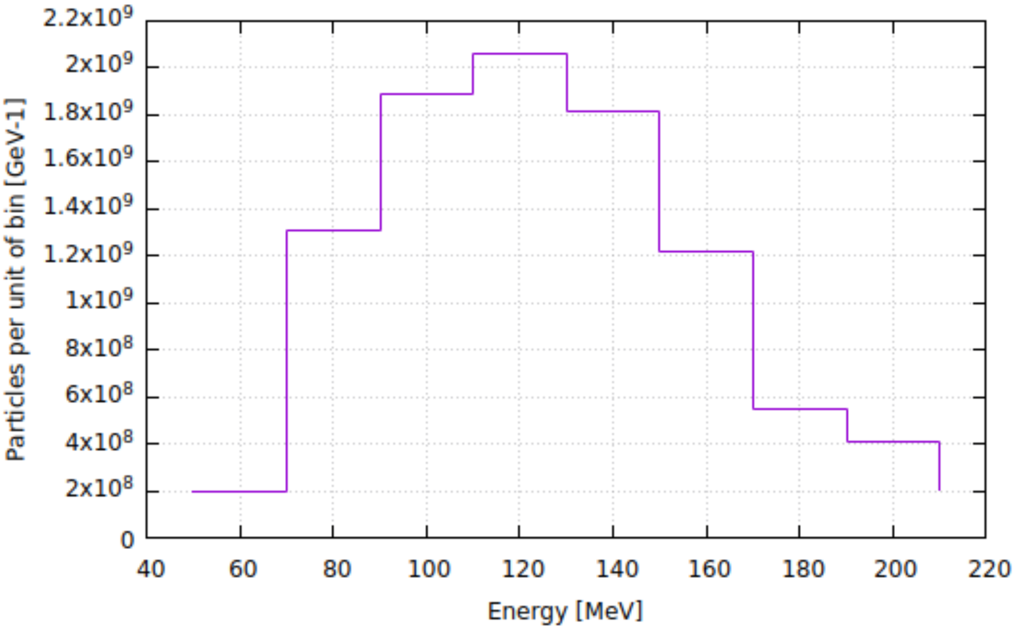

Figure 4.10: Spectrum of protons adopted for the simulations.

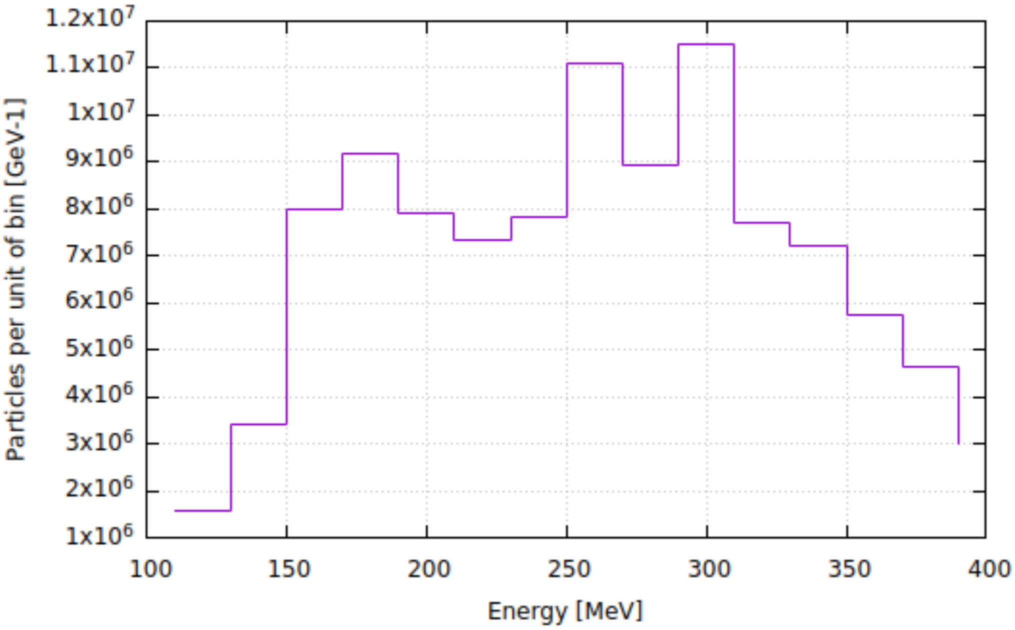

Figure 4.11: Spectrum of carbon ions adopted for the simulations.

Scoring

To estimate the ambient dose equivalent, H*(10), the Monte Carlo simulations incorporated the following scoring components:

- A dose map of the ambient dose equivalent around the spheres, as depicted in Figure 4.9.
- The neutron fluence crossing each sphere.

Given the precision of the geometry model and the close proximity of the spheres, it was determined to average the dosimetric results to obtain a single value for detector 1 and 2, and another for detector 3 and 4. This approach helps consolidate the results and provide a more robust assessment of the ambient dose equivalent.

4.3.2 Results and Discussion

This section covers the results obtained from simulations involving proton and carbon ion spectra, as depicted in Figures 4.10 and 4.11. The simulations incorporated workloads detailed in Table 4.6 and were based on the beam loss model outlined in Section 2.4.2. The measurements were carried out between 04/10/2023 at 9:16 and 05/10/2023 at 17:16.

Figure 4.12 displays the ambient dose equivalent map for irradiation with carbon ion beams. Notably, the primary beam loss points in the area of interest are the horizontal dump and the electrostatic septum. For the assessment of the dose received by the rem counters, a denser dose grid was positioned around the detectors, as illustrated in Figures 4.13 and 4.14. These figures provide dose maps for protons and carbon ions, allowing for a qualitative evaluation. It's apparent that the H*(10) values are comparable for the selected proton and carbon ion workloads. Furthermore, Figures 4.15 and 4.16 depict the dose profiles corresponding to the spheres for protons and carbon ions, respectively. The X-axis aligns with the Y-axis in Figure4.9. To quantitatively evaluate the dose, the mean value of the dose profile curves (Figures 4.15 and 4.16) was computed within the range of 200 cm to 300 cm for positions 1 and 2, and 700 cm to 800 cm for positions 3 and 4.

The counts obtained with the rem counters, along with their corresponding doses, are documented in Table 4.7. It's worth noting that the calibration factor utilized for these measurements is 1.25 nSv/counts.

Table 4.7: Comparison between values obtained with the rem counter and Monte Carlo simulation.

Position	*Counts*	**H*(10) [mSv] MSND**	**H*(10) [mSv] FLUKA**	**Ratio**
1-2	1.40x10^6 ± 1%	1.98 ± 6%	2.08 ± 2%	1.05
3-4	1.60x10^6 ± 1%	1.74 ± 6%	3.50 ± 2%	2.01

The results presented in Table 4.7 indicate a strong agreement for positions 1-2 and a notable underestimation for positions 3-4. However, several key considerations should be highlighted:

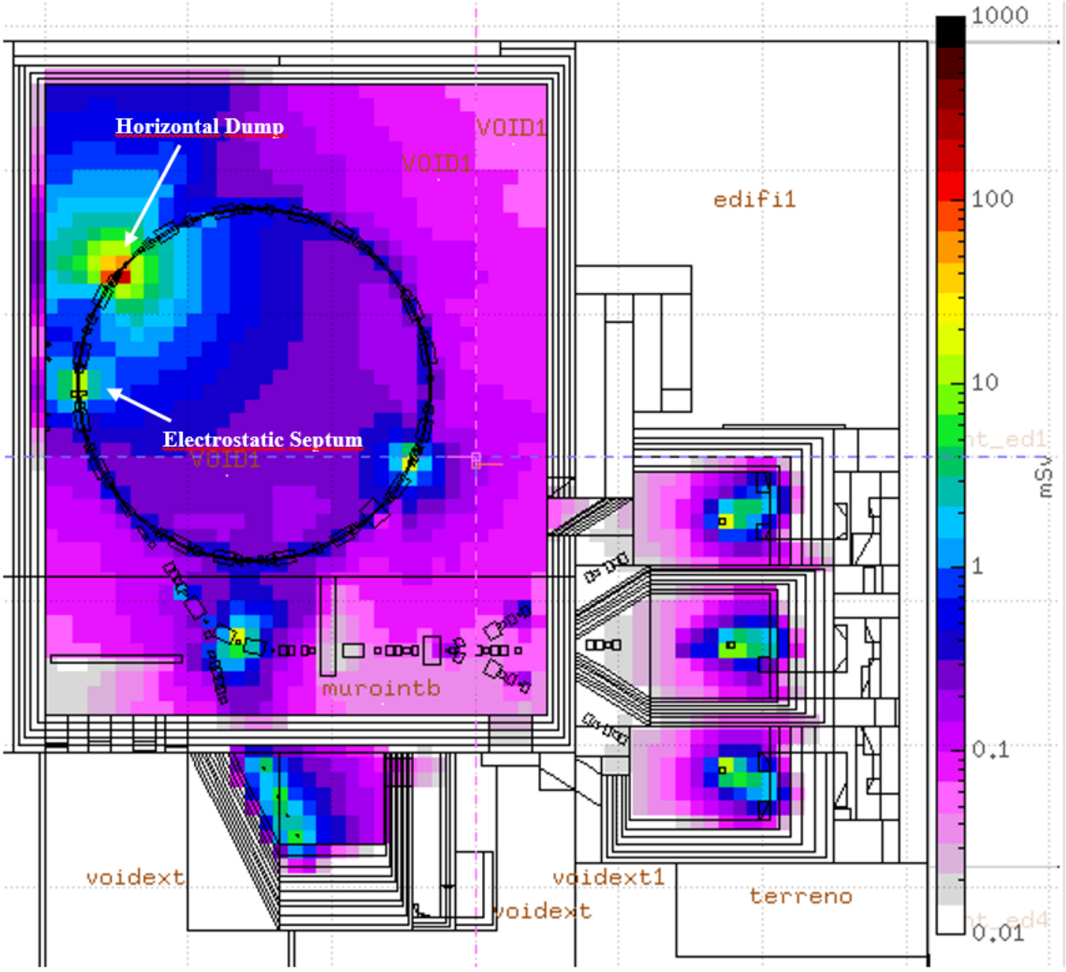

Figure 4.12: Dose map in the region of interest with the proton beam. The scale shows ambient dose equivalent values in mSv.

- The model is designed for radiation protection and is intentionally cautious, typically resulting in an overestimation of real beam losses and related doses.

- The model is considered reliable for year-long evaluations but may not be as accurate for short-term periods.

- The selected measurement points are located in close proximity to areas of beam loss, and slight adjustments in positioning can lead to substantial variations in the received dose. For this reason, a study conducted as described in Section 4.2.1 can potentially lead to misinterpretation. Notably, the neutron spectrum with both proton and carbon ion beams can undergo substantial changes, even within a few centimeters, as demonstrated in Figures 4.17 and 4.18.

Considering the factors mentioned, the results can be viewed in a positive light. The rem counters do not reach saturation levels inside the synchrotron room, and the dose

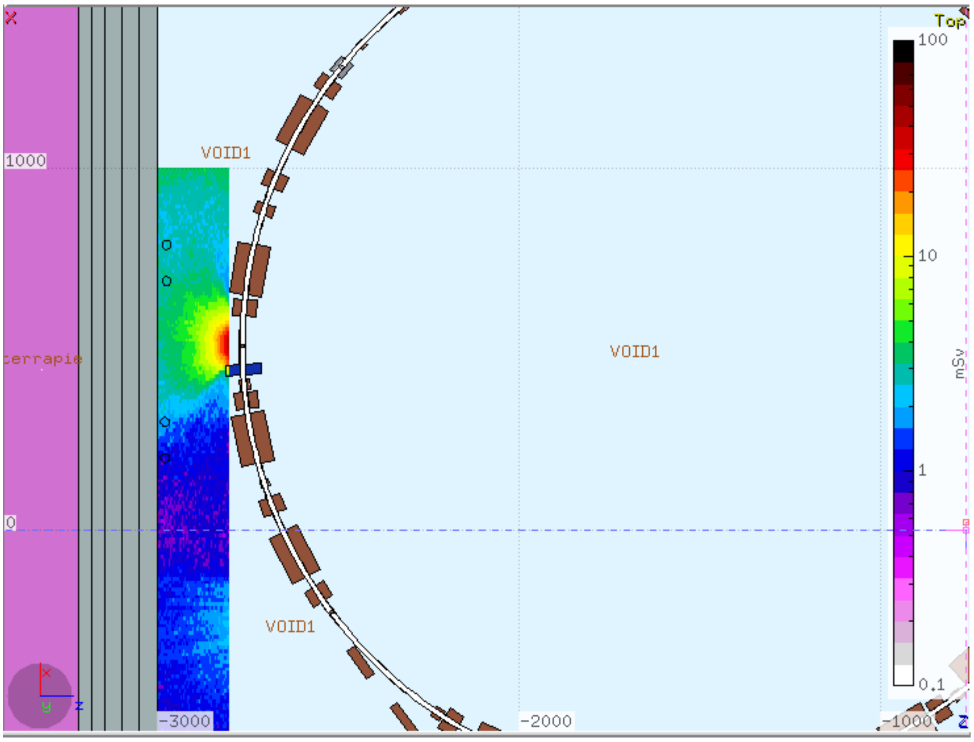

Figure 4.13: Detail of dose map in the region of interest with the proton beam. The scale shows ambient dose equivalent values in mSv.

assessments are reliable. The detectors are suitable for monitoring beam losses and assessing the percentage of beam losses. In the future, longer-duration measurements with a greater number of measurement points are planned to further validate the beam loss model's accuracy.

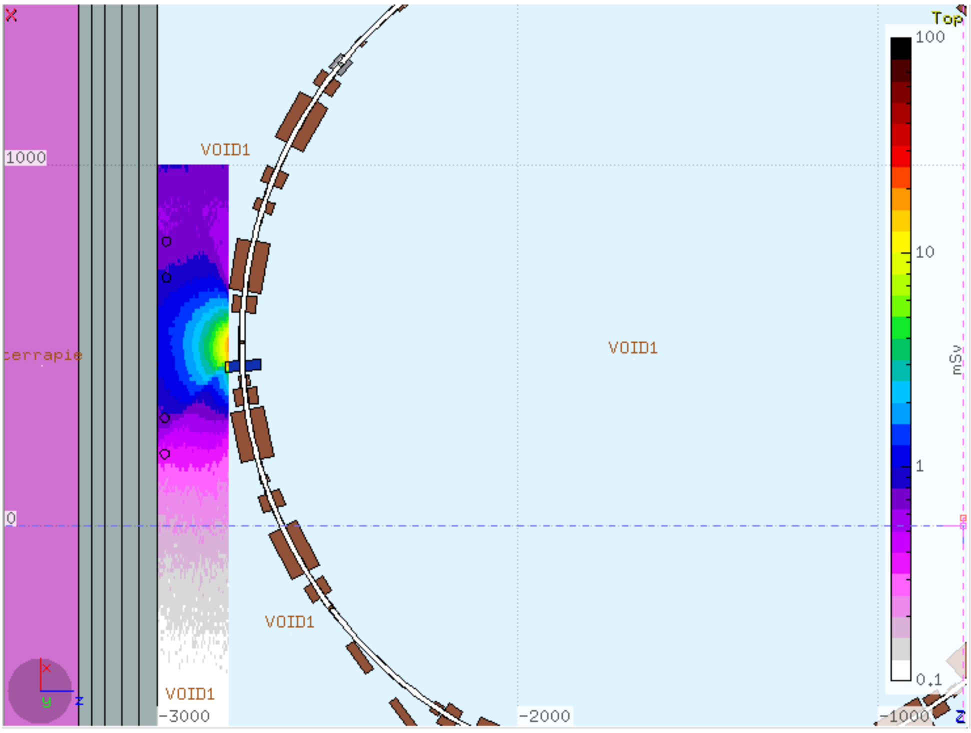

Figure 4.14: Detail of dose map in the region of interest with the carbon ion beam. The scale shows ambient dose equivalent values in mSv.

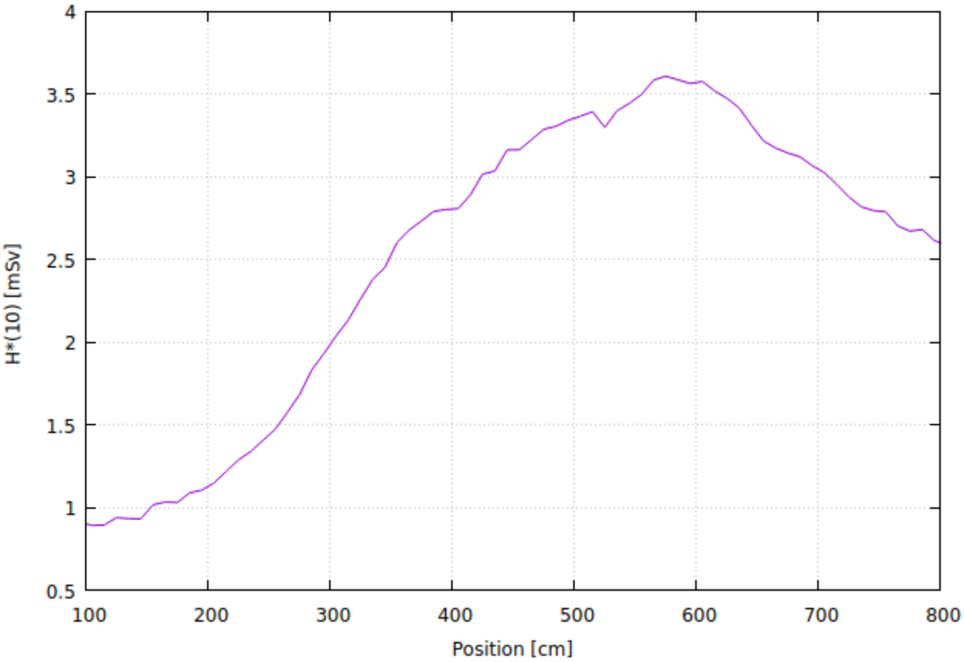

Figure 4.15: Dose profile obtained with the proton beam. X-axis is in correspondence with the Y-axis in Figure 4.9.

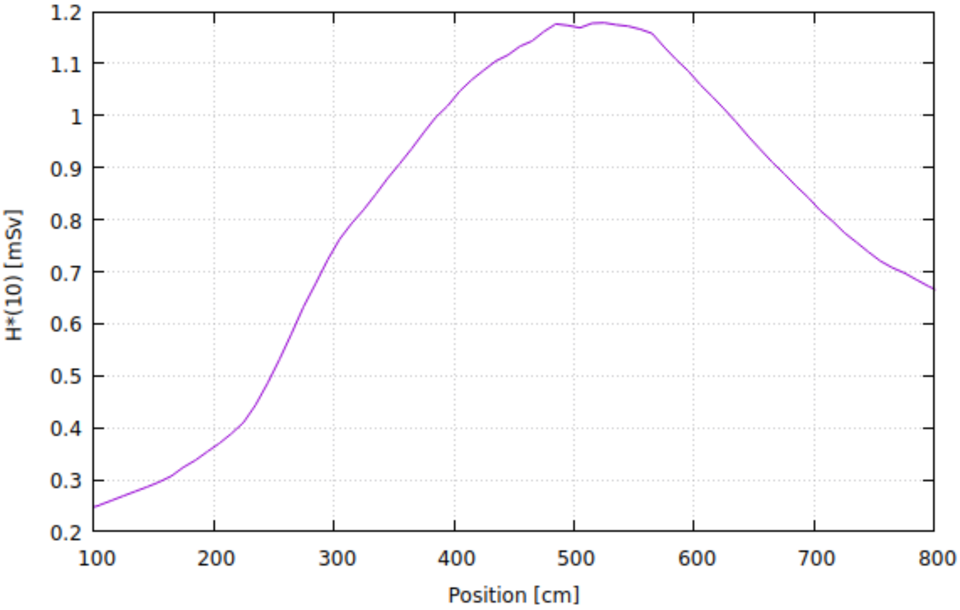

Figure 4.16: Dose profile obtained with the carbon ion beam. X-axis is in correspondence with the Y-axis in Figure 4.9.

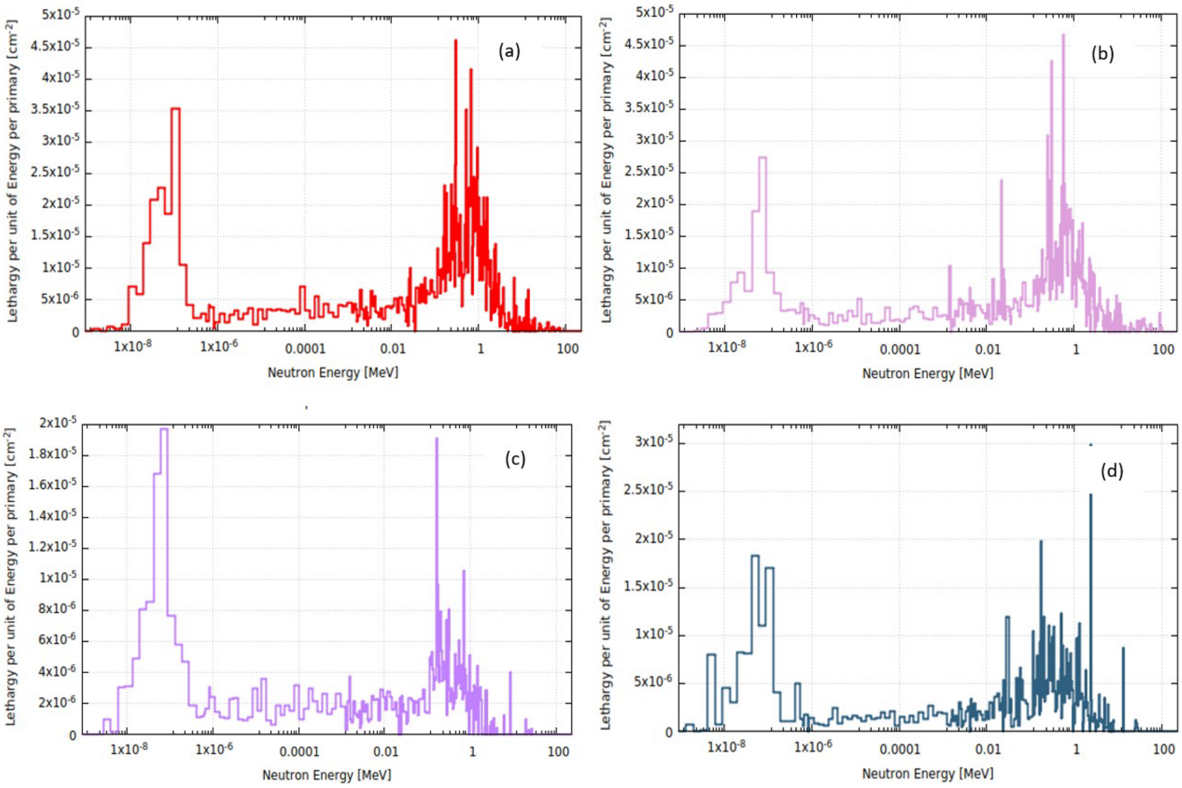

Figure 4.17: Neutron spectrum (a), (b), (c), (d) respectively in positions 1, 2, 3, 4 shown in Figure 4.9 with the proton beam.

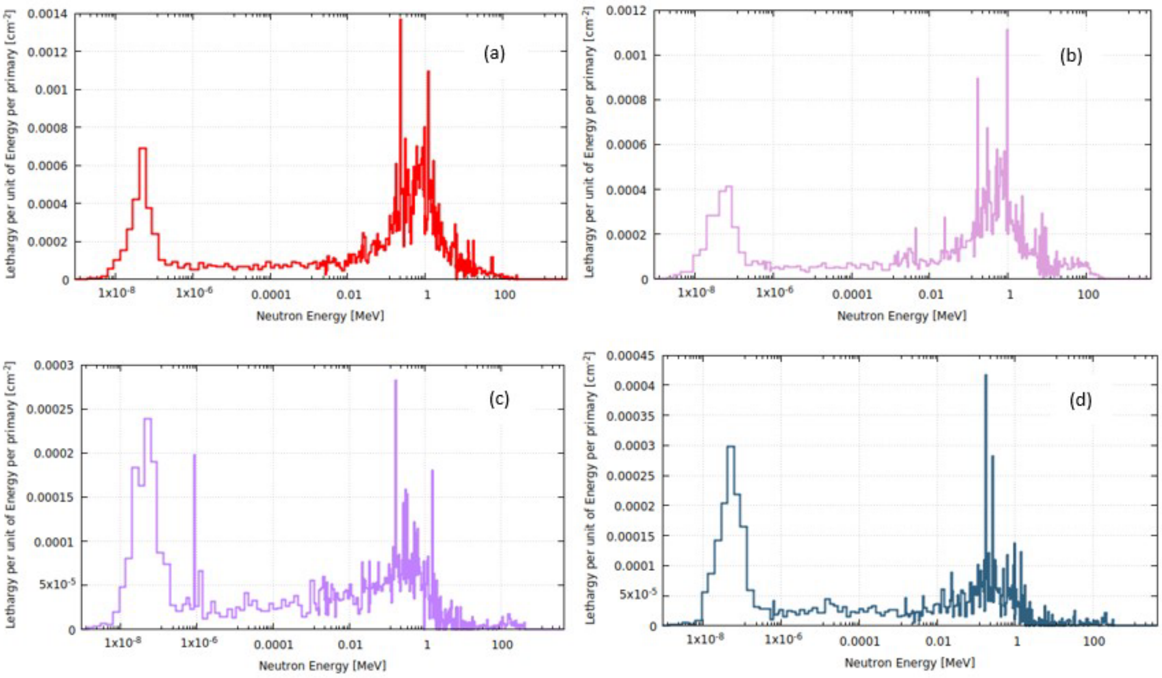

Figure 4.18: Neutron spectrum (a), (b), (c), (d) respectively in positions 1, 2, 3, 4 shown in Figure 4.9 with the carbon ion beam.

5 | Conclusions and Future Developments

This thesis has been carried out in the framework of the CNAO expansion project that involves a new proton synchrotron with a rotating gantry and a BNCT facility. Furthermore, the current synchrotron installed that already accelerates protons and carbon ions will be upgraded in order to accelerate also helium, lithium, oxygen and iron ions. The current Italian radiation protection regulation [5] requires assessments on the maximal current at which the new ion species can be accelerated.

The second chapter of this thesis is dedicated to this topic. The study is conducted with the Monte Carlo line of sight model available in literature, that is usually adopted for shielding problems. In this thesis the model has been adapted for the specific case introducing the carbon ratio. This ratio is calculated dividing the ambient dose equivalent obtained with a selected ion in a given shielding position by the dose evaluated with carbon ions. The results enlarge the literature data available for these models, in particular, introducing the attenuation curves for iron ions at 306 MeV/u. Furthermore, the carbon ratio can be also adopted for a first evaluation of ion currents in other hadron therapy centers that already accelerate carbon ions. The final evaluation of currents have been conducted with Monte Carlo simulations with the implementation of the complete CNAO geometry in FLUKA. In this thesis, the geometry and the beam loss model has been refined. Maximum currents for selected ions were calculated multiplying the ratio between the dose provided by a given ion and carbon ions at 400 MeV/u by the maximum current allowed for carbon ions. Table 5.1 shows an hypothesis of currents that can be accelerated in CNAO taking into account also clinical and experimental requests. The reported values are evaluated considering ∼400 dose points both inside CNAO boudaries with values higher than 10 μSv/year and points outside the CNAO boundaries.

Chapter three describes both the computational and experimental studies conducted for the characterization of a rem counter. The detector is based on a Micro Structured Neutron Detector (MSND) with a polyethylene based moderator with cadmium and lead inserts. The entire system is then connected to a Raspberry Pi through GPiO pins to control it remotely. A first experiment was set to verify the performances between the MSND and the Raspberry Pi connection with multiple counting programmes. In particular, the final code implemented is composed by a visualization script written in Python and a counting script written in C that was able to manage square signal up to

Table 5.1: Values of ions/year evaluated in this thesis.

Ion	**Beam Energy [MeV/u]**	**ions/year**
^{4}He	250	$3.15 \text{x} 10^{16}$
^{7}Li	306	$1.05 \text{x} 10^{16}$
^{12}C	400	$1.26 \text{x} 10^{16}$
^{16}O	400	$1.68 \text{x} 10^{15}$
^{56}Fe	306	$8.4 \text{x} 10^{14}$

90 kHz, over the requirements of the MSND (66 kHz). Then the rem counter has been modelled in FLUKA in order to calculate the response curve of the detector, that shows the counts·cm^2 as function of 54 neutron energies from 10 meV to 1 GeV.Results show a high level of agreement with literature data on other rem counters. During the experimental campaign conducted at the Czech Metrology Center (CMI) a calibration factor of 1.25 ± 0.06 nSv/count has been estimated with an Am-Be source and the linearity test shows a saturation dose rate of 2 mSv/h. Tests suggest the possibility to adopt the rem counter also for beam loss monitor applications.

Finally, the detector was tested at Cern calibration room, at Cerf facility and in CNAO synchrotron room. All tests show a great reliability of the rem counter even in high rate mixed fields. In particular, the measurements at calibration room with a Am-Be source confirm the calibration factor calculated at CMI and experiments conducted at Cerf and at CNAO show a slightly underestimation of dose estimated by the detector in high energy neutron fields. This behaviour is common for rem counters since they are usually calibrated with Am-Be or ^{252}Cf sources peaked around 1-10 MeV. In fact, the Cerf and CNAO spectrum ranges from thermal to high energy neutrons up to hundreds of MeV that can cause this underestimation. This trend has been confirmed with Monte Carlo simulations where the ratio between the rem counter response with Am-Be and Cerf neutron spectrum has been calculated.

Since the good results of the experimental campaigns at Cerf and CNAO in mixed high rate fields, it is under evaluation the possibility to adopt the rem counter both for ambient dose evaluation and for beam loss monitoring at CNAO. The idea is to develop a network infrastructure dedicated to a set of these detectors for the online dose monitoring of the center. In particular, this application can also improve the beam loss model adopted in this thesis in order to improve future ambient dose evaluations needed for the radiological impact of the center.

A | Field and Dosimetric Quantities

In the first part of this chapter the main field quantities adopted in the thesis are defined. In the following sections the nuclear interactions at hadrontherapy energies, the rem counters and the Monte Carlo code Fluka are introduced. In this section the main definitions for radiation field, dosimetric and radiation protection quantities adopted in the thesis are introduced.

A.1 Radiation Field Quantities

Radiation field quantities are defined to describe the radiation field propagation in the space.

Fluence

Particle fluence is a radiation field quantity adopted to evaluate the number of particles in a certain point R in the space and can be calculated through the formula:

$$\Phi = \frac{dN}{da} \tag{A.1}$$

with dN the number of particles incident on a sphere centered in R with a cross-sectional area da. Its unit is $[m^{-2}]$. Fluence is independent from energy and from the radiation field orientation. In order to take into account of these variables some differential quantities can be defined. The differential spectra, Φ_E, can be expressed as:

$$\Phi = \frac{dN}{da\ dE} \tag{A.2}$$

and its measured in $[m^{-2} \cdot J^{-1}]$.

In Monte Carlo codes, often, a double differential fluence (angle and energy) is evaluated, defined as:

$$\frac{d\Phi_E}{d\Omega} = \frac{d\Phi(E)}{dE\ d\Omega} \tag{A.3}$$

and its unit is $[m^{-2} \cdot J^{-1} \cdot sr^{-1}]$.

Flux

The flux is the defined as:

$$\phi = \frac{d\Phi}{dt} \tag{A.4}$$

and its unit is $[m^{-2} \cdot s^{-1}]$. This quantity is adopted in nuclear reactors to take into account the variation of neutron fluences in the reactor core.

A.2 Dosimetric Quantities

Dosimetric quantities describe the energy transfer from ionizing radiation interaction with matter. The main quantities are the imparted energy and the absorbed dose.

Energy Imparted

The imparted energy, ϵ, is defined as:

$$\epsilon = R_{in} - R_{out} + \Sigma Q \tag{A.5}$$

where R_{in} is the energy of the radiation field that enters the volume considered, R_{out} is the energy emerging from the volume and ΣQ is the sum of all energies released during the interactions. R_{in} and R_{out} take into account the energies of directly and indirectly ionizing radiation. The imparted energy is a stochastic quantity measured in $[J]$. Since its nature, it is useful to introduce the mean value of the imparted energy $\bar{\epsilon}$.

Absorbed Dose

The absorbed dose is a stochastic quantity that described the mean energy imparted in a volume of mass, dm, through the formula:

$$D = \frac{d\bar{\epsilon}}{dm} \tag{A.6}$$

its unit is $[J \cdot kg^{-1}]$ or $[Gy]$. The absorbed dose is a physical quantity, that can be measured, but that cannot be related to biological effects of ionizing radiation. In fact, it doesn't take into account the interactions that generate that dose.

A.3 Radiation Protection Quantities

Equivalent dose and effective dose are defined to describe the deterministic and stochastic effects of ionizing radiation on the human body. Deterministic effects has a threshold dose to appear and their severity increase linearly with the dose. Stochastic effects are independent of the dose value and their probability increases as the dose absorption.

Furthermore, the dose limits for population and workers in the current regulation [5] are expressed as equivalent dose and effective dose values. In order to evaluate these doses the operational quantities are adopted. The most widely used is the ambient dose equivalent that is introduced at the end of the paragraph.

Equivalent Dose

The equivalent dose, H_T is defined as [67]:

$$H_T = \sum_R w_R \cdot D_{T,R} \tag{A.7}$$

where w_R is the radiation weighting factor, that depends of the radiation type R, and $D_{T,R}$ is the absorbed dose by the tissue T. Even if, w_R is dimensionless the unit changes from $[Gy]$ to $[Sv]$ to stress that the radiation protection quantities are not physical quantities. In fact, a better knowledge of radiation effects can change the w_R values. In Figure A.1 and in Figure A.2 are reported the values of w_R for each radiation type.

Radiation type	**Radiation weighting factor, w_R**
Photons	1
Electrons and muons	1
Protons and charged pions	2
Alpha particles, fission fragments, heavy ions	20
Neutrons	A continuous function of neutron energy (see Fig 1.1)

Figure A.1: Radiation weighting factors for each radiation type.

Effective Dose

The effective dose, E, is the sum of the equivalent doses evaluated for each tissue or organ of the human body, T:

$$E = \sum_T w_T \cdot H_T = \sum_T w_T \sum_R w_R \cdot D_{T,R} \tag{A.8}$$

with E expressed in $[Sv]$, w_T the weighting factor for the tissue or organ T and H_T the equivalent dose absorbed by the tissue or organ T. In Figure A.3 the weighting factors for the main tissue and organs are reported.

Ambient Dose Equivalent

The ambient dose equivalent, $H^*(10)$, is a operational quantity adopted to estimate the effective dose defined as [67]: the dose equivalent at a point in a radiation field that would be produced by the corresponding expanded and aligned field in the ICRU sphere at a

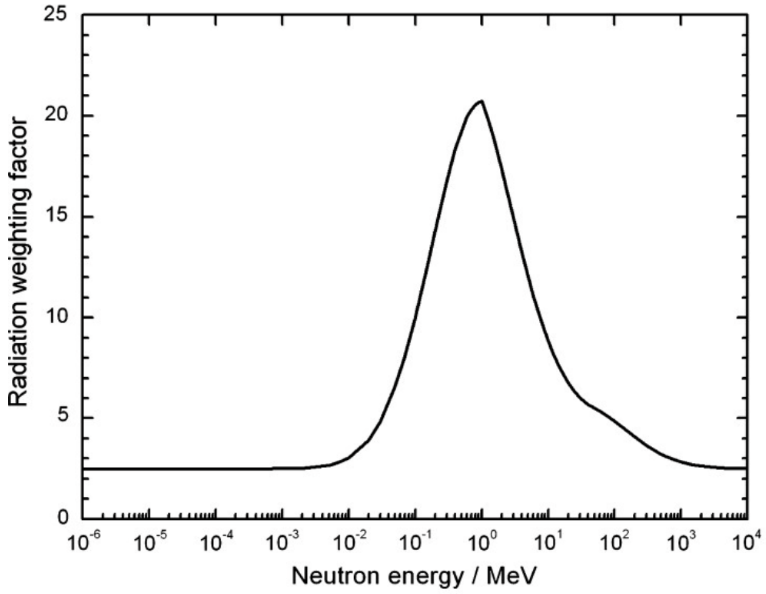

Figure A.2: Radiation weighting factors function for neutrons.

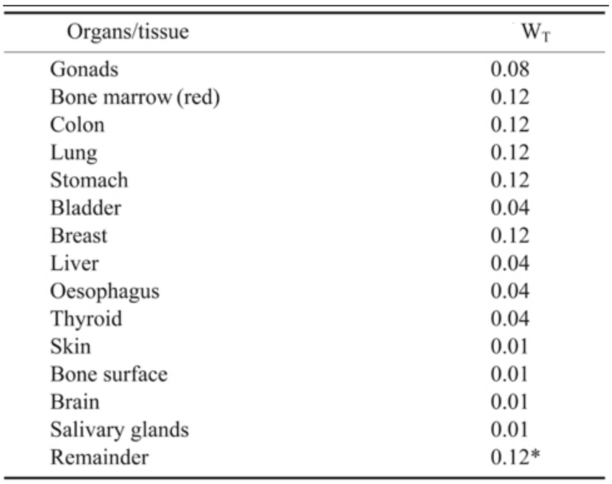

Organs/tissue	W_T
Gonads	0.08
Bone marrow (red)	0.12
Colon	0.12
Lung	0.12
Stomach	0.12
Bladder	0.04
Breast	0.12
Liver	0.04
Oesophagus	0.04
Thyroid	0.04
Skin	0.01
Bone surface	0.01
Brain	0.01
Salivary glands	0.01
Remainder	0.12*

Figure A.3: Tissue weighting factors for irradiated tissue or organ.

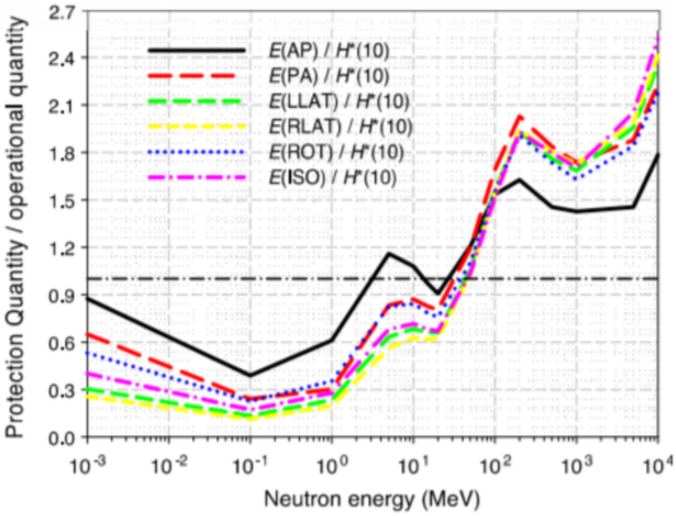

Figure A.4: Ratio between $H^*(10)$ and the effective dose E with different irradiation.

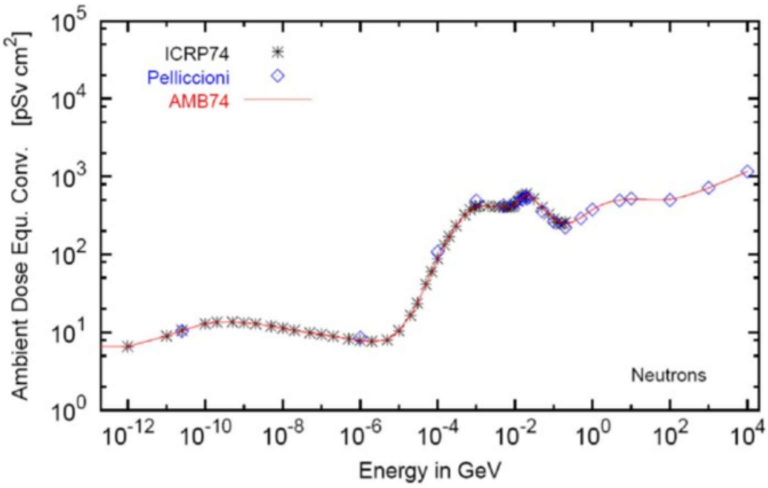

Figure A.5: Conversion coefficient from fluence to ambient dose equivalent values for neutrons [58].

depth of 10 mm on the radius vector opposing the direction of the aligned field. It's unit is the $[Sv]$. The ICRU sphere is a sphere with a diameter of 30 cm made of 4-elements ICRU tissue (density:1 g/cm^3, mass composition: 76.2% oxygen, 11.1% carbon, 10.1% hydrogen and 2.6% nitrogen).

The ambient dose equivalent is a good estimator of the effective dose and in most cases overestimate it. In Figure A.4 the ratio between $H^*(10)$ and the effective dose E with different irradiation is reported. For neutron with energies over 10 MeV the ambient dose equivalent underestimates the value of E. Monte Carlo codes often adopt conversion coefficients from fluences to ambient dose equivalent values. In Figure 3.2 the ratios for neutron are reported.

B | Visualization and Counting Codes

B.1 Python Visualization Code

In this section are reported screenshots of the python code adopted for the counting interface (Figure B.1) on the Raspberry Pi.

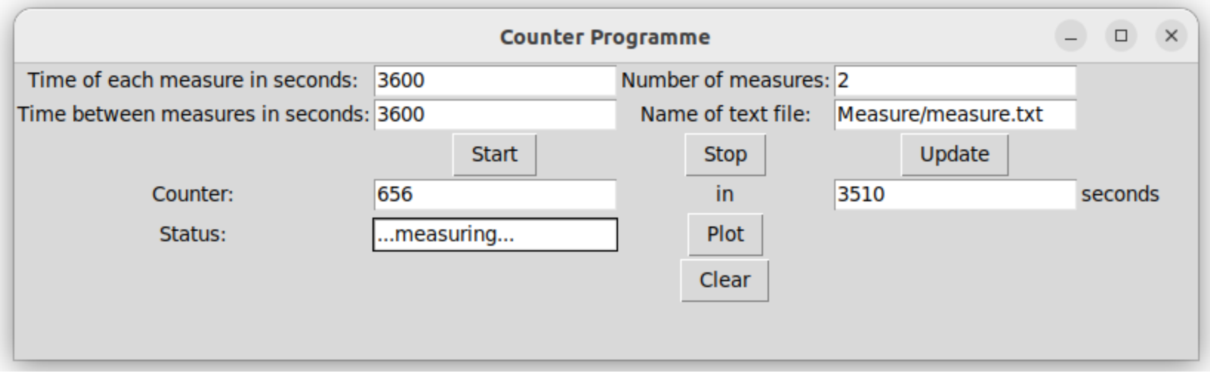

Counter Programme

Time of each measure in seconds: 3600

Number of measures: 2

Time between measures in seconds: 3600

Name of text file: Measure/measure.txt

Counter: 656 in 3510 seconds

Status: ...measuring...

Figure B.1: View of the counting interface written with the python interface Tkinter.

The code can be divided into sections shown in Figures B.2 to B.8, in particular:

- Figure B.2 shows the import of libraries and modules needed for the code and dimension of the dialog window of the program;
- Figure B.3 shows the functioning of the Start button through the Start() function;
- Figure B.4 shows the functioning of the Stop and Update buttons through Stop() and Update() functions;
- Figures B.5 and B.6 show the functioning of the Plot button through the Plot() function;
- Figure B.7 shows the functioning of Clear button through the clear_screen() function;
- Figure B.8 shows defines widgets positions and infinite loop function;

```
#!/usr/bin/env python3

##############IMPORTS#################################################

import time
import os

import pandas as pd

from tkinter import *

import matplotlib.pyplot as plt
import numpy as np

#############INPUTS#####################################################

root = Tk()
root.geometry("800x200")

```

Figure B.2: Libraries and modules imported in the code.

```
#############START FUNCTION#########################################

def Start():
    global counter
    global final_time
    global t
    global meas_time
    global step
    global cooling
    global fl_text

    meas_time = int(input_time.get())
    step = int(input_step.get())
    cooling = int(input_cooling.get())
    fl_text = str(input_filename.get())
    final_counter.delete(0, END)
    time_s.delete(0, END)
    status_view.delete(0, END)
    status_view.insert(0,"...total time %d seconds..." \
        %(meas_time * step + cooling * (step-1)))
    t = time.time()
    meas_time_text = str(meas_time)
    step_time_text = str(step)
    cooling_time_text = str(cooling)
    os.system("sudo killall pigpiod")
    os.system('lxterminal -e sudo ./c_program' + ' ' + \
        meas_time_text + ' ' + step_time_text + ' ' + \
        cooling_time_text + ' ' + fl_text + '&')
    status_view.delete(0, END)
    status_view.insert(0,"...measuring...")
    meas_time_text = '0'
    step_time_text = '0'

```

Figure B.3: Start button function.

```
##############STOP FUNCTION##########################################

def Stop():
    final_counter.delete(0, END)
    with open(fl_text,'r') as f:
        last_line = f.readlines()[-1]
    last_line = last_line.split(',')
    counterr = last_line[2]
    final_counter.insert(0,counterr)
    os.system("sudo pkill c_program")
    status_view.delete(0, END)
    status_view.insert(0,"...measure stopped...")

##############UPDATE FUNCTION##########################################

def Update():
    final_counter.delete(0, END)
    t1 = time.time() - t
    t_update = round(t1)
    if (t_update > meas_time*step):
        time_s.delete(0, END)
        time_s.insert(0,meas_time*step)
        t_update = meas_time*step
    else:
        time_s.delete(0, END)
        time_s.insert(0,t_update)
    with open(fl_text,'r') as f:
        last_line = f.readlines()[-1]
    last_line = last_line.split(',')
    counterr = last_line[2]
    final_counter.insert(0,counterr)
```

Figure B.4: Stop and update button functions.

```
###############################PLOT################################

def Plot():
    plt.clf()
    df = pd.DataFrame()
    date = []
    times = []
    counter = []
    measure = []
    seconds = []
    number_meas = []
    table = []
    rif = 0;
    filepath = fl_text
    with open(filepath) as fp:
         for item in fp:
            count = item.split()
            if (len(count)==1):
                table.append(count)
                rif = rif + 1;
            else:
                    date.append(count[0])
                    times.append(count[2])
                    counter.append(int(count[4]))
                    number_meas.append(int(count[6]))
                    measure.append(int(rif))
    old_counter = 0
    df['Date'] = date
    df['Time'] = times
    df['Counts'] = counter
    df['Measure'] = measure
    df['MNumber'] = number_meas

    print(df.to_string())

```

Figure B.5: First part of Plot button function.

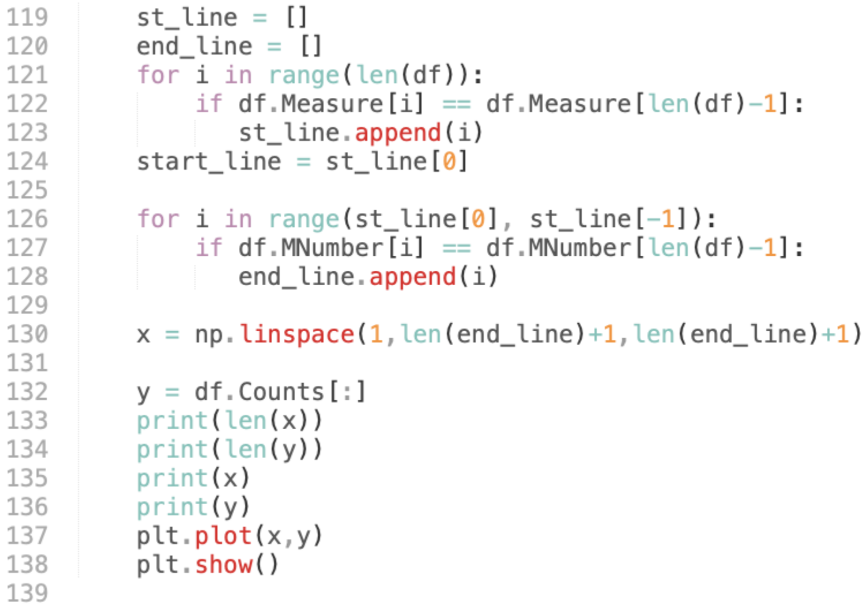

```
    st_line = []
    end_line = []
    for i in range(len(df)):
        if df.Measure[i] == df.Measure[len(df)-1]:
            st_line.append(i)
    start_line = st_line[0]

    for i in range(st_line[0], st_line[-1]):
        if df.MNumber[i] == df.MNumber[len(df)-1]:
            end_line.append(i)

    x = np.linspace(1,len(end_line)+1,len(end_line)+1)

    y = df.Counts[:]
    print(len(x))
    print(len(y))
    print(x)
    print(y)
    plt.plot(x,y)
    plt.show()
```

Figure B.6: Second part of Plot button function.

```
################CLEAR SCREEN##############################################

def clear_screen():
    input_time.delete(0, END)
    input_step.delete(0, END)
    input_cooling.delete(0, END)
    input_filename.delete(0, END)
    final_counter.delete(0, END)
    time_s.delete(0, END)
    status_view.delete(0, END)

################WIDGETS###################################################

root.title("Counter Programme")
input_time = Entry(root)
input_step = Entry(root)
input_cooling = Entry(root)
counter = Label(root, text="Time of each measure in seconds:")
step = Label(root, text="Number of measures:")
cooling_time = Label(root, text="Time between measures in seconds:")
result = Label(root, text="Counter:")
file_name = Label(root, text="Name of text file:")
input_filename = Entry(root)
inn = Label(root, text="in")
final_counter = Entry(root)
time_s = Entry(root)
seconds = Label(root, text="seconds")
plot = Button(root, text= "Plot", command = Plot)
clear = Button(root, text= "Clear", command = clear_screen)
start = Button(root, text= "Start", command = Start)
stop = Button(root, text= "Stop", command = Stop)
update = Button(root, text= "Update", command = Update)
status = Label(root, text="Status:")
status_view = Entry(root)

```

Figure B.7: Clear button function and definition of widgets.

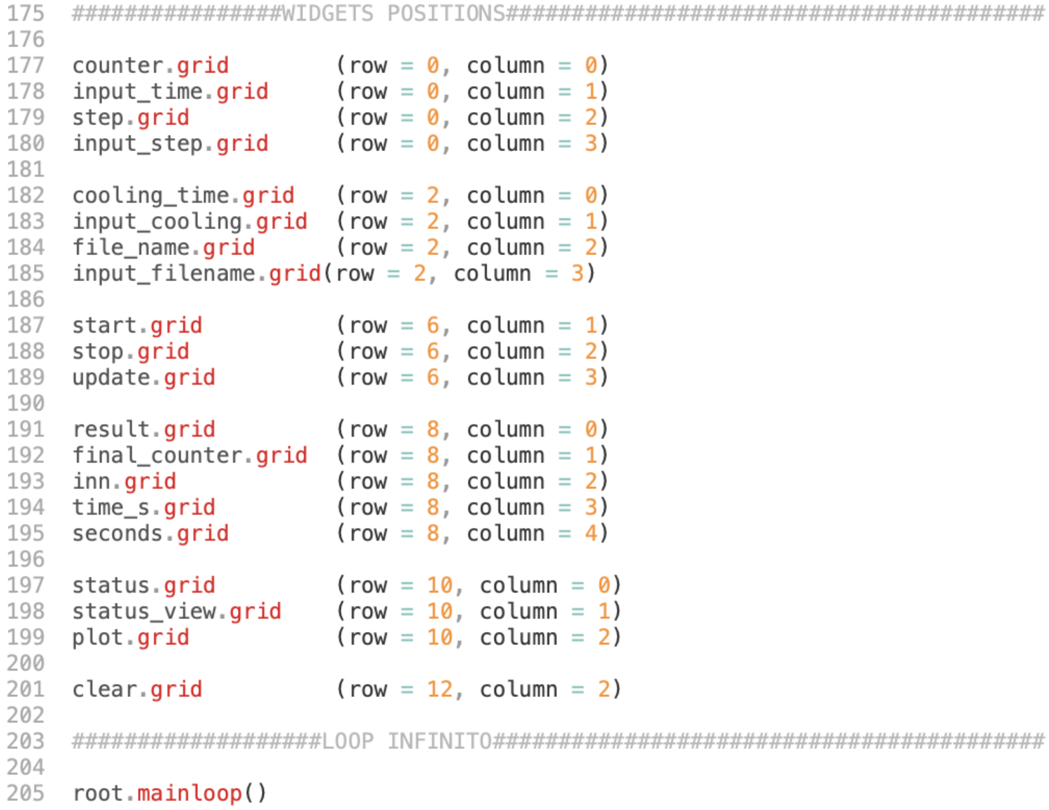

```
###############WIDGETS POSITIONS########################################

counter.grid        (row = 0, column = 0)
input_time.grid     (row = 0, column = 1)
step.grid           (row = 0, column = 2)
input_step.grid     (row = 0, column = 3)

cooling_time.grid   (row = 2, column = 0)
input_cooling.grid  (row = 2, column = 1)
file_name.grid      (row = 2, column = 2)
input_filename.grid(row = 2, column = 3)

start.grid          (row = 6, column = 1)
stop.grid           (row = 6, column = 2)
update.grid         (row = 6, column = 3)

result.grid         (row = 8, column = 0)
final_counter.grid  (row = 8, column = 1)
inn.grid            (row = 8, column = 2)
time_s.grid         (row = 8, column = 3)
seconds.grid        (row = 8, column = 4)

status.grid         (row = 10, column = 0)
status_view.grid    (row = 10, column = 1)
plot.grid           (row = 10, column = 2)

clear.grid          (row = 12, column = 2)

###################LOOP INFINITO##########################################

root.mainloop()
```

Figure B.8: Definition of widgets positions and infinite loop function.

B.2 C Counting Code

In this section are reported screenshots of the C code adopted for the counting program on the Raspberry Pi. The code communicates directly with GPiO pins with the PIGPIO library.

The code can be divided into sections shown in Figures B.9 to B.12, in particular:

- Figure B.9 shows variables declared in the code and the import of libraries and modules needed;
- Figure B.10 shows the function that writes the text file each second;
- Figure B.11 shows the first part of the main with the import of parameters from the python code, the initialization of variables and the GPiO setup;
- Figure B.12 shows the second part of the main with the counting cycle;

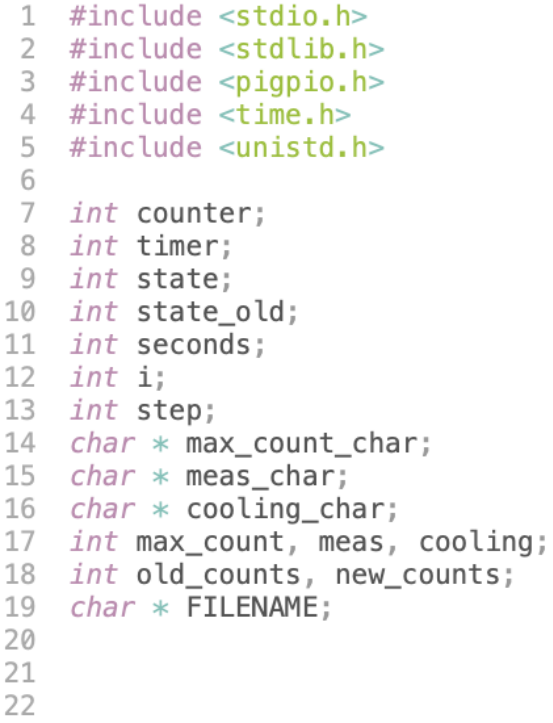

```c
#include <stdio.h>
#include <stdlib.h>
#include <pigpio.h>
#include <time.h>
#include <unistd.h>

int counter;
int timer;
int state;
int state_old;
int seconds;
int i;
int step;
char * max_count_char;
char * meas_char;
char * cooling_char;
int max_count, meas, cooling;
int old_counts, new_counts;
char * FILENAME;



```

Figure B.9: Libraries and modules imported in the code and declaration of the variables.

```c
//----------FUNCTION THAT PRINTS DATE,--------------//
//-------------DAY, COUNTER, STEP-------------------//
void timer_print_save(void)
{

    step = i + 1;
    time_t t;
        t = time(NULL);
        struct tm tm;
        tm = *localtime(&t);
    FILE *fp;
    fp = fopen(FILENAME,"a");
    fprintf(fp, "%d-%d-%d , %d:%d:%d , %d , %d \n", tm.tm_mday, ^
        tm.tm_mon+1, tm.tm_year+1900, tm.tm_hour, tm.tm_min, ^
        tm.tm_sec, counter, step);
    fclose(fp);
    printf("%d", counter);
    if (timer == max_count)
    {
        sleep(cooling);
    }
    timer = timer + 1;
    counter = 0;
}

```

Figure B.10: Function that prints the text file each second.

```c
//-------INSERT INPUT PARAMETERS-----------------------------//
//------------SET IN THE PYTHON INTERFACE)-------------------//
int main(int argc, char *argv[])
{
   max_count_char = argv[1];
   meas_char = argv[2];
   cooling_char = argv[3];
   max_count = atoi(argv[1]);
   meas = atoi(argv[2]);
   cooling = atoi(argv[3]);
   FILENAME = argv[4];
   printf("\n max_count = %d meas = %d \n", max_count, meas);

//----------------INITIALIZE PARAMETERS---------------------//
   counter = 0;
   timer = 0;
   seconds = 1;
   old_counts = 0;
   new_counts = 0;
   state_old = 0;
   i = 0;

//----------------INIZIALIZE GPIO LIBRARY------------------//
if (gpioInitialise() < 0)
{
}
else
{
   gpioSetMode(26, PI_INPUT);
}
FILE *fp;
fp = fopen(FILENAME,"a");
fclose(fp);

```

Figure B.11: First part of the main with the import of parameters from the python code, the initialization of variables and the GPiO setup.

```
//---------------COUNTING--------------//
while(i < meas)
{
   timer = 1;
   while(timer <= max_count)
   {
    state = gpioRead(26);
    if(state_old == 0)
    {
        if(state == 1)
        {
            counter = counter + 1;
            state_old = 1;
        }
        else
        {
            state_old = 0;
        }
    }
    else
    {
        if(state == 0)
        {
            state_old = 0;
        }
    }
    gpioSetTimerFunc(0,1000,timer_print_save);
   }
return 0;
}
```

Figure B.12: Second part of the main with the counting cycle.

Bibliography

[1] Ptcog site. https://www.ptcog.site/index.php/facilities-in-operation-public. Accessed: 11-07-2023.

[2] Sandro Rossi. Hadron therapy achievements and challenges: The cnao experience. *Physics*, 4(1):229–257, 2022.

[3] L Celona, G Ciavola, S Gammino, L Andò, and D Mascali. Design of the aisha ion source for hadrontherapy facilities. *Proceedings of ECRIS2012, Sydney, Australia Published in Experiments Read more... Monday*, 7:17, 2017.

[4] *Advances in Boron Neutron Capture Therapy*. Non-serial Publications. INTERNATIONAL ATOMIC ENERGY AGENCY, Vienna, 2023.

[5] Gazzetta ufficiale della repubblica italiana. Decreto legislativo 31 luglio 2020, n. 101. 2020.

[6] TT Böhlen, Francesco Cerutti, MPW Chin, Alberto Fassò, Alfredo Ferrari, P Garcia Ortega, Andrea Mairani, Paola R Sala, George Smirnov, and Vasilis Vlachoudis. The fluka code: developments and challenges for high energy and medical applications. *Nuclear data sheets*, 120:211–214, 2014.

[7] Alfredo Ferrari, Johannes Ranft, Paola R Sala, and A Fassò. *FLUKA: A multi-particle transport code (Program version 2005)*. Number CERN-2005-10. Cern, 2005.

[8] Stefano Dibartolomeo. Secondary radiation field characterization and neutron dosimetry measurements in a synchrotron for hadrontherapy, 2020.

[9] Matteo Frosini. Secondary radiation field characterization and neutron dosimetry measurements in a synchrotron for hadrontherapy, 2020. Available at https://hdl.handle.net/10589/153556.

[10] S Agosteo, A Mereghetti, E Sagia, and M Silari. Shielding data for hadron-therapy ion accelerators: Attenuation of secondary radiation in concrete. *Nuclear Instruments and Methods in Physics Research Section B: Beam Interactions with Materials and Atoms*, 319:154–167, 2014.

[11] S Agosteo, G Fehrenbacher, and M Silari. Attenuation curves in concrete of neutrons from 1 GeV/u C and U ions on a Fe target for the shielding design of RIB in-flight facilities. *Nuclear Instruments and Methods in Physics Research Section B: Beam Interactions with Materials and Atoms*, 226(3):231–242, 2004.

[12] S Agosteo, T Nakamura, M Silari, and Z Zajacova. Attenuation curves in concrete of neutrons from 100 to 400 MeV per nucleon He, C, Ne, Ar, Fe and Xe ions on various targets. *Nuclear Instruments and Methods in Physics Research Section B: Beam Interactions with Materials and Atoms*, 217(2):221–236, 2004.

[13] Yosuke Iwamoto and RM Ronningen. Attenuation of ambient dose equivalent from neutrons by thick concrete, cast iron and composite shields for high energy proton, 3He, 48Ca and 238U ions on Cu targets for shielding design. *Nuclear Instruments and Methods in Physics Research Section B: Beam Interactions with Materials and Atoms*, 269(3):353–363, 2011.

[14] Eunjoong Lee, Junhyeok Kim, Giyoon Kim, Jinhwan Kim, Kyeongjin Park, and Gyuseong Cho. Attenuation curves of neutrons from 400 to 550 Mev/u for Ca, Kr, Sn, and U ions in concrete on a graphite target for the design of shielding for the RAON in-flight fragment facility in Korea. *Nuclear Engineering and Technology*, 51(1):275–283, 2019.

[15] Francesco Bonforte. Monte carlo simulations for radiation protection purposes in two sychrotron facilities, 2020.

[16] Giuseppe Mazzola. Monte carlo approach for dose and activation analysis in an a-bnct facility: case study, 2021. Available at `https://hdl.handle.net/10589/176054`.

[17] Simona Lamorte. Characterization of an active rem counter based on a microstructured diode, 2020.

[18] Antonella Talamo. Study of the response of active dosimeters for a bnct radiation field, 2021.

[19] Giorgio Garlaschelli. Monte carlo simulations for radiation protection purposes in two sychrotron facilities, 2019. Available at `https://www.politesi.polimi.it/bitstream/10589/150827/1/Tesi%20Giorgio%20Garlaschelli.pdf`.

[20] Ncrp Party et al. Screening models for releases of radionuclides to atmosphere, surface water, and ground (ncrp report no. 123 i) and screening models for releases of radionuclides to atmosphere, surface water, and ground-work sheets (ncrp report no. 123 ii). *Physics in Medicine and Biology*, 42(1):263, 1997.

[21] S.G. Homann. HotSpot health physics codes version 2.07.2 user's guide. Technical report, National Atmospheric Release Advisory Center Lawrence Livermore National Laboratory, Livermore, US, 2011.

[22] Bruce A Napier. Genii version 2 users' guide. Technical report, Pacific Northwest National Lab.(PNNL), Richland, WA (United States), 2004.

[23] Tommaso Lorenzon. A computational method for assessing the dose due to chronic release of radioactive air : a hadron therapy facility case study, 2021. Available at `https://hdl.handle.net/10589/176260`.

[24] UDF Manual. Ansys fluent 12.0. *Theory Guide*, page 67, 2009.

[25] Giuseppe Giannattasio, Alessio Castorrini, Antonio D'Angola, Michele Ferrarini, and Francesco Bonforte. Three-dimensional computational fluid dynamics investigation of the dispersion of radioactive cloud-id rad11-318. 2023.

[26] I Strašík, E Mustafin, and M Pavlovič. Residual activity induced by heavy ions and beam-loss criteria for heavy-ion accelerators. *Physical Review Special Topics-Accelerators and Beams*, 13(7):071004, 2010.

[27] Alice Formento. Methodology for the study of induced activity in the systems, structures and components of the cnao synchrotron and the future hitachi synchrotron, 2021. Available at `https://hdl.handle.net/10589/174976`.

[28] Stefano Pizzardi. Activation study for future decommissioning of proton therapy and boron neutron capture therapy facilities at cnao with fluka simulations, 2022. Available at `https://hdl.handle.net/10589/196432`.

[29] Benedetta Brusasco. A method to study the water acti- vation with fluka and lsc for a hadron therapy facility, 2022. Available at `https://hdl.handle.net/10589/184347`.

[30] F Pozzi and M Silari. The cern-eu high-energy reference field (cerf) facility: New fluka reference values of spectral fluences, present and newly proposed operational quantities. *Nuclear Instruments and Methods in Physics Research Section A: Accelerators, Spectrometers, Detectors and Associated Equipment*, 979:164477, 2020.

[31] Kenneth S Krane. *Introductory nuclear physics*. John Wiley & Sons, 1991.

[32] Gary J Russell et al. Spallation physics-an overview. *Proc. ICANS-XI, Tsukuba*, pages 90–25, 1990.

[33] Alberto Rotondi, Paolo Pedroni, and Antonio Pievatolo. Monte carlo methods. In *Probability, Statistics and Simulation: With Application Programs Written in R*, pages 319–367. Springer, 2022.

[34] C Ahdida, D Bozzato, D Calzolari, F Cerutti, N Charitonidis, A Coronetti, GL D'Alessandro, A Donadon Servelle, LS Esposito, et al. New capabilities of the fluka multi-purpose code. *Frontiers in Physics*, page 705, 2022.

[35] Giuseppe Battistoni, Till Boehlen, Francesco Cerutti, Pik Wai Chin, Luigi Salvatore Esposito, Alberto Fassò, Alfredo Ferrari, Anton Lechner, Anton Empl, Andrea Mairani, et al. Overview of the fluka code. *Annals of Nuclear Energy*, 82:10–18, 2015.

[36] Jack PC Kleijnen, Ad Ridder, and Reuven Rubinstein. Variance reduction techniques in monte carlo methods. 2010.

[37] Fluka online manual. `http://www.fluka.org/content/manuals/online/INDEX-manual.html`. Accessed: 2023-19-03.

[38] Vasilis Vlachoudis et al. Flair: a powerful but user friendly graphical interface for fluka. In *Proc. Int. Conf. on Mathematics, Computational Methods & Reactor Physics (M&C 2009), Saratoga Springs, New York*, volume 176, 2009.

[39] Giuseppe Battistoni, Till Boehlen, Francesco Cerutti, Pik Wai Chin, Luigi Salvatore Esposito, Alberto Fassò, Alfredo Ferrari, Anton Lechner, Anton Empl, Andrea Mairani, et al. Overview of the fluka code. *Annals of Nuclear Energy*, 82:10–18, 2015.

[40] Dermott E Cullen, John H Hubbell, and Lynn Kissel. Epdl97: the evaluated photo data library97 version. Technical report, Lawrence Livermore National Lab.(LLNL), Livermore, CA (United States), 1997.

[41] A Ferrari, PR Sala, R Guaraldi, and F Padoani. An improved multiple scattering model for charged particle transport. *Nuclear Instruments and Methods in Physics Research Section B: Beam Interactions with Materials and Atoms*, 71(4):412–426, 1992.

[42] A Fasso, A Ferrari, J Ranft, and PR Sala. New developments in fluka modelling of hadronic and em interactions. In *KEK PROCEEDINGS*, volume 97, pages 32–43. NATIONAL LABORATORY FOR HIGH ENERGY PHYSICS, 1997.

[43] A Capella, U Sukhatme, C-I Tan, and J Tran Thanh Van. Dual parton model. *Physics Reports*, 236(4-5):225–329, 1994.

[44] B Deler and G Valladas. Practical formulation of the isobar model. *Il Nuovo Cimento A (1971-1996)*, 45(3):559–587, 1966.

[45] David J Herndon, Paul Söding, and Roger J Cashmore. Generalized isobar model formalism. *Physical Review D*, 11(11):3165, 1975.

[46] A Ferrari and PR Sala. A new model for hadronic interactions at intermediate energies for the fluka code. *MC93*, page 277, 1993.

[47] A Fasso, A Ferrari, J Ranft, and PR Sala. Fluka: performances and applications in the intermediate energy range. In *Proceedings of the Specialists Meeting on Shielding Aspects of Accelerators, Targets & Irradiation Facilities, Arlington, USA*, page 287, 1994.

[48] A Ferrari and P R Sala. The physics of high energy reactions. Technical report, CERN-ATL-PHYS-97-113, 1997.

[49] Stefan Roesler, Ralph Engel, and Johannes Ranft. The monte carlo event generator dpmjet-iii. In *Advanced Monte Carlo for Radiation Physics, Particle Transport Simulation and Applications: Proceedings of the Monte Carlo 2000 Conference, Lisbon, 23–26 October 2000*, pages 1033–1038. Springer, 2001.

[50] Victor Andersen, Francesca Ballarini, Giuseppe Battistoni, Mauro Campanella, Massimo Carboni, Francesco Cerutti, Anton Empl, Alberto Fasso, A Ferrari, E Gadioli, et al. The fluka code for space applications: recent developments. *Advances in Space Research*, 34(6):1302–1310, 2004.

[51] Heinz Sorge, Horst Stoecker, and Walter Greiner. Relativistic quantum molecular dynamics approach to nuclear collisions at ultrarelativistic energies. *Nuclear Physics A*, 498:567–576, 1989.

[52] Francesco Cerutti, G Battistoni, G Capezzali, P Colleoni, A Ferrari, E Gadioli, A Mairani, and A Pepe. Low energy nucleus–nucleus reactions: the bme approach and its interface with fluka. In *Proceedings of the 11th International Conference on Nuclear Reaction Mechanisms, Varenna (Italy)*, 2006.

[53] S Agosteo, M Magistris, A Mereghetti, M Silari, and Z Zajacova. Shielding data for 100–250 MeV proton accelerators: double differential neutron distributions and attenuation in concrete. *Nuclear Instruments and Methods in Physics Research Section B: Beam Interactions with Materials and Atoms*, 265(2):581–598, 2007.

[54] Francesco Bonforte, Michele Ferrarini, Antonio D'Angola, Elio Giroletti, and Daniele Introini. Heavy-ions shielding data for hadrontherapy application with monte carlo methods. *Radiation Protection Dosimetry*, page ncad207, 2023.

[55] James F Ziegler, Matthias D Ziegler, and Jochen P Biersack. SRIM–The stopping and range of ions in matter (2010). *Nuclear Instruments and Methods in Physics Research Section B: Beam Interactions with Materials and Atoms*, 268(11-12):1818–1823, 2010.

[56] Radiation Detection Technologies. Microstructured semiconductor neutron detector, 2021.

[57] Glenn F Knoll. *Radiation detection and measurement*. John Wiley & Sons, 2010.

[58] A Ferrari and M Pelliccioni. Fluence to dose equivalent conversion data and effective quality factors for high energy neutrons. *Radiation Protection Dosimetry*, 76(4):215–224, 1998.

[59] Richard H Olsher, Hsiao-Hua Hsu, Anthony Beverding, Jeffrey H Kleck, William H Casson, Dennis G Vasilik, and Robert T Devine. Wendi: an improved neutron rem meter. *Health Physics*, 79(2):170–181, 2000.

[60] S Agosteo, Marco Caresana, Michele Ferrarini, and M Silari. A dual-detector extended range rem-counter. *Radiation measurements*, 45(10):1217–1219, 2010.

[61] I Ö Andersson and Josef Braun. A neutron rem counter. Technical report, Aktiebolaget Atomenergi, Stockholm (Sweden), 1964.

[62] C Birattari, Adolfo Esposito, Alfredo Ferrari, M Pelliccioni, T Rancati, and M Silari. The extended range neutron rem counter linus: overview and latest developments. *Radiation Protection Dosimetry*, 76(3):135–148, 1998.

[63] Marco Caresana, C Cassell, Michele Ferrarini, E Hohmann, GP Manessi, S Mayer, M Silari, and Vincenzo Varoli. A new version of the lupin detector: Improvements and latest experimental verification. *Review of Scientific Instruments*, 85(6), 2014.

[64] M Pelliccioni. Overview of fluence-to-effective dose and fluence-to-ambient dose equivalent conversion coefficients for high energy radiation calculated using the fluka code. *Radiation Protection Dosimetry*, 88(4):279–297, 2000.

[65] Fabio Pozzi. *CERN Radiation Protection (RP) calibration facilities.* PhD thesis, Technische Universität München, 2016.

[66] Marco Silari and Fabio Pozzi. The cern-eu high-energy reference field (cerf) facility: applications and latest developments. In *EPJ Web of Conferences*, volume 153, page 03001. EDP Sciences, 2017.

[67] Radiological Protection. Icrp publication 103. *Ann ICRP*, 37(2.4):2, 2007.